Diss. ETH No. 18140

Photorefractive effects in $Sn_2P_2S_6$ at near bandgap and telecommunication wavelengths

A dissertation submitted to the
Swiss Federal Institute of Technology

ETH ZURICH

for the degree of
DOCTOR OF SCIENCES ETH ZÜRICH

presented by

Roger Mosimann

Dipl. Phys. ETH
born September 24, 1979
citizen of Sumiswald (BE), Switzerland

accepted on the recommendation of

Prof. Dr. P. Günter, examiner
Prof. Dr. G. Montemezzani, co-examiner
Dr. M. Jazbinsek, co-examiner

Zürich 2008

Contents

Abstract

Photorefractive crystals such as $LiNbO_3$, $KNbO_3$ or $BaTiO_3$ are very promising for many applications in all-optical signal processing. Unfortunately most photorefractive crystals suffer from serious constraints: One is their slow response time and the second is the very low sensitivity at near infrared wavelengths. Due to the need of fast nonlinear optical devices in optical communication systems, which mostly operate at the wavelength 1.55 μm, attention has been drawn to finding an appropriate photorefractive material. We investigated the photorefractive effects useful for such applications in tin hypothiodiphosphate ($Sn_2P_2S_6$), which is a rather new photorefractive material with very promising properties. It has a large coupling constant and very fast response times in the visible and near infrared region.

$Sn_2P_2S_6$ has a very large transparency range, from the visible green light at 530 nm into the infrared region at 8 μm. In this thesis, we will focus in the first part on the lower absorption edge region, where direct interband excitation is possible with widespread laser sources, allowing for very fast switching of light. We show that at a moderate light intensity of 0.5 W/cm^2 it is possible to diffract a probe beam of any wavelength above 560 nm with a response time of about 100 μs using green light for writing the photorefractive Bragg grating. In order to determine the necessary material parameters, a new method for measuring very high absorption constants through photocurrent measurements was developed and applied for several materials. Light induced waveguides could be formed in $Sn_2P_2S_6$ crystals by using the same green light source, with a recording time of 200 μs, the fastest ever measured, thus being good candidates for switches or similar applications. In extending this approach we were able to write arrays of such waveguides with a spacing of 7 μm, which can be controlled spatially by applying an external field.

In the second part we investigated the photorefractive properties of Te-doped $Sn_2P_2S_6$ crystals at the telecommunication wavelength 1.55 μm. Doping with tellurium atoms (Te) extends the photorefractive response of the material into the near infrared region. For the first time we could demonstrate photorefraction in a bulk ferroelectric crystal at 1.55 μm. A coupling constant of up to 6 cm^{-1} with a response time of 10 ms was observed without using any resonant methods or external fields to enhance the photorefractive response. This is the main advantage of Te-doped $Sn_2P_2S_6$, since the only other materials having comparable photorefractive effects at this wavelength are semiconductors, where a large external applied field is necessary to obtain these results. In a next step planar

waveguides were created in $Sn_2P_2S_6$ crystals by He^+-ion implantation and photorefractive two-wave mixing demonstrated therein. Waveguides offer several advantages, firstly they confine the beam strongly, which results in a faster response and in case of $Sn_2P_2S_6$ helps to overcome the high dark conductivity at 1.55 μm. Secondly they are compatible to integrated optics and fiber technology and thirdly the implantation process can increase the photorefractive response of the material. We show that for pure $Sn_2P_2S_6$ crystals the photorefractive response has been increased by ion-implantation by almost a factor of two whereas in Te-doped crystals the properties are the same as for the bulk material, preserving the very good photorefractive properties of Te:$Sn_2P_2S_6$ at 1.55 μm.

Zusammenfassung

Photorefraktive Kristalle wie zum Beispiel $LiNbO_3$, $KNbO_3$ oder $BaTiO_3$ sind sehr vielversprechend für viele Anwendungen auf dem Gebiet der rein optischen Signalverarbeitung. Leider weisen die meisten photorefraktiven Kristalle erhebliche Nachteile auf: Zum einen die langsame Antwortzeit und zum anderen die tiefe Empfindlichkeit im nahen infraroten Wellenlängenbereich. Durch die Nachfrage nach schnellen nichtlinear optischen Kommunikationsmittel in optischen Systemen, welche fast immer bei der Wellenlänge 1.55 μm arbeiten, wurde die Suche nach einem passenden photorefraktiven Material verstärkt. Wir haben die photorefraktiven Effekte, welche für solche Anwendungen nützlich sind, in Zinn-Hypothiodiphosphat ($Sn_2P_2S_6$) untersucht. $Sn_2P_2S_6$ ist ein eher neues photorefraktives Material mit sehr vielversprechenden Eigenschaften. Es hat eine sehr hohe Verstärkungskonstante und eine sehr schnelle Antwortzeit im sichtbaren und nahen infraroten Wellenlängenbereich.

$Sn_2P_2S_6$ ist über einen grossen Wellenlängenbereich transparent, beginnend im sichtbaren grünen Licht bei 530 nm bis tief in die infrarote Lichtregion bei 8 μm hinein. In dieser Doktorarbeit konzentrieren wir uns im ersten Teil auf die Region der unteren Absorptionskante, wo direkte interband Anregung mit weit verbreiteten Lasern möglich ist und damit das sehr schnelle schalten von Licht erlaubt. Wir zeigen, dass es möglich ist mit der moderaten Lichtintensität von 0.5 W/cm^2 einen Laserstrahl von beliebiger Wellenlänge grösser als 560 nm, mit einer Antwortzeit von ungefähr 100 μs zu beugen, wobei sichtbares grünes Laserlicht zum schreiben des photorefraktiven Bragg Gitters verwendet wurde. Um die notwendigen Materialparamter zu bestimmen, wurde eine neue Methode entwickelt und für mehrere Materialien angewendet, die die Messung von sehr hohen Absorptionskonstanten durch Photostrommessungen ermöglicht. Mit der selben grünen Laserquelle konnten auch licht-induzierte Wellenleiter mit einer Antwortzeit von ca. 200 μs in $Sn_2P_2S_6$ Kristallen realisiert werden. Dies stellt die schnellste je gemessene Antwortzeit dar und macht das Material deshalb zu einem sehr guten Kandidaten für das Schalten von Licht oder ähnlichen Anwendungen. Durch Erweitern dieses Ansatzes konnten wir ein Array solcher Wellenleiter mit einem Abstand von jeweils 7 μm schreiben und mit Hilfe eines externen Feldes die örtliche Position kontrollieren und verändern.

Im zweiten Teil der Doktorarbeit wurden die photorefraktiven Eigenschaften von Te-dotierten $Sn_2P_2S_6$ Kristallen bei der Telekommunikationswellenlänge 1.55 μm untersucht. Durch das dotieren mit Tellurium Atomen (Te) wird die photorefraktive Sensibilität des

Materials in den nahen Infrarotbereich hin erweitert. Zum ersten Mal überhaupt ist es gelungen Photorefraktion in einem massiven ferroelektrischen Kristall bei 1.55 μm zu zeigen. Eine Verstärkungskonstante von bis zu 6 cm^{-1} mit einer Antwortzeit von 10 ms konnte gemessen werden. Dies ohne weitere Möglichkeiten zum Verstärken des Effekts zu nutzen, wie zum Beispiel ein elektrisches Feld anzulegen oder bei einer Resonanz zusätzlich zu pumpen. Dies ist der Hauptvorteil von Te-dotierten Sn$_2$P$_2$S$_6$ Kristallen, da nur Halbleiter vergleichbare photorefraktive Eigenschaften bei dieser Wellenlänge aufweisen und bei diesen ein hohes angelegtes elektrisches Feld von Nöten ist. In einem nächsten Schritt wurden planare Wellenleiter in Sn$_2$P$_2$S$_6$ Kristallen mittels He$^+$-Implantation hergestellt und Zwei-Wellen Mischen darin demonstriert. Wellenleiter bieten mehrere Vorteile. Als erstes wird der Strahl sehr stark eingeengt, was eine schnellere Antwortzeit zur Folge hat und durch die höhere Intensität geeignet ist die hohe Dunkelleitfähigkeit in Sn$_2$P$_2$S$_6$, speziell bei $\lambda = 1.55$ μm, zu übertreffen. Zweitens sind die Wellenleiter kompatibel mit Fibern oder anderen integrierten optischen Bauteilen und drittens besteht die Möglichkeit, dass das Implantieren die photorefraktiven Eigenschaften des Materials verbessert. Wir zeigen das für reines Sn$_2$P$_2$S$_6$ durch die Implantation die Zwei-Wellen Mischen Verstärkungskonstante des Materials fast verdoppelt wurde, wohingegen in Te-dotierten Kristallen die Eigenschaften die selben wie im massiven Kristall sind, was bedeutet, dass auch die sehr guten Eigenschaften bei 1.55 μm im Wellenleiter erhalten bleiben.

Chapter 1

Introduction

Photonics is the science of the harnessing of light, and encompasses its generation, its detection, and manipulation. As one of the driving technologies of modern telecommunication, photonics is a key technology in the 21st century. Being able to transmit a large amount of data through optical fibers over a long distance at the speed of light is the basis of the networked economy. This means that there is a great interest in developing new technologies and materials in areas like laser manufacturing, fiber-optics, integrated-optics, nonlinear-optics or electro-optics. Other fields for applications of photonics apart from telecommunication include biological and chemical sensing, medical diagnostics and therapy, security scanning technology, display technology, optical computing, and many more.

This thesis studies tin hypothiodiphosphate ($Sn_2P_2S_6$) as a possible material for applications in telecommunication. The material has shown very promising photorefractive properties and is a good candidate for photorefractive applications at the important telecommunication wavelength 1.55 μm. So far no material has been found with satisfying properties at this wavelength. In chapter 2 the interband photorefraction in $Sn_2P_2S_6$ is investigated for possible switching applications and in chapter 3 this effect is used to guide light dynamically in one respectively an array of light induced waveguides. Chapter 4 describes the photorefractive properties of Te-doped $Sn_2P_2S_6$ at the wavelength 1.55 μm. This is the first time photorefractive sensitivity could be demonstrated in a bulk ferroelectric crystal at this wavelength. Ion implantation was used to create a planar waveguide in the bulk crystal and the properties in this waveguiding region are described in chapter 5. In the following chapter basic concepts and models which are important for this work are introduced.

1.1 Nonlinear optics

1.1.1 Linear and nonlinear optical effects

In the electromagnetic theory of light, the material response to the illumination of light is described by the following equation:

$$
\begin{aligned}
P_i &= P_i^0 + P_i^L + P_i^{NL} \\
&= P_i^0 + \underbrace{\varepsilon_0 \, \chi_{ij}^{(1)} \, E_j}_{P_i^L} + \underbrace{\varepsilon_0 \, \chi_{ijk}^{(2)} \, E_j E_k + \varepsilon_0 \, \chi_{ijkl}^{(3)} \, E_j E_k E_l + \ldots}_{P_i^{NL}}
\end{aligned}
\tag{1.1}
$$

using the Einstein convention for summation over common indices (with $i, j, k, l = 1, 2, 3$); $\boldsymbol{P}$ is the macroscopic material polarization, $\boldsymbol{P}^0$ the spontaneous polarization, $\boldsymbol{P}^L$ the linear polarization, $\boldsymbol{P}^{NL}$ the nonlinear polarization, $\boldsymbol{E}$ the electric field of the light, ε_0 the vacuum permittivity, $\chi^{(1)}$ the linear, $\chi^{(2)}$ the second-order, and $\chi^{(3)}$ the third-order susceptibility. In the dipole approximation the even-order susceptibilities are only present in noncentrosymmetric materials because of symmetry reasons. The odd-order susceptibilities on the other hand occur in all materials. All the information on the macroscopic optical properties of a material is represented in the susceptibility tensors $\chi^{(n)}$.

For lower light intensities, such as natural sun light, only the first order, linear, term of Eq. 1.1 is needed to describe the optics, because the higher order terms are very small. Thus in order to induce a nonlinear optical effect in a material a high intensity is needed, which is generally the case for the light emitted by lasers, illustrating the close relationship these two fields of research historically share. The second-order term $\chi^{(2)}$ is then responsible for effects such as second harmonic generation or parametric amplification and oscillation, whereas the third-order term $\chi^{(3)}$ causes phenomena like third harmonic generation, self-focusing and optical phase conjugation.

1.1.2 Electro-optic effect

If the electric field $\boldsymbol{E}$ is composed by the field $\boldsymbol{E}^\omega$ of an optical wave plus a static electric field $\boldsymbol{E}^0$, the nonlinear polarization P_i^{NL} in (1.1) will have terms of the same frequency as $\boldsymbol{E}^\omega$, the first such terms being

$$
P_i^{NL} = 2 \, \varepsilon_0 \, \chi_{ijk}^{(2)} \, E_j^\omega E_k^0 + 3 \, \varepsilon_0 \, \chi_{ijkl}^{(3)} \, E_j^\omega E_k^0 E_l^0 + \ldots
\tag{1.2}
$$

This polarization gives a change of the refractive index, which is best written as the change of the tensor $\varepsilon^{-1} = n^{-2}$ in the form

$$
\Delta \left(\frac{1}{n^2} \right)_{ij} = r_{ijk} E_k^0 + R_{ijkl} E_k^0 E_l^0 + \ldots
\tag{1.3}
$$

where r_{ijk} is the linear electro-optic tensor, related to $\chi^{(2)}_{ijk}$, and R_{ijkl} is the quadratic electro-optic tensor, which is related to $\chi^{(3)}_{ijkl}$. Contrarily to the nonlinear optical effect, the electro-optic effect does not depend on the intensity of the optical wave $\boldsymbol{E}^{\omega}$, but only on the static field $\boldsymbol{E}^0$. Note that due to dispersion, the linear and nonlinear optical susceptibilities depend on the frequency of the fields involved.

For the linear electro-optic effect (Pockels effect) we can approximate the refractive index changes Δn_i induced by the field in first order as:

$$\Delta n_i = -\frac{n_i^3 r_{ijk} E_k}{2} \tag{1.4}$$

In most photorefractive crystals it is sufficient to consider the above linear electro-optic effect only. As we will discuss in the following section, in such crystals the linear electro-optic effect may lead to a spatial modulation of the refractive index, in which the refractive index change depends linearly on the electric field. This effect is the basis for the experiments reported in Chapters 2 to 5.

1.2 Photorefractive effect

The photorefractive effect is a phenomenon in which the local index of refraction of a medium is changed by the illumination of a beam of light with a spatial intensity variation. Such an effect was first discovered in 1966 when researchers were studying the transmission of laser beams through electro-optic crystals. It was found that the presence of laser beams inside some electro-optic crystals leads to an index inhomogeneity, which distorts the wave front of the transmitted laser beam. Such an effect was first referred to as "optical damage" [1] and is now knows as the photorefractive effect. Many different effects can lead to photorefraction as for example photochemical effects, photoinduced reorientation of molecules, Kerr effect at high intensity, or photoinduced thermal effects. In this chapter we will restrict the definition of the photorefractive effect to the refractive index change due to light induced charge transport in electro-optic materials. Even though in some cases thermally induced charge carriers can significantly influence the resulting photorefractive effect, as one can see in chapter 4 and 5. Photorefraction gives rise to many interesting effects as for example light induced wave-guiding [2], phase conjugation [3,4], beam amplification [5], and four wave mixing [6].

In this section the basic theory of photorefraction, starting from the band-transport model will be presented. The special case of direct band-to-band photo-excitation will be considered in section 1.3.

Physical Processes Involved in the Photorefractive Effect

The photorefractive effect can be described by the following four processes:

- Generation of charge carriers through photo-excitation by an inhomogeneous illumination. Charge carriers can either be electrons excited from trap levels in the material energy band gap into the conduction band, or holes excited into the valence band.

- Transport of the excited, mobile charges from the illuminated regions into dark zones due to diffusion or to electric forces, induced by an external field or the internal space charge field (drift). In some materials a preferred initial momentum is present, adding to the charge separation (photogalvanic effect).

- In the dark areas the mobile charge carriers recombine into trapped states such as defects, impurities or self-trapping. This charge separation continues until the diffusion current is counterbalanced by the drift current.

- Due to this charge redistribution, a space charge electric field is generated, which leads to a change of the refractive index via the electro-optic effect, described shortly in section 1.1.2.

Fig. 1.1 illustrates the involved processes and steps for the special case of hole diffusion. In Fig. 1.2 a simplified band-scheme and the most important processes for photo-excitation, displacement, recombination, and trapping of charge carriers are depicted.

In the following, we introduce the most important mathematical models used to describe the above mentioned physical processes.

The so-called conventional model was elaborated by Kukhtarev et al. [7–9] considering only photo-excitation and recombination of one species of charge carriers between a single donor level and the corresponding conduction band. This single-level band scheme, along with the involved physical mechanisms, is depicted in Fig. 1.3. Note that while this simplified model describes satisfactorily the processes in a large number of materials showing the photorefractive effect, there exist several crystals where details of the charge transport mechanism are better described by considering additional defect levels [10–12]. Another important limitation is that the photon energies of the light illumination must be smaller than the band-gap energy.

The involved processes can be described by the following set of equations

$$\frac{\partial N_D^+}{\partial t} = (s_e I + \beta_e)(N_D - N_D^+) - \gamma_e n N_D^+ \tag{1.5}$$

$$\frac{\partial n}{\partial t} = \frac{\partial N_D^+}{\partial t} + \frac{1}{e}\boldsymbol{\nabla}\mathbf{J}_e \tag{1.6}$$

$$\mathbf{J}_e = en\boldsymbol{\mu}_e\mathbf{E} + k_\mathrm{B}T\boldsymbol{\mu}_e\boldsymbol{\nabla}n + es_e I(N_D - N_D^+)\mathbf{L}_{ph} \tag{1.7}$$

$$\boldsymbol{\nabla}\mathbf{E}_\mathrm{sc} = \frac{e}{\varepsilon_0\varepsilon_\mathrm{eff}}(N_D^+ - n - N_A), \tag{1.8}$$

where the photoexcited charges are assumed to be electrons. The symbols in the above equations are:
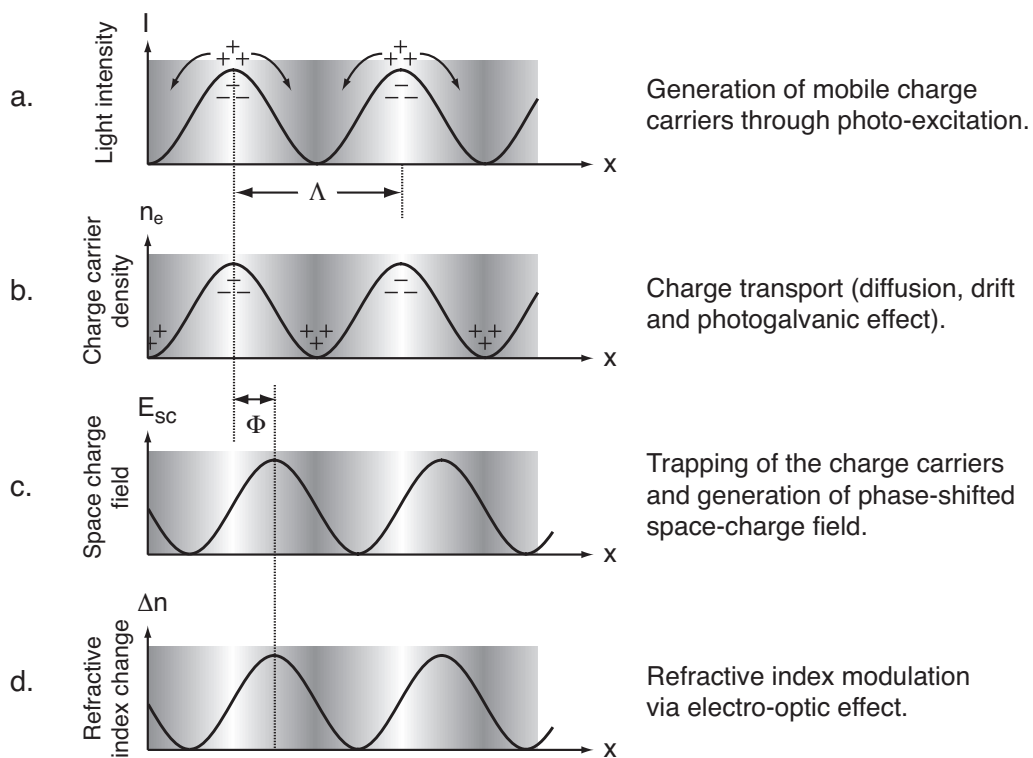
FIGURE 1.1: Mechanisms involved in photorefraction, here illustrated for the case of hole transport. Λ is the grating constant and Φ is the phase shift between light intensity and refractive index modulation. For charge transport dominated by diffusion one gets $\Phi = \Lambda/4$.
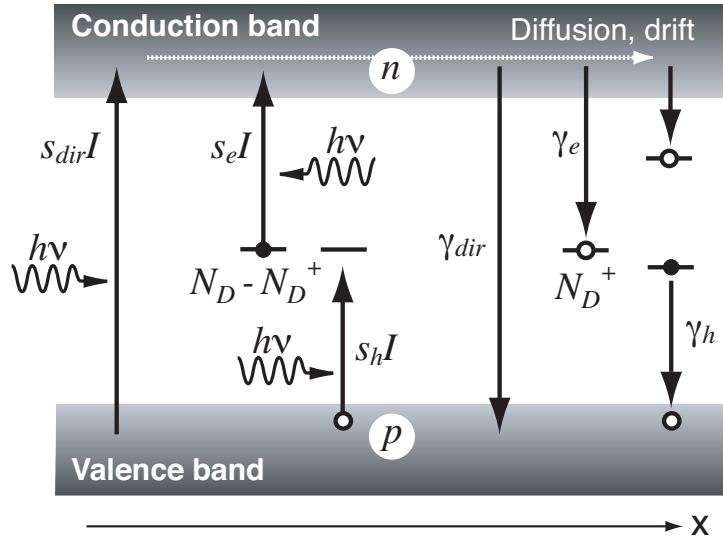
FIGURE 1.2: Simplified band scheme of possible charge transitions in a photorefractive material with the concentration of ionized donors $N_D - N_D^+$ and traps N_D^+. Excitation of charge carriers may occur via band-to-band (with a generation rate $s_{dir}I$), trap-to-band ($s_e I$), and band-to-trap transitions ($s_h I$). Excited charges are displaced by diffusion and drift. They can recombine through band-to-band electron-hole recombination (with a recombination rate γ_{dir}), or be trapped in mid-bandgap levels (γ_e and γ_h). The arrows show the movements of the electrons and thermal excitation is not depicted.
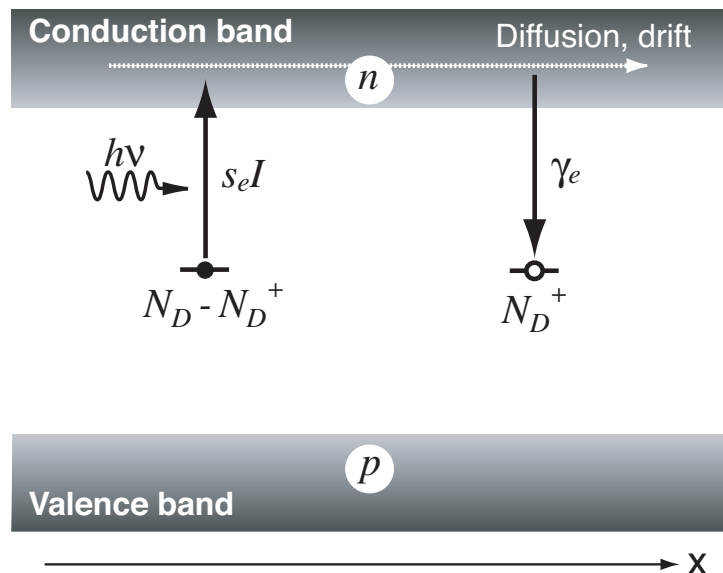
FIGURE 1.3: Single level band scheme in the conventional model at low intensities. An electron is photoexcited to the conduction band from a mid band-gap level. Diffusion or drift result in a displacement of the electron. Near a trap center, the electron can be retrapped.

- n the free electron concentration in the conduction band;
- N_D the donor concentration;
- N_D^+ the concentration of ionized donors;
- N_A the concentration of ionized donors (acceptors) in the dark;
- $\mathbf{J}_e$ the electron current density;
- $\mathbf{E}$ the total electric field;
- $\mathbf{E}_{sc}$ the space charge field;
- I the light intensity;
- $\mathbf{L}_{ph}$ the photogalvanic transport length vector;
- s_e the photoionization constant for electrons;
- β_e the thermal (dark) generation rate for electrons;
- γ_e the recombination constant for electrons;
- $\boldsymbol{\mu}_e$ the electrons mobility;
- ε_0 the vacuum dielectric permittivity;
- $\varepsilon_{\mathrm{eff}}$ the dielectric permittivity of the material in the direction of $\mathbf{E}_{sc}$;
- e the absolute value of the elementary charge;
- k_{B} the Boltzmann constant;
- T the absolute temperature.

Equation (1.5) is the rate equation for the concentration of the ionized donors. The first term describes the photoionization process ($s_e I$) and the thermal excitation of electrons from the donor level. The second term takes into account the recombination of the electrons (γ_e) into traps, in our case ionized donors. The second equation (1.6) is the continuity equation for the electron density. The additional term with respect to Eq. (1.5) describes the divergence of the electron current density. Eq. (1.7) describes the different contributions to the electron current density. The first term gives the drift current in the total electric field $\mathbf{E} = \mathbf{E}_{sc} + \mathbf{E}_0$, where $\mathbf{E}_0$ is the applied field. The second term describes the diffusion process of the electrons generated by the electron concentration gradient. Thus, this term only gives a contribution for inhomogenous illumination. The last term gives the photogalvanic current, if present. In $\mathrm{Sn_2P_2S_6}$ it is negligible, therefore we do not consider it in the following. The last equation (1.8) is the Poisson equation for the electric field. It describes the spatially modulated part of the electric field generated by the nonuniform distribution of the charge carriers in the crystal. These four equations are valid in this form only for isotropic photoexcitation, i.e., if s_e is independent on the light polarization and intensity, or if the intensity and polarization of the exciting light

wave is invariant, i.e., constant, with respect to its propagation direction, like in the case of a plane wave.

1.2.1 Photorefractive gratings

Irradiating a photorefractive material homogeneously will not generate a space charge field or refractive index grating, but only change some of the bulk material properties like the conductivity or the absorption. In contrast, for an inhomogeneous illumination the charges are locally redistributed and will result in a space charge field. An effective way to produce an intensity pattern is given by the interference of two plane waves. Considering two plane waves with wavevectors $\mathbf{k}_1$ and $\mathbf{k}_2$ and electric field amplitudes A_1 and A_2 respectively we obtain a sinusoidal intensity pattern of the form

$$I(\mathbf{x}) = I_0(1 + m \cos \mathbf{K} \cdot \mathbf{x}) \tag{1.9}$$

where $\mathbf{K} = \mathbf{k}_1 - \mathbf{k}_2$ is the grating vector, $\mathbf{x}$ is the position vector, $m = 2\frac{|A_1||A_2|}{|A_1|^2+|A_2|^2}$ is the modulation depth, and $I_0 = \frac{1}{2}\sqrt{\epsilon_0/\mu_0}(|A_1|^2 + |A_2|^2)$ the mean intensity. For small modulation m, such an intensity distribution will build-up a spatial periodic space charge field $\mathbf{E}_{\mathrm{sc}}$ with the same period. The direction of $\mathbf{E}_{\mathrm{sc}}$ is oriented parallel to the grating vector $\mathbf{K}$ and we will denote in the following the amplitude of the first spatial Fourier component of the space charge field with E_{sc}. In order to include in E_{sc} also the phase of the $\mathbf{E}_{\mathrm{sc}}$ grating with respect to the illumination grating (1.9), we allow complex values of E_{sc} by defining $\mathbf{E}_{\mathrm{sc}} = \mathrm{Re}(E_{\mathrm{sc}} \exp i \mathbf{K} \cdot \mathbf{x}) \mathbf{K}/|\mathbf{K}|$. In this way a purely imaginary value of E_{sc} means that the space charge grating is shifted by $\pi/2$ with respect to the illumination grating. The exact amplitude of E_{sc} for the conventional model will be given later in this section and for interband photorefraction in the next section.

In an electro-optic material the presence of a periodic space charge field E_{sc} generates a refractive index grating, which can be investigated by diffraction experiments of a third plane wave, eventually at a different wavelength. For non-centrosymmetric materials that exhibit the linear electro-optic effect, the change of the dielectric permittivity tensor is defined as

$$\Delta \boldsymbol{\epsilon}^{-1} = \mathbf{r}_{\mathrm{eff}}(\mathbf{K}) E_{\mathrm{sc}}. \tag{1.10}$$

where $\boldsymbol{\epsilon}$ is the dielectric permittivity tensor in the material at the corresponding light wavelength and $\mathbf{r}_{\mathrm{eff}}(\mathbf{K})$ is a 3×3 matrix describing the electro-optic effect, which involves the unclamped electro-optic tensor and the additional contributions from the piezo-electric effect [13]. Since in (1.10), and alike in the following formula for Δn, the oscillating spatial term is not included, the left-hand side of these equations are the complex first spatial Fourier components.

For a certain geometry and light polarization, the amplitude of the spatially periodic refractive index change Δn can be expressed as

$$\Delta n \approx -\frac{1}{2} n^3 r_{\mathrm{eff}} E_{\mathrm{sc}} \tag{1.11}$$

where n is the refractive index seen by the beam, and r_{eff} is the effective electro-optical coefficient relevant for this geometry. In the following section the magnitude of the space charge field is considered in detail.

Space charge field for sinusoidal illumination

A solution of Eqs. (1.5)–(1.8) can be found in the case where the material is illuminated with an intensity distribution as described by Eq. (1.9).

The space charge field is parallel to the grating vector and its amplitude is $|E_{\text{sc}}|$. Without any external electric field applied to the crystal and negligible photogalvanic current, the complex amplitude of the space charge field E_{sc} in case of small modulation depth m is given by [8]

$$E_{\text{sc}} = i\,m\,\frac{E_q E_D}{E_q + E_D} \tag{1.12}$$

where i is the imaginary unit and indicates that the space-charge field grating is shifted by $\pi/2$ compared to the illumination grating. For a better physical interpretation of E_{sc} we have introduced the diffusion field E_D and the trap limited field E_q. The first is defined as

$$E_D = \frac{k_B T}{e} K, \tag{1.13}$$

and corresponds to the field amplitude of a sinusoidal electric field that exactly counteracts the effect of the charge diffusion process. The trap limited field is

$$E_q = \frac{e}{\epsilon_{\text{eff}} \epsilon_0 K} N_{\text{eff}} \tag{1.14}$$

and gives a limit for the maximum E_{sc} that can be generated with the available traps. In Eq. (1.14) ϵ_{eff} is the effective dielectric constant for the chosen configuration [14], and N_{eff} is the effective trap density defined as

$$N_{\text{eff}} = \frac{N_{D0}^+(N_D - N_{D0}^+)}{N_D} \tag{1.15}$$

where $N_{D0}^+ = n_0 + N_A$ is the spatial average of ionized donors with illumination switched on. Although n_0, the spatial average of electrons in the conduction band when the light is on, is dependent on the intensity I_0 of the light, n_0 is in most cases much smaller than N_A, so that $N_{D0}^+ \approx N_A$, N_{eff} and E_q are independent on the light intensity in the conventional model.

An important conclusion can be deduced from Eq. (1.12). If one of the two fields E_q or E_D is much smaller than the other, the total space-charge field is limited by this field. These limiting cases can be observed experimentally by varying the grating constant K.
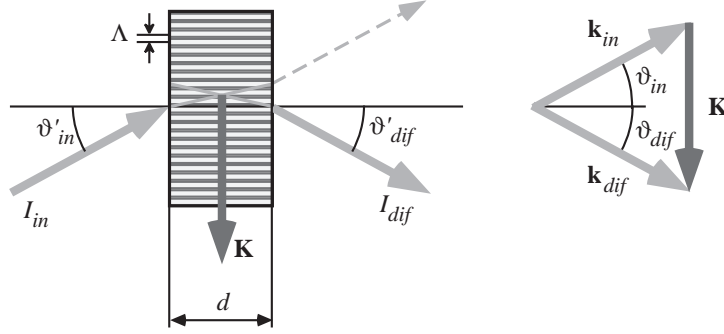
FIGURE 1.4: Schematic representation of light diffraction at an unslanted holographic grating with grating period Λ. On the right-hand side the wave-vector momentum conservation for the incident and diffracted beam is depicted. To fulfill the Bragg condition, the difference between the wave-vectors must correspond to the grating vector $K = 2\pi/\Lambda$.

Space charge field for an externally applied field

In the case when there is an external applied electric field E_0, the amplitude of the space-charge field E_{sc} is given by the following expression:

$$E_{sc} = im \frac{E_q E_D}{E_q + E_D} \left(\frac{1 + i\frac{E_0}{E_d}}{1 + i\frac{E_0}{E_d + E_q}} \right) \tag{1.16}$$

The first term on the right hand side of the equation is the space-charge field in the absence of an applied field, identical with Eq. 1.12. The term inside the brackets represents a scaling factor due to the presence of a DC electric field E_0. This scaling factor is a complex number. Thus the applied electric field not only changes the magnitude of the space-charge field, but also alters its spatial phase.

By examining the scaling factor in Eq. 1.16, we note that the effect due to the applied field E_0 is insignificant when $E_q \ll E_d$ which occurs, according to Eqs. 1.13 and 1.14, at large wave numbers (or smaller grating periods). Generally speaking, the externally applied field E_0 has a large effect on the space-charge field when $E_q \gg E_d$ and $E_0 \geq E_d$. With these conditions fulfilled an externally applied field can be used to significantly increase the photorefractive response of some materials [15].

Beam diffraction at an holographic grating

Diffraction gratings are one of the most powerful elements in modern optics. For a diffraction grating two regimes, Bragg and Raman-Nath, can be distinguished [16]. We will focus on Bragg diffraction that is typical for thick (volume) holographic gratings, as mostly the case in photorefractive experiments.

The diffraction efficiency of a grating is defined as $\eta = I_{dif}/I_{in}$, where I_{dif} and I_{in} are the intensities of the diffracted beam and input beam respectively. For a Bragg grating, η was first calculated by Kogelnik [17] using the theory of coupled waves and recently

expanded to the case of anisotropic materials by Montemezzani and Zgonik [18]. If we have the same absorption α for the incoming and the diffracted wave and a grating of thickness d with refractive index modulation only, one obtains the following equation:

$$\eta = \frac{\sin^2 \sqrt{\nu^2 + \xi^2}}{1 + \xi^2/\nu^2} \, e^{-\alpha d} \tag{1.17}$$

with

$$\xi^2 = \frac{\Delta k^2}{4} d^2 \tag{1.18}$$

$$\nu^2 = \frac{k_0^2 A_r^2}{16 n_i n_{dif} g_{in} g_{dif} \cos \vartheta_{in} \cos \vartheta_{dif}} d^2 \tag{1.19}$$

where Δk represents the wave-vector mismatch from the Bragg condition projected normal to the sample surface, $g_{in,dif} = \hat{\mathbf{e}}_{in,dif} \hat{\mathbf{d}}_{in,dif}$ are the projection cosines between electric-field ($\hat{\mathbf{e}}_{in,dif}$) and dielectric-displacement ($\hat{\mathbf{d}}_{in,dif}$) unit vectors of the incident and diffracted beam respectively, and $\vartheta_{in,dif}$ are the angles inside the material between the Poynting vectors of the incident and the diffracted wave and the normal of the entrance surface (see Fig. 1.4, where $g_{in} = g_{dif} = 1$ was assumed). The coupling constant A_r can be expressed in case of refractive index modulation caused by the electro-optic effect and a space-charge field E_{sc} as

$$A_r = -n_{in}^2 n_{dif}^2 g_{in} g_{dif} r_{eff} E_{sc} . \tag{1.20}$$

Neglecting the anisotropy of the crystal and using (1.11) leads to the approximation

$$\nu^2 = \frac{k_0^2 (\Delta n \, d)^2}{4 \cos \vartheta_{in} \cos \vartheta_{dif}} \tag{1.21}$$

often used to determine Δn from diffraction experiments.

The dependence of the diffraction efficiency on the beam incidence angle in the air ϑ'_{in}[1] is shown for a 1 cm thick $Sn_2P_2S_6$ crystal in Fig. 1.5. The diffraction efficiency presents a strong central peak. On the top of the peak, at Bragg matching ($\Delta k = \xi = 0$), Eq. (1.17) for the diffraction efficiency reduces to $\eta = e^{-\alpha d} \sin^2 \nu$. On the other side, for weak gratings ($\nu^2 \ll 1$) and negligible absorption the curve of Fig. 1.5 is proportional to $\nu^2 (\sin \xi/\xi)^2$. In this case η results simply proportional to ν^2 and therefore proportional to the square of the spatial field modulation, $|E_{sc}|^2$. The position of the side minima and the zero crossing is determined by ξ, i.e. by wave-vector mismatch Δk and the thickness of the crystal. Another important property of Eq. (1.17) is that for a large value of $\nu \approx 1$ diffraction efficiency as high as 100 % can be expected if the absorption is negligible. This allows a very effective way to deviate light beams.

---

[1]The relation between the angle inside the material and in the air is given by Snell's law $n_{in} \sin \vartheta_{in} = \sin \vartheta'_{in}$
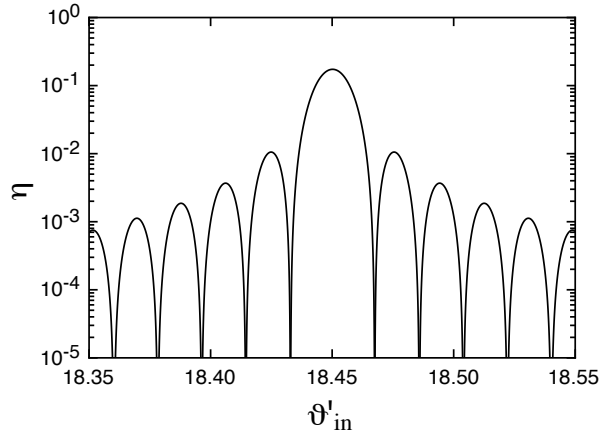
FIGURE 1.5: Diffraction efficiency η as function of the external angle ϑ'_{in} for a 1 cm thick Sn$_2$P$_2$S$_6$ crystal. The other parameters are the grating spacing $\Lambda = 1\,\mu$m, $\lambda = 633\,$nm, $\Delta n = 5 \cdot 10^{-5}$, and the absorption $\alpha = 0.5\,$cm^{-1}.

Dynamics of grating formation

To form the grating needed for a significant diffraction efficiency, a large number of charge carriers have to be excited. In order to do so photons have to be absorbed and thus the speed of the photorefractive effect is in a first approach fundamentally limited by the photon flux. This simple approach can be used to derive a fundamental limit for the speed of the photorefractive effect [19]. We assume, that the charge density is a sinusoidal function:

$$\rho = \rho_0 \ \cos(Kx) \tag{1.22}$$

where ρ_0 is a constant. The number of photoexcitations needed to create this distribution in N_p and the time τ_{fund} required to generate these N_p photoexcitations in a unit volume is then described by the following formula:

$$\tau_{fund} = \frac{h\nu}{e} \frac{\lambda}{\Lambda} \frac{\Gamma}{\alpha_p} \frac{2}{\pi\eta} \frac{1}{IQ}, \tag{1.23}$$

where $h\nu$ is the photon energy at wavelength λ, e is the fundamental electron charge, Λ is the grating spacing, Γ is the two-wave mixing gain, see section 1.2.1, α_p the absorption, η the quantum efficiency, I the light intensity and $Q = \frac{n^3 r}{\varepsilon_0 \varepsilon}$ the figure of merit for photorefractive materials. If we assume a quantum efficiency of 1 and the following parameters: $h\nu = 2$ eV, $\lambda/\Lambda = 0.1$, $\alpha_p = 1$ cm^{-1}, $I = 1$ W/cm^2, $n = 3$, $r = 180$ pm/V, $\varepsilon = 230$, which are similar to the ones of Sn$_2$P$_2$S$_6$, we get for a gain constant of 5 cm^{-1} a limit of 30 μs, which can be compared to the measured build-up times, that are in the order of several ms.

However, to see how the space-charge field builds up with time before reaching the steady state, we need to consider not only the rate of photoexcitation but also other

processes, such as the rate of recombination and the speed of charge transport. All these mechanisms are included in the band transport model described by Eqs. 1.5-1.8. Solving these equations for the time dependent variables $N_D^+(t)$, $n(t)$, $\mathbf{J_e}(t)$ and $\mathbf{E_{sc}}(t)$ will result in a exponential build-up of the space-charge field (and thus the coupling constant Γ):

$$E_{sc}(t) = E_{sc}\left(1 - \mathrm{e}^{-t/\tau}\right),\tag{1.24}$$

where E_{sc} is the same as for the steady state solution in Eq. 1.16 and τ is the complex time constant

$$\tau = \tau_{die}\frac{1 + \frac{E_d + iE_0}{E_m}}{1 + \frac{E_d + iE_0}{E_q}}\tag{1.25}$$

with the dielectric relaxation time for negligible dark conductivity

$$\tau_{die} = \frac{\varepsilon_0\varepsilon}{\sigma_{photo}} = \frac{\varepsilon_0\varepsilon}{e\mu n_0},\tag{1.26}$$

where

$$n_0 = \frac{sI_0(N_D - N_{D0}^+)}{\gamma N_{D0}^+}\tag{1.27}$$

and the drift field

$$E_m = \frac{\gamma N_{D0}^+}{\mu K}.\tag{1.28}$$

The drift field describes the electric field that moves a charge carrier a distance $1/K$ during its lifetime. From τ_{die} one can see, that the build-up time for the conventional photorefractive effect is inverse proportional to the intensity I_0.

In the absence of an externally applied field ($E_0=0$), τ is a real number and $E_{sc}(t)$ grows exponentially. In the case of an applied electric field τ is complex and thus $E_{sc}(t)$ will oscillate as well as exponentially build-up with $\mathrm{Re}(\tau)$.

Interesting is the behavior of τ for very large and small grating spacings Λ. If Λ converges to infinity, which means homogeneous illumination, the rise time will converge towards the dielectric relaxation time τ_{die}, which allows to extract information on the photoconductivity σ_{photo}. To see the behavior of the rise time for very small grating spacings we can rewrite Eq. 1.25 as follows

$$\tau = \tau_{die}\frac{1 + (2\pi l_d/\Lambda)^2}{1 + (2\pi l_s/\Lambda)^2},\tag{1.29}$$

where $l_d = \sqrt{k_B T\mu/(e\gamma N_A)}$ is the diffusion length and $l_s = \sqrt{\varepsilon\varepsilon_0 k_B T/(e^2 N_{eff})}$ the Debye screening length. For small grating spacings $\tau \simeq \tau_{die}(l_d/l_s)^2$ it depends on which of the two length is dominating if the response time increases or decreases. This is shown in Fig. 1.6 with the solid line representing the case where l_s is shorter and the dashed for l_d being shorter. The diffusion length can be described as the average distance a charge
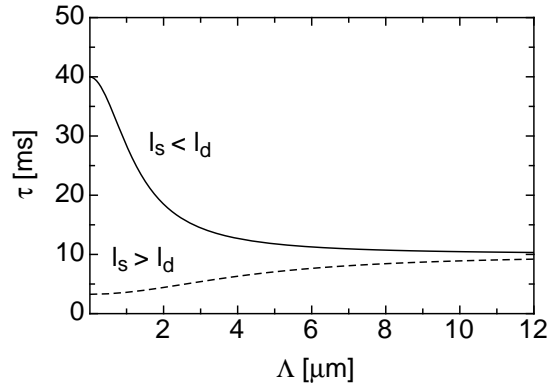
FIGURE 1.6: Simulation of the grating response time τ as a function of the grating spacing Λ for different values of l_d and l_s. The lines are according to Eq. 1.29. The figure shows nicely the convergence towards τ_{die} (10 ms) for large grating spacings and the different behavior for small grating spacings, depending on which length l_d or l_s is smaller.

carrier travels during its lifetime. The screening length is the distance needed to screen a charge field perturbation in the medium.

In many materials the measured build-up does not follow a perfect exponential curve, which is due to more complex trap level arrangements or the existence of several different charge carriers. Still the exponential approach offers in most cases a good enough description for the build-up of photorefractive gratings and allows for a comparison of the response times of different materials.

The decay of photorefractive gratings with time either in the dark (due to homogeneous thermal ionization) or under homogeneous illumination is the same as for the build-up process. It decays exponentially with the same time constant τ. In case of dark-decay it is governed by the dark conductivity σ_{dark} instead of the photoconductivity σ_{photo}.

Two wave mixing

Due to the non-local response of the charge grating with respect to the light intensity grating energy transfer between two interfering beams is possible. This is interesting for applications like beam cleanup coherent image amplification etc. Two wave mixing (TWM) is also often used as a simple experimental technique to evaluate the photorefractive properties of a material particularly for diffusion dominated charge transport. The experiment allows to probe the magnitude and the build-up time of the space charge field E_{sc} component that is $\pi/2$ shifted with respect to the intensity pattern. From the TWM measurement, the effective trap density N_{eff} (see Eq. (1.15)), which is mainly responsible for grating spacing dependence of the space charge field, can be determined.

In two wave mixing experiments, two coherent light beams, the signal beam with the intensity I_S and the pump beam with intensity I_P, interact in the photorefractive

medium. The nonlinear interaction between the two waves may result in energy or phase transfer between the beams.

The interference between the signal and pump beams produces an intensity pattern in the crystal, and a space charge field described by Eq. (1.12) builds up. If diffusion is the dominant charge transport mechanism for the photoexcited charge carriers, a refractive index grating is built up, which is exactly $\pi/2$ out of phase with respect to the intensity grating if no external field is applied. The pump beam is diffracted off the grating and the diffracted wave is either exactly in phase with the signal or out of phase. Therefore, the signal is either amplified or depleted. For $I_P \gg I_S$ (undepleted pump approximation) the measured energy transfer can be characterized by the exponential gain Γ which is defined as

$$\Gamma = \frac{1}{d} \ln \frac{I_S^{on}}{I_S^{off}} \, , \tag{1.30}$$

where I_S^{off} and I_S^{on} are the intensities of the transmitted signal beam before and after turning on the pump beam and d is the length of the path of the signal beam in the crystal along its energy propagation direction [18]. In chapter 5, TWM is used to determine the material properties r_{eff} and N_{eff} of $Sn_2P_2S_6$ in the bulk and waveguiding region, where a more explicit expression for Γ is given.

It is important to note, that the value of the coupling constant Γ is in the single-level band model independent of the intensity, since the absolute value of the space-charge field being responsible for the refractive index grating does not depend on the intensity (see Eq. 1.12). The only way to increase this field is by applying an external electric field as described in sec. 1.2.1. The only exception occurs, if the dark conductivity is similar to the photoconductivity and thus erases the written grating and weakens the effect. After a certain intensity the saturated regime, where the photoconductivity dominates, is reached. This can be a rather large intensity depending on the wavelength and the material, an example is discussed in chapter 4.

1.3   The interband photorefractive effect

The conventional model only considers photo-excitation of charges from one midgap impurity level to one of the conduction bands. Accordingly, the absorption constant is small and the excitation process rather slow (milliseconds to seconds). As shown in Fig. 1.2, other transitions are possible as well. Under light illumination with photon energies larger than the band gap, band-to-band transitions occur and dominate over impurity-to-band transitions. Because of a much higher absorption constant in this regime, many more free charge carriers are produced, thus leading to a much faster excitation process. This effect is known as the "interband photorefractive effect".

Basic equations

The most common set of equations describing the charge dynamics is given in [20], and includes one trap level in addition to direct band-to-band excitation. No thermal excitations and no photogalvanic current are considered. The following equations describe the processes illustrated in Fig. 1.2:

$$\frac{\partial N_D^+}{\partial t} = s_e I(N_D - N_D^+) + \gamma_h p(N_D - N_D^+) - \gamma_e n N_D^+ \tag{1.31}$$

$$\frac{\partial n}{\partial t} = s_{dir} I(N_V - p) + s_e I(N_D - N_D^+) - \gamma_e n N_D^+ - $$
$$- \gamma_{dir} np + \frac{1}{e} \boldsymbol{\nabla} \mathbf{J}_e \tag{1.32}$$

$$\frac{\partial p}{\partial t} = s_{dir} I(N_V - p) + s_h I(N_V - p) N_D^+ - \gamma_h p(N_D - N_D^+) - $$
$$- \gamma_{dir} np - \frac{1}{e} \boldsymbol{\nabla} \mathbf{J}_h \tag{1.33}$$

$$\mathbf{J}_e = en\boldsymbol{\mu}_e \mathbf{E}_{\text{sc}} + k_B T \boldsymbol{\mu}_e \boldsymbol{\nabla} n \tag{1.34}$$

$$\mathbf{J}_h = ep\boldsymbol{\mu}_h \mathbf{E}_{\text{sc}} - k_B T \boldsymbol{\mu}_h \boldsymbol{\nabla} p \tag{1.35}$$

$$\boldsymbol{\nabla} \mathbf{E}_{\text{sc}} = \frac{e}{\varepsilon_0 \varepsilon_{\text{eff}}} (N_D^+ + p - n - N_A) \tag{1.36}$$

The symbols have the same meaning as in Eqs. (1.5–1.8) whereas the newly added ones are defined as follows: p is the free hole concentration in the valence band, N_V is the density of electrons close enough to the top of the valence band to be photoexcited, J_h the hole current density, s_{dir} the photoexcitation constant for direct band-to-band phototransitions, γ_h the recombination constant for the hole-donor interaction, and μ_h the hole mobility. The mathematical complexity of this set of equations is already for one impurity level so high that no closed solution has yet been found. Analytic solutions for $\mathbf{E}_{\text{sc}}$ were found by applying some simplifications [20,21]. Here we present only the solution for pure interband regime, i.e. without considering any trap level ($N_D = N_D^+ = N_A = 0$), and without an external field. This limit well describes the effect for high light intensities, where the contribution from trap levels becomes negligible.

The resulting amplitude of the space charge field E_{sc} for a continuous sinusoidal illumination with a small light intensity modulation m is given by

$$E_{\text{sc}} = -i\,m\,\frac{E_{qf} E_D (E_{Rh} - E_{Re})}{(E_D + E_{Re} + E_{Rh})(E_D + E_{qf})} \tag{1.37}$$

where $E_D = K k_B T / e$ represents the diffusion field, E_{qf} the free carrier-limited field

$$E_{qf} = \frac{e}{\epsilon_{\text{eff}} \epsilon_0 K} \sqrt{\frac{gI_0}{\gamma_{dir}}}, \tag{1.38}$$

and $E_{Re,Rh}$ the electron (hole) recombination fields

$$E_{Re,Rh} = \frac{1}{K\mu_{e,h}} \sqrt{gI_0 \gamma_{dir}}, \tag{1.39}$$

where the constant $g = s_{dir} N_V = \frac{\alpha_{dir}}{h\nu}$ is related to the absorption constant α_{dir} in a crystal without any impurities divided by the photon energy $h\nu$. The recombination fields can be interpreted as the average electric field needed to drift one electron or hole by a distance $K^{-1} = \Lambda/2\pi$ before a direct band-to-band recombination takes place.

Eq. (1.37) is a little bit more complex than Eq. (1.12), valid for the conventional single level model. Different regimes dominated by one of the fields E_{qf}, E_D, E_{Rh}, and E_{Re} are possible. In interband photorefraction the steady state of the space charge field depends not only on the grating spacing Λ but also on the light intensity I_0. For high intensities ($E_{qf} \gg E_D$) and small grating spacings Λ, the E_{sc} will grow proportional to $\sqrt{I_0}$.

The dynamics of the build-up is given by a double exponential function [21], and the build-up time constants are proportional to

$$\tau_{ib} \propto \frac{1}{\sqrt{I_0}} \tag{1.40}$$

in the pure interband regime. The diffraction efficiency of interband gratings is given by (1.17), but with the interband space charge field (1.37) inserted in (1.20). This results, for small efficiencies, in

$$\eta \propto \left(\Delta n \, \tilde{d} \right)^2 \propto \left[\Delta n \, \ln \left(\frac{I_0}{I_{\text{ref}}} \right) \right]^2 \tag{1.41}$$

where $\tilde{d}$ is the thickness of the grating and I_{ref} is a reference intensity needed for normalisation. In (1.41) the grating is assumed constant until a certain thickness $\tilde{d}$, which is dependent on the illumination intensity, and then vanishing. This approximation has been shown to yield equal or better results than a model with an exponentially decreasing grating [20].

Usually interband photorefractive experiments are performed with ultraviolet light, since the bandgap of most photorefractive materials lies in that energy range. $Sn_2P_2S_6$ has a smaller bandgap of 2.3 eV and thus visible laser lines, such as of an Argon laser or a solid state frequency doubled Nb:YAG laser, can be used. More characteristic properties of this material are given in section 1.4.

Photoconductivity measurement

The photoconductivity in the interband regime can experimentally be determined by applying an electric field E (for example in the x direction), measuring the electric current I_{el} through the crystal and changing the light intensity in the transversal direction (z direction). This is however directly possible only in very thin plates because of the large absorption. The absorption is strongly reducing the incident light intensity I_0 along the direction z, perpendicular to the light incidence surface following

$$I_\alpha(z) = I_0 \mathrm{e}^{-\alpha z}. \tag{1.42}$$

17

The electric current J_{el} under illumination in an absorbing material is given by Ohm's law by

$$J_{el}(I_0) = \int_0^d E\sigma_{tot}(I_0 e^{-\alpha z}) b\,dz \qquad (1.43)$$

where b is the crystal dimension in the y-direction, d is the thickness in z-direction, and E is the applied electric static field. If the incident light intensity I_0 is increased by a small amount ΔI_0, the expression for the electric current can be rewritten as

$$J_{el}(I_0 + \Delta I_0) = \int_0^d E\sigma_{tot}(I_0 e^{-\alpha(z+\Delta z)}) b\,dz \qquad (1.44)$$

where the property

$$\Delta I_0 \approx -\alpha I \Delta z \qquad (1.45)$$

obtained by linearization of Eq. (1.42) was used. Calculating the difference $\Delta J_{el}(I_0) = J_{el}(I_0 + \Delta I_0) - J_{el}(I_0)$ between the electric currents, and after some rearrangement of the integration boundaries, we obtain

$$\Delta J_{el}(I_0) = Eb\left(\int_{\Delta z}^0 \sigma_{tot}(I_0 e^{-\alpha z})\,dz - \int_{d+\Delta z}^d \sigma_{tot}(I_0 e^{-\alpha z})\,dz\right). \qquad (1.46)$$

In the case of strong absorption ($d \gg 1/\alpha$) the total conductivity σ_{tot} in the second integral of Eq. (1.46) can be replaced by the intensity independent dark conductivity, which is defined as $\sigma_{dark} = \sigma_{tot}(I_0 = 0)$. Further for small light intensity changes ($\Delta I_0 \ll I_0$) the conductivity in the first integral of Eq. (1.46) can be assumed as constant over the integration range. For the photoconductivity $\sigma_{ph} = \sigma_{tot} - \sigma_{dark}$ we finally obtain

$$\sigma_{ph}(I_0) = -\frac{\alpha}{bE}\frac{\Delta J_{el}}{\Delta I_0/I_0} \qquad (1.47)$$

where we made use again of Eq. (1.45).

The photoconductivity in thick samples can therefore be calculated by the measurement of the $J_{el}(I_0)$ characteristic after numerical differentiation. An experiment is presented in appendix A where the method is used to determine the absorption constant of a $Sn_2P_2S_6$ and a $LiNbO_3$ crystal through photocurrent measurements.

1.4 $Sn_2P_2S_6$ crystals

1.4.1 Introduction

Tin hypothiodiphosphate ($Sn_2P_2S_6$) is a very interesting material for photorefractive, electro-optical and nonlinear optical applications. In the photorefractive field $Sn_2P_2S_6$ is characterized by a large beam coupling gain in the wavelength range $0.5\ldots 1.55\ \mu m$ and a relatively fast response, two orders of magnitude faster than $BaTiO_3$ doped with

rhodium, which is the usual photorefractive material in the near infrared. In electro-optics $Sn_2P_2S_6$ is useful because of its large electro-optical coefficients and their nearly absent dispersion in the near infrared. For example the diagonal electro-optical coefficient $r_{111} = 160\,\text{pm/V}$ at $\lambda = 1550\,\text{nm}$, which leads to a half-wave voltage 15-20 times smaller than in the standard material $LiNbO_3$. For nonlinear optics $Sn_2P_2S_6$ is interesting due to its large effective nonlinear optical coefficients with phase-matching in a transparency region ranging from 0.53 to 8μm.

An overview of $Sn_2P_2S_6$ is given in the chapter on this material in Ref. 22. We are mainly interested in the photorefractive properties of $Sn_2P_2S_6$ so we will describe these here first, and then pass on to the crystal's growth, structure and other properties in the next sections.

1.4.2 Photorefractive properties

Investigations of the photorefractive effect in $Sn_2P_2S_6$ started in 1991, when Grabar et al. first observed this effect in $Sn_2P_2S_6$ [23]. A few years later Odoulov et al. remarked that the photorefractive gain at 1.06μm can be enhanced considerably by pre-illuminating the crystal with white light [24,25]. A new step forward was made in 2001 when a new "brown" modification was obtained [26] and in 2003 with tellurium doped crystals, which both outperform normal "yellow" crystals in photorefractive gain and speed.

Although the excellent performance of $Sn_2P_2S_6$ makes it interesting for many applications, only little is known about the origins of the photorefractive response, considering both, charge transport and energy (trap) levels involved [22,27]. Nominally pure (yellow) $Sn_2P_2S_6$ crystals typically exhibit a great variation of parameters between different samples, and can be basically divided in two groups [22]. Crystals of type I show a pronounced electron-hole competition and a strong influence on preillumination and are of fundamental importance due to the unique electron-hole competing dynamics. Particularly, this allows to demonstrate a coherent optical oscillator with periodic zero- phase modulation [28] or the photorefractive slowing down of light [29]. On the other hand, for crystals of type II no considerable transient gain and preillumination influence are detected, and these samples are preferable for applications requiring a high steady-state photorefractive gain.

Different dopants have been used with the aim to enhance the photorefractive properties of $Sn_2P_2S_6$. Modification of the properties was achieved mainly with elements chosen from the respective groups in the periodic table of elements to substitute one of the three atoms Sn, S or P in the molecular structure. The most successful one being tellurium (Te). Doping by Te enhances the photorefractive response of the material significantly towards the infrared region [30]. $Sn_2P_2S_6$:Te presents photorefractive sensitivity without any additional enhancement methods at $\lambda = 1.55\ \mu$m, which is discussed in chapter 4. Self-pumped optical phase conjugation in these crystals was realized up to a wavelength of 1064 nm [31,32]. Doping with antimony (Sb) increases the photorefractive response in

the visible wavelength range at around $\lambda = 633$ nm and suppresses the infrared response of the material, which is desired, e.g., for electro-optic and nonlinear optical applications [30]. An other interesting dopant is bismuth (Bi) which shifts the lower absorption edge of the material by several hundreds nanometers towards the infrared, which is discussed in appendix C. The "brown" modified crystals offers very good photorefractive properties but is almost impossible to grow, since the growth conditions for this crystal are not fully understood. The main photorefractive parameters of pure, "brown", Te-doped and Sb-doped $Sn_2P_2S_6$ crystals are shown in Table 1.1, in comparison to some standard materials.

The lower absorption edge of $Sn_2P_2S_6$ is in the green wavelength region, allowing for interband photorefraction at visible wavelength. Widely available laser sources can thus be used, such as Argon lasers or frequency doubled Nd:YAG laser. This is an advantage to other materials such as $LiNbO_3$ or $KNbO_3$ which need UV laser sources for these kind of applications. Chapter 2 will offer more details on these properties.

TABLE 1.1: Typical photorefractive parameters of various $Sn_2P_2S_6$ crystals at two light wavelengths λ: α_x, absorption coefficient for x-polarized light; Γ_{max}, maximal two-wave mixing gain; τ, faster response time at a grating spacing of $1\,\mu m$ and scaled to a light intensity of $1\,W/cm^2$; N_{eff}, effective trap density [22, 30, 33]

$Sn_2P_2S_6$ sample	λ [nm]	α_x [cm^{-1}]	Γ_{max} [cm^{-1}]	τ [ms]	N_{eff} [$10^{16}\,cm^{-1}$]
Yellow	633	0.5	4–7	10–50	0.7
	780	0.2	2–5	100	0.2
	1064	0.1	0.9	-	0.04
Brown	633	5.7	38	4	2.5
	780	1.0	18	10	0.7
	1064	0.09	8.6	-	0.04
Te-doped (1%)	633	1.0	10	2.5	0.9
	780	0.4	6	7	1
	1064	0.09	4.5	25	0.53
	1550	<0.1	2.8	10	0.32
$LiNbO_3$ (SLN)	633	0.2	20	$(5\text{–}50)\cdot 10^4$	
$KNbO_3$	633	0.2	2–5	1–2	

1.4.3 Growth of $Sn_2P_2S_6$

The growth of the $Sn_2P_2S_6$ crystal was first described in 1970 by Nitsche et al. [34]. They reported the possibility that single crystals of many metal-phosphorous-sulfur compounds $Me_2P_2S_6$ (Me = Sn, Fe, Cd) can be grown by a vapor transport technique employing pure iodine. Stoichiometric amounts of the constituting elements and the transporter gas were
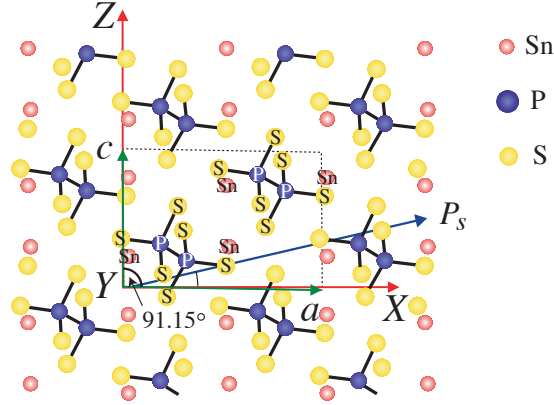
FIGURE 1.7: Schematic structure of Sn$_2$P$_2$S$_6$. The symmetry plane is parallel to the plane of the figure. The unit cell in the Dittmar notation is indicated by the dashed lines.

sealed into quartz ampoules and brought to reaction at 650°C–700°C. The ampoule was placed in the hot spot of a horizontal temperature gradient, while the crystal grows in the cold end (ca 20°C colder) by chemical transport. A possible reaction equilibrium for this transport is:

$$2(SnI_2)_{gas} + 0.5(P_4)_{gas} + 3(S_2)_{gas} \rightleftharpoons (Sn_2P_2S_6)_{solid} + 2(I_2)_{gas}$$
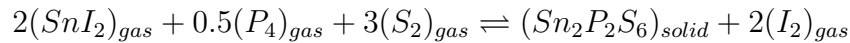
but other reactions, involving volatile phosphorous sulfides and/or phosphorus halides cannot be excluded [35]. Average growth times were of the order of 100 hours. Nowadays there are three different transporter agents used [22]: pure iodine I$_2$, SnI$_2$ and SnI$_4$. By changing the transporter agent and growth parameters (temperature, gradients, pressure...) crystals of different characteristics are obtained, with a color ranging from yellow, orange to brown, which is probably the consequence of their different (not-prefectly stoichiometric) composition [22].

1.4.4 The crystal structure

The structure at room temperature was investigated in Ref. [36] and at 110° in Ref. [37]. At room temperature the crystal has a ferroelectric [38] monoclinic structure with point group m [36], above the second order phase transition at $T_C = 66 \pm 2\,°C$ [39] the crystal is paraelectric and belongs to the monoclinic point group $2/m$.

The primitive cell is shown in Fig. 1.7 and is set according to the standard convention [40] that b is perpendicular to the mirror plane, and $c < a$, $\beta > 90°$, $\alpha = \gamma = 90°$. Then the translation vectors are $a = 9.375$ Å, $b = 7.488$ Å and $c = 6.513$ Å, and the angle β between a and c is $\beta = 91.15°$ [36]. Note that the crystal axis b is perpendicular to the plane of Fig. 1.7. The elementary cell has two P_2S_6 units. The whole structure shows a pseudossymmetry through a pseudo twist axis in direction [010]. The P_2S_6 unit is settled by two distorted trigonal PS_3 prisms which are related together through a P-P bond. The bases are rotated so that the whole symmetry is $3m$. The two Sn^{2+} cations are connected to the $(P_2S_6)^{4-}$ complex by ionic bonds.

The atoms of the unit cell have a space group Pn [37] at room temperature, since the atoms get onto each other by a translation by $(\frac{1}{2}, 0, \frac{1}{2})$ and successively a mirror operation about the y-plane. But note that all the macroscopic physical properties follow the point group symmetry, which is equal to the space group if one ignores the translations (which have no effect macroscopically).

The coordinate system chosen to describe the physical tensor symmetry is a right handed Cartesian x, y, z system. According to the standard of piezoelectric materials [40], the y-axis is perpendicular to the symmetry plane ($y \parallel b$), the z-axis is chosen parallel to the crystal c-axis and the x-axis perpendicular to y and z [22].

1.4.5 Spontaneous polarisation and other physical properties

Existence of ferroelectricity in $Sn_2P_2S_6$ was first reported in Refs. 38 and 41. It is given by movement of Sn atoms in a rigid P_2S_6 framework [37]. In crystals of class m the direction of the spontaneous polarisation $\mathbf{P}_S$ is not predictable, it must just lie in the (010) plane. $\mathbf{P}_S$ happens to lie between $+x$ and $+z$ [42], $(14 \pm 2)°$ from $+x$ [43]. The value for $\mathbf{P}_S$ was found to be 14 μC/cm^2 at 20°C and the coercitive field is 750 V/cm [41].

As-grown $Sn_2P_2S_6$ crystals are usually poly-domain. For electro-optical, photorefractive, nonlinear optical or piezoelectric applications crystals need to be poled. This is done by heating the sample well over the phase transition temperature $T_C = 66 \pm 2°$C and slowly cooling it down to room temperature under an applied electric field larger than the coercive field.

During heating of a poled sample, $\mathbf{P}_S$ decreases up to the critical temperature, where it goes to zero following the square root dependence typical for second order phase transitions [38].

We conclude this introduction to $Sn_2P_2S_6$ with an overview of its physical properties in Table 1.2.

TABLE 1.2: Basic physical properties of $Sn_2P_2S_6$ at room temperature. The tensor elements are in the coordinates defined in Ref. 42.

		Reference
Spontaneous polarization P_s	$15\,\mu C/cm^2$	[41, 44, 45]
Transparency range	$530\,nm - 8000\,nm$	[46], [47]
Main refractive indices[a]	$n_1 = 3.0256$	[42]
	$n_2 = 2.9309$	
	$n_3 = 3.0982$	
Dielectric constant ϵ_{11}	$230 - 300$	[48]
Electro-optic coefficient r_{111}^T[a]	$174\,pm/V$	[49]
Piezoelectric coefficient d_{111}	$244\,pC/N$	[50]
Density ρ	$3.54{\cdot}10^3\,kg/m^3$	[36]
Elastic constant C_{1111}	$4.2 \cdot 10^{10}\,N/m^2$	[51]
Pyroelectric coefficient p_1	$7 \cdot 10^{-4}\,C/(m^2\,K)$	[52]
Coercive field E_c	$7.5 \cdot 10^4\,V/m$	[41]
Heat capacity C_p	$240\,J/(mol\,K)$	[53]
Thermal conductivity λ_1	$0.5\,J/(s\,m\,K)$	[54]
Nonlinear optical susceptibility[b]	$\chi_{111}^{(2)} = 24\,pm/V$	[47]
	$\chi_{1111}^{(3)} = 17 \cdot 10^{-20}\,m^2/V^2$	[47]

[a]at $632.8\,nm$
[b]at $1907\,nm$

Chapter 2

Interband photorefraction in $Sn_2P_2S_6$ at visible wavelengths [†]

Continuous-wave photorefractive experiments in $Sn_2P_2S_6$ crystals and interband photorefraction at the visible wavelengths 514 nm and 488 nm are presented. Two-wave mixing and Bragg diffraction measurements at 514 nm show grating response times of around 100 microseconds at moderate light intensities of 0.6 W/cm^2, i.e. two orders of magnitude faster than measured in the same crystal in the conventional photorefractive regime. A large two-wave mixing gain of up to $\Gamma = 60 \pm 8 \, \text{cm}^{-1}$ is measured, and holes are identified as dominant charge carriers for the interband photorefractive effect.

2.1 Introduction

The interband photorefractive effect is characterized by a rapid charge redistribution upon inhomogeneous illumination, followed by an electro-optic change of the optical properties due to the generated space-charge electric field due to band to band photoexcitation of intrinsic charge carriers. Compared to the conventional photorefractive effect connected with photoexcitation from deep donor centers, the main advantages of the interband photorefraction are a much faster response and a strong robustness of the grating against illumination with sub band-gab photons [20, 56]. For the interband photorefractive effect intentional doping of the crystal in order to achieve efficient photocarrier generation from donor levels is not required since carriers are directly exited from intrinsic energy levels of the material. The interband photorefractive effect is very attractive for many applications because of the faster recording times. Recording times of less then 100 μs have been reported in $KNbO_3$ at 1 mW/cm^2 power levels [20]. It has already been implemented to demonstrate incoherent-to-coherent light converters [57], optical joint Fourier-transform correlators [58], fast dynamical light-induced waveguides [2] and tunable optical filters for wavelength division multiplexing [59].

[†]This chapter has been published in J. Opt. Soc. Am. B **23**, 1620 - 1625 (2006) [55]

Interband photorefraction has been studied previously in $KNbO_3$ [20] and $LiTaO_3$ [56], where ultraviolet (UV) light was used for the grating recording. For many practical applications, however, it would be more convenient to use visible instead of UV light due to the several advantages in terms of availability of laser sources, standard optical devices, easier detection etc. The availability of a material with large electro-optic response being suitable for interband photorefraction under visible illumination offers therefore very interesting perspectives. The material studied in this work, tin hypothiodiphosphate ($Sn_2P_2S_6$), fulfills all requirements for fast interband photorefraction at visible wavelengths due to its large electro-optic effects (e.g. $r_{111}^T = 174 \, pm/V$ at $\lambda = 633$ nm [49]) and the suitable band gap energy of E=2.3 eV.

$Sn_2P_2S_6$ is a monoclinic ferroelectric crystal with a broad transparent region ($0.53 - 8 \, \mu$m [47]). In the regime of the conventional photorefractive effect, it shows fast photorefractive grating recording times and large refractive index changes in the red and near infrared region [24, 26, 31, 32, 60, 61]. The possibility for fast hologram recording in $Sn_2P_2S_6$ via interband photorefraction under cw visible illumination was demonstrated recently in our preliminary experiments [62]. We have also measured the photoconductivity and determined the absorption coefficients at 488 nm and 514 nm [63]. In the pulsed regime, effects ascribed to the interband photorefractive effect were already used to demonstrate optical correlation at high repetition frame rates using the wavelength 532 nm [58].

In this paper we present photorefractive gratings in $Sn_2P_2S_6$ with very fast build-up times (less then 100 μs), recorded at visible green ($\lambda = 514$ nm) and blue ($\lambda = 488$ nm) light. The diffraction efficiency of a Bragg grating follows an intensity dependence as expected for the interband regime. The strong influence of the orientation of the optical indicatrix in the mirror plane of the monoclinic structure on the observed Bragg diffraction angle is predicted and experimentally verified. This phenomenon can be used to gain information on the material refractive indices within the high absorption region. Finally, two-wave mixing experiments permit to determine a very high effective exponential gain coefficients of up to 60 cm^{-1} for the wavelength of $\lambda = 514$ nm as a result of the strong photorefractive and electro-optic nonlinearity. This measurement also allowed us to determine the most mobile charge carriers in $Sn_2P_2S_6$.

2.2 Experimental

2.2.1 Sample preparation

$Sn_2P_2S_6$ single crystals were produced by the conventional vapor-transport technique [35] using iodine as a transporter. At room temperature $Sn_2P_2S_6$ has a ferroelectric monoclinic structure with point group m. In this work we use the coordinate system as defined in Ref. 42 with the z-axis parallel to the crystallographic c-axis, $y \parallel b$ normal to the mir-

ror plane, and x normal to y and z. The indicatrix is rotated in the xz-plane, and its rotation angle α_{ind} is defined as the angle between the x axis and the major principal axis of the indicatrix. This angle is wavelength and temperature dependent [42]. The poling was performed by heating the crystal above the second order phase transition at $T_C = 338 \pm 2$ K and slowly cooling it down to room temperature with an electric field of about 1 kV/cm applied along the x-direction. We used a bulk crystal and a thin z-plate. The dimensions of the thick $Sn_2P_2S_6$ crystal were $5.07 \times 5.38 \times 4.85$ mm^3 along the x, y and z axes respectively. The thin plate had dimensions $7.3 \times 8.3 \times 0.045$ mm^3 and was attached to a quartz substrate with a thickness of 3 mm. The single domain state was verified using the directional light scattering method described in Ref. 64.

2.2.2 Bragg diffraction and two-wave mixing

Bragg diffraction from photorefractive gratings was performed in a nondegenerate four-wave mixing configuration in the longitudinal geometry as illustrated in Fig. 2.1. In this geometry all three beams enter the crystal through the same surface and propagate in the xz plane. The experiments were performed with a writing beam from an Ar-ion laser at 514 nm and 488 nm (Coherent Innova 100, max. cw single-mode power 1 W) and a reading beam from a HeNe laser (max. cw power 5 mW). The absorption constant α at 488 nm is $2600 \pm 800 \, \text{cm}^{-1}$ for the x-polarization and $1730 \pm 70 \, \text{cm}^{-1}$ for the y-polarization, and at 514 nm $490 \pm 20 \, \text{cm}^{-1}$ for the x-polarization and $110 \pm 10 \, \text{cm}^{-1}$ for the y-polarization [63]. The recording light penetration depth $1/\alpha$ is therefore of the order of $4 - 200 \, \mu\text{m}$ for the wavelengths between $\lambda = 488$ and 514 nm, which means that the interaction length for the readout beam is quite short. The read out beam was p-polarized (in the xz plane) in all the measurements, while the writing beams were either p- or s-polarized. The diffracted probe beam (HeNe laser) had a wavelength of $\lambda = 633$ nm and thus a photon energy of $h\nu = 2.0 \, \text{eV}$, which is smaller than the band-gap energy in $Sn_2P_2S_6$ (2.3 eV). Therefore it is expected that the reading beam cannot influence the interband grating. An acousto-optical deflector was used to turn the recording beam on and off. After the crystal the diffracted beam power was measured with a photodiode.

For the two-wave mixing experiment we used the same setup as for the Bragg diffraction experiments without the read-out beam and introduced a filter (1%) to weaken one of the writing beams, which is then called the signal beam. For this experiment we used a thin $Sn_2P_2S_6$ plate of $45 \, \mu\text{m}$ thickness along the z-axis, obtained by polishing down the bulk crystal. After the sample we focused the beam on the photodiode, for collecting all the light passing through the absorbing thin plate.

The photoconductivity measurements show that the interband regime, in which the photoconductivity follows a square root intensity dependence [20], is reached at intensities above $1 \, \text{mW/cm}^2$ at 488 nm and $10 \, \text{mW/cm}^2$ at 514 nm [63]. In all the experiments in this work we have used higher intensities, therefore we consider that at the intensity levels used in the present measurements the main contribution comes from gratings associated

to mobile carriers and not carriers from deep traps. In general, deep trap gratings might be formed deeper inside the crystal where the intensity becomes lower, as observed previously in $KNbO_3$ [20] and $LiTaO_3$ [56].
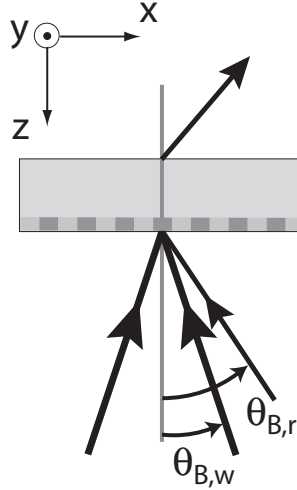

FIGURE 2.1: Experimental configuration and crystal orientation for longitudinal Bragg diffraction measurements. The grating is written by two recording beams at 514 nm or 488 nm incident symmetrically with respect to the sample normal at angles $\pm\theta_{B,w}$. The read-out beam at 633 nm is here on the right side with respect to the sample normal, later we refer to this configuration as "read-out from the right side", corresponding to positive angles $\theta_{B,r}$. "Read-out from the left side", corresponding to negative angles $\theta_{B,r}$, means that the read out beam is on the left side with respect to the sample normal, according to the crystal orientation indicated on the scheme.

2.3 Results and discussion

2.3.1 Bragg diffraction

Determination of the Bragg angle

The external Bragg angle $\theta_{B,r}$ of the reading beam can be calculated by

$$\sin\theta_{B,r} = \frac{\lambda_r}{\lambda_w}\sin\theta_{B,w} \tag{2.1}$$

if the writing beams are incident symmetrically to the sample, and $\theta_{B,w}$ is the external incidence angle of the writing beam, λ_r the read-out beam wavelength and λ_w the writing beam wavelength. For $Sn_2P_2S_6$ this equality will in general not hold because the indicatrix is rotated in the xz-plane and therefore the main axes are not perpendicular to the crystal surface. Additionally this rotation changes with the wavelength ($\alpha_{ind}^{514\,nm} = 39.9°$,

$\alpha_{\text{ind}}^{633\,\text{nm}} = 43.3°$) [42]. We chose p-polarized read-out beams, since the effective electro-optical coefficient is then closer to r_{111}^T, which is the largest coefficient in this material [49]. This implies, however, that the rotation of the indicatrix has to be taken into account in every measurement, as explained in the following.

Let us first consider the case where also the two writing beams are polarized in the plane of the incidence. In this case the two writing beams have different refractive indices in the crystal and therefore the grating fringes are not perpendicular to the surface of the crystal. This effect modifies the Bragg angle from Eq. (2.1), and the direction of the Bragg angle shift is determined by the direction of the optical indicatrix with respect to the direction of the incident beams.

In the second case the writing beams are s-polarized. In this case both writing beams have the same refractive index and the grating fringes are perpendicular to the surface. However, there will be still a shift of the Bragg angle with respect to Eq. (2.1), due to the p-polarized read-out beam, for which the refractive index will be different if coming from the left or from the right side with respect to the sample normal.

Fig. 2.2 shows the measured diffraction efficiency η as a function of the incidence angle $\theta_{B,r}$ of the read-out beam for writing beams polarized in the incidence plane entering at $\theta_{B,w} = 15.9°$. The measured diffraction efficiency has been approximated with the theoretical dependence obtained for phase-only transmission gratings [17, 18]:

$$\eta = \frac{\sin^2(\nu^2 + \xi^2)^{1/2}}{(1 + \xi^2/\nu^2)} \exp(-\alpha d), \tag{2.2}$$

with

$$\xi^2 = \frac{\Delta k_r^2}{4} \tilde{d}^2, \tag{2.3}$$

and

$$\nu^2 = \left(\frac{\pi \Delta n \tilde{d}}{\lambda_r (\cos(\theta_i) \cos(\theta_d))^{1/2}} \right)^2, \tag{2.4}$$

where d is the thickness of the crystal, $\tilde{d}$ the thickness of the grating, θ_i and θ_d the internal angles of the Poynting vectors of the incoming and diffracted waves respectively, Δk_r the wavevector mismatch and Δn the effective refractive index modulation amplitude. Similar measurements have also been performed for s-polarized writing beams at $\lambda = 514\,\text{nm}$ and $\lambda = 488\,\text{nm}$. In Table 2.1 the values for the external Bragg angles calculated from the known refractive indices [42] and the measured values are presented. The calculation of the Bragg angle is very sensitive to the values of the refractive indices, which were extrapolated from Sellmeier parameters obtained from data outside the absorption regime ($\lambda = 550 - 2300\,\text{nm}$). Still the calculated and the measured angles match very well. This indicates also that the refractive indices can be extrapolated very accurately with a Sellmeier formula from Ref. 42 to lower wavelengths until at least 488 nm. The
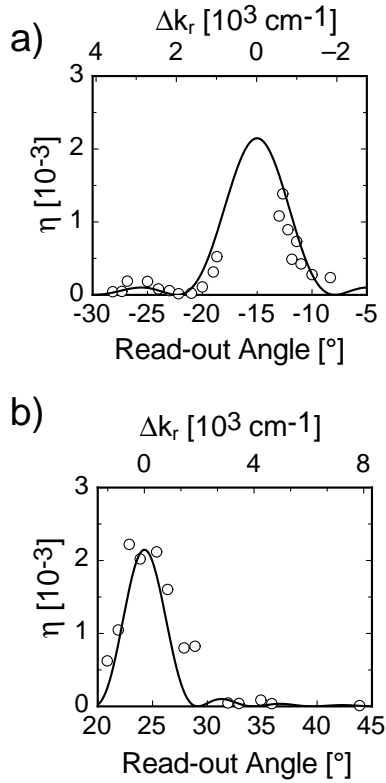
FIGURE 2.2: Diffraction efficiency η as a function of the read-out angle and the wavevector mismatch Δk, for a) read-out from the left side and b) read-out from the right side (see Fig. 2.1). All the beams, the writing and the read out beams, were p-polarized. The solid curves are given by Eq. (2.2) using the same parameters for both curves and correspond to a grating thickness $\tilde{d} = 30\,\mu$m, $\lambda_w = 514\,$nm, $\Delta n = 3.0 \times 10^{-4}$, $\Lambda = 0.94\,\mu$m, $\theta_{B,r}^{left} = -15.0\,^\circ$ and $\theta_{B,r}^{right} = 24.3\,^\circ$. The total writing intensity was $I_w = 460\,$mW/cm^2.

error for the refractive indices used to calculate the Bragg angles is ± 0.015, resulting from the error in the determination of the Bragg angle of $\pm 1°$.

The direction of the $+x$-axis is $15°$ off the direction of the polar axis (see Fig. 2.3), the direction of the $+z$-axis is more difficult to determine [42]. The direction of the shift of the Bragg angle from Eq. (2.1) can be used to determine the direction of the $+z$-axis with respect to the entrance surface. As a recipe, with the $+x$ axis pointing to the right, the $+z$-axis is in the backward direction if a larger Bragg angle is measured for a read-out beam coming from the right than for one coming from the left. The resulting $+z$-axis (defined as in Ref. 42) is shown in Fig. 2.3.
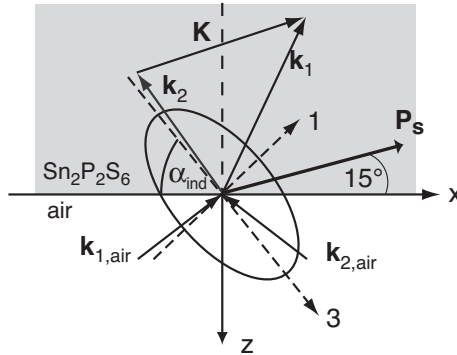

FIGURE 2.3: The orientation of the indicatrix, x- and z-axis as determined from the Bragg diffraction measurements. The z-axis is pointing out of the crystal. $\mathbf{k}_{1,air}$ and $\mathbf{k}_{2,air}$ are the incident writing wave vectors, $\mathbf{k}_1$ and $\mathbf{k}_2$ the wave vectors in the crystal, $\mathbf{K}$ the grating vector and α_{ind} the rotation angle of the indicatrix.

TABLE 2.1: Measured external Bragg angles $\theta_{B,r}$ for the p-polarized read-out beam compared to the Bragg angles calculated with taking into account the rotation of the indicatrix and without rotation.

λ [nm]	Position of the read-out beam	Writing pol.	$\theta_{B,r}$ [°]		
			calc. with Eq. (2.1)	calculated	measured
514	left side	p	-19.6	-14.9	-15.0
514	right side	p	19.6	24.6	24.3
514	left side	s	-19.6	-24.1	-24.0
488	left side	s	-20.8	-25.2	-25.3

Intensity dependence

The dependence of the Bragg diffraction efficiency on the intensity of the writing beam was studied with both p- and s-polarized writing beams and at the wavelengths of 488 nm

and 514 nm. The intensity of the writing beams was changed with a filter in front of the crystal and the intensity of the read-out beam was $I_{HeNe} = 130\,mW/cm^2$.

The diffraction efficiency defined as the ratio between the diffracted and the incident light intensities is shown in Fig. 2.4 as a function of intensity for $\lambda = 488\,nm$ and s-polarization. This relation can be approximated by [20]

$$\sqrt{\eta} \simeq \frac{\pi \Delta n}{\lambda \alpha} \ln\left(\frac{I_0}{I_{ref}}\right), \tag{2.5}$$

where Δn is the average amplitude of the refractive index change, α is the absorption constant at the wavelength of the writing beams, I_0 is the total incident writing intensity, and I_{ref} is a reference intensity needed for normalization. This behaviour is expected if we assume that increasing the writing intensity increases the effective thickness of the grating and that the depth dependence of the grating is a step function. In $KNbO_3$ similar interband effects have been observed and the step function depth dependence was shown to describe the experimental results better than an exponential decrease [20]. The straight line in Fig. 2.4 is a good indicator that we are in the interband regime.
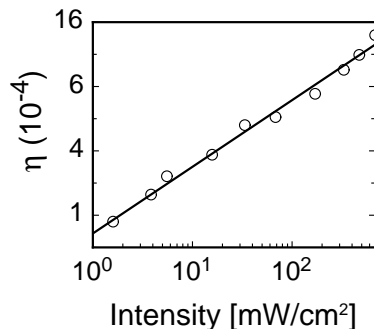

FIGURE 2.4: Intensity dependence of the diffraction efficiency (on a square-root/logarithmic scale). The theoretical line is according to Eq. (2.5) with parameters $\alpha = 1730\,cm^{-1}$ (from Ref. 63), $\Delta n = 1.2 \times 10^{-4}$, $I_{ref} = 0.2\,mW/cm^2$. ($\lambda = 488\,nm$, writing beams are s-polarized, read out beam is p-polarized. Grating spacing $\Lambda = 0.9\,\mu m$.)

Dynamics of the grating build up

One of the main advantages of interband photorefractive effects is the timescale for the build-up of the grating. In order to measure the dynamics of the build-up we used an acousto-optic deflector with a rise time of less than 0.5 μs to ensure a fast switching of the laser beam. Fig. 2.5 shows the diffraction efficiency of the grating for $\lambda = 633\,nm$ p-polarized light after turning on the writing p-polarized beams at $\lambda = 514\,nm$ and two different total intensities.

The dynamics of the diffraction efficiency cannot be explained with a simple model, because the intensity of the writing beam is exponentially decreasing with the depth

inside the crystal. For the build up of the holographic grating this means that the build up time, the amplitude and the phase of the grating will depend on the depth. The diffracted beam at the back side of the crystal is formed by the coherent sum of all the amplitudes of the diffracted light at different depths. For a model with several time constants the measured curves are not described significantly better, than for just one parameter. The build-up was therefore modeled with a semi-heuristic exponential function of the form

$$\eta = \eta_1 \Big(1 - \exp(-t/\tau) \Big)^2. \qquad (2.6)$$

This yields a time constant for the grating build-up τ (see Fig. 2.5). For 320 mW/cm^2 writing beam intensity $\tau = 125\,\mu$s, and for 650 mW/cm^2 $\tau = 80\,\mu$s, which is as expected faster for the higher writing beam intensity.
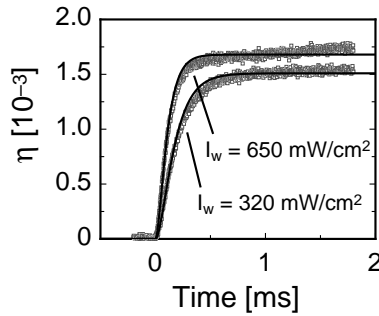

FIGURE 2.5: Grating build-up dynamics for two different writing intensities at $\lambda = 514\,$nm. The read-out beam intensity was 130 mW/cm^2, grating spacing $\Lambda = 1.0\,\mu$m, and both the read-out and the writing beams p-polarized. The solid lines are according to Eq. (2.6) with the build-up times of $\tau = 125\,\mu$s for 320 mW/cm^2 and $\tau = 80\,\mu$s for 650 mW/cm^2.

The measured build-up at $\lambda = 514\,$nm where $\alpha = 490\,$cm^{-1} is very fast compared to typical build-up times measured in brown Sn$_2$P$_2$S$_6$ at $\lambda = 633\,$nm for 1 W/cm^2, which is $\tau = 5 - 50\,$ms. It is also more then two orders of magnitude faster than in LiTaO$_3$ in the interband regime at about the same writing intensity and $\lambda = 257\,$nm where $\alpha = 270\,$cm^{-1} (Ref. 56) and almost as fast as in KNbO$_3$, where build up times of about 10 μs were obtained in transversal geometry at 1 W/cm^2 and $\lambda = 351\,$nm but a much higher absorption ($\alpha = 1900\,$cm^{-1}) and with an applied external applied field for an enhancement of the diffraction efficiency [65].

2.3.2 Two-wave mixing in a thin plate

Two-wave mixing experiments in the interband regime allow for the determination of the most mobile charge carriers and the verification of the amplitude of the refractive index change Δn. The experiments were performed in a $45\,\mu$m thick Sn$_2$P$_2$S$_6$ plate, with p-polarized light of wavelength $\lambda = 514\,$nm, a total intensity of $I_0 = 373\,$mW/cm^2

(pump beam = 370 mW/cm^2, signal beam = 3 mW/cm^2) and a grating spacing of $\Lambda = 1\,\mu$m. In the Bragg diffraction experiments described in section 2.3.1 we measured an effective grating thickness of $\tilde{d} = 30\,\mu$m for a similar writing intensity. For simplifying the calculation of the two wave mixing gain we make an assumption of a constant amplitude grating of the same thickness, and no two-wave mixing interaction below $\tilde{d} = 30\,\mu$m. This is justified by the fact that deeper in the crystal the grating cannot be formed because the dark conductivity dominates over the photoconductivity induced by the not yet absorbed photons. Therefore we can estimate the lower limit of the gain coefficient as

$$\Gamma = \frac{1}{\tilde{d}} \ln \frac{I_{\text{w/ pump}}}{I_{\text{w/o pump}}} \,, \tag{2.7}$$

where $I_{\text{w/ pump}}$ and $I_{\text{w/o pump}}$ are respectively the signal beam intensities with and without the pump beam turned on. The two-wave mixing gain can be related to an effective refractive index change Δn as

$$\Gamma = \frac{4\pi}{\lambda \cos \theta_s} \Delta n \,, \tag{2.8}$$

where θ_s the internal incidence angle of the signal wave.

The result of $\Gamma = 60 \pm 8\,\text{cm}^{-1}$ with a grating spacing of 1 μm shows a very high gain in the visible and the corresponding refractive index contrast $\Delta n = (2.4 \pm 0.5) \times 10^{-4}$ corresponds well to the value of Δn calculated from Bragg diffraction in section 2.3.1. In the conventional photorefractive regime at $\lambda = 633\,\text{nm}$ the maximal gain reaches about 7 cm^{-1}. The high gain in the interband region can be explained by two factors. First the number of effective charge carriers $N_{eff}(\lambda)$ increases with decreasing wavelength as observed in the transparent region [31], second also the electro-optic coefficient $r(\lambda)$ increases as one approaches the absorption edge [49].

In order to verify the true two-wave mixing origin of the energy transfer we rotated the plate by 180° around the y axis, so that the spontaneous polarization was inverted. We measured in this case a weakening of the signal beam, as expected for photorefractive two-wave mixing. If the signal beam gets amplified with the spontaneous polarization pointing in direction of the amplification, the most mobile charge carriers are holes, since the corresponding electro-optic coefficient is positive [49]. This is the situation that occurs in $Sn_2P_2S_6$, so the main charge carrier is the same as has been identified for conventional photorefraction [49, 61]. In the case of the interband photorefraction this implies that $\mu_h > \mu_e$, where μ_h is the mobility of the holes and μ_e the mobility of the electrons [20, 66].

2.4 Conclusions

We have investigated and analyzed the interband photorefractive effects in $Sn_2P_2S_6$ at visible wavelengths. This allowed us to determine an average refractive index change of $\Delta n = (3 \pm 0.3) \times 10^{-4}$ at $\lambda = 514\,nm$. Due to the rotation of the indicatrix we observed a considerable shift of the Bragg angle, which allowed to determine the refractive indices in the interband regime and determine the direction of the $+z$ axis in the crystal.

The build-up time constants of the interband photorefractive effect are in the order of 100 μs at an intensity of 0.6 W/cm^2 and therefore more than two orders of magnitude shorter than for the conventional photorefractive effect at $\lambda = 633\,nm$ at the same intensity level. Additionally the effect is observed around $\lambda = 530\,nm$, easily accessible by compact all solid state laser sources.

With a thin plate of $Sn_2P_2S_6$ two-wave mixing effects at a wavelength of $\lambda = 514\,nm$ were demonstrated with a very high gain coefficient of $\Gamma = 60 \pm 8\,cm^{-1}$ for p-polarized light. We concluded that the most mobile charge carriers at this wavelength are holes, and therefore $\mu_h > \mu_e$.

Interband holography in $Sn_2P_2S_6$ proves therefore to be an important tool, not only for applications in fast parallel coherent optics, but also as an experimental technique allowing to access and determine material parameters in the high absorption region.

Chapter 3

Fast dynamic waveguides and waveguide arrays in photorefractive $Sn_2P_2S_6$ [†]

We report on dynamic waveguides and waveguide arrays induced beneath the surface of electro-optic $Sn_2P_2S_6$ crystals by visible light at 514 nm. The waveguide structures are generated by interband photoexcitation and drift or diffusion charge transport mechanism. These structures are probed nondestructively in the transverse direction with a beam at a longer wavelength. We measured the fastest formation of light induced waveguides in the visible up to now. The recording times are below 200 μs for intensities above 0.1 W/cm^2. By interfering two light beams, dynamic waveguide arrays are generated with waveguide spacings of 7μm. If an electric field is applied to the crystal, these arrays can be spatially shifted by 1.5 μm for an applied field of $E_0 = 1$ kV/cm.

3.1   Introduction

Waveguides are the basic elements in integrated optical applications [67]. Many of these applications like optical switching, routing or dynamic optical interconnections require fast switching between waveguide channels. This is normally done electro-optically by applying complicated electrode configurations on permanently structured waveguides. Several techniques based on light-induced refractive index changes have been recently proposed [2, 68–70]. The most interesting feature of these waveguides is that they can be dynamically reconfigured, and thus signals can be routed by solely changing the light illumination.

Periodic dielectric structures such as photonic crystals or photonic lattices have recently gained a lot of interest due to their exciting features like controlling and manipulating the propagation and manage the diffraction of optical beams [70–72]. In

---

[†]This chapter is accepted for publication in Opt. Express (2009)

photorefractive crystals, a periodic modulation of the refractive index can be induced dynamically by interfering two or more light beams inside the crystal. For investigations of light propagation in periodic lattices, strontium-barium-niobate (SBN) is the most extensively employed material due to its high electro-optic activity ($r_{33} = 235$ pm/V for SBN:60, $r_{33} = 1340$ pm/V for SBN:75 at $\lambda = 0.5~\mu$m) [73]. However, the photorefractive response times of SBN in the visible are in the order of a few seconds [73], which makes this material not suitable for applications, where short waveguide formation times are required.

In this work, we investigate the potential of tin hypothiodiphosphate ($Sn_2P_2S_6$) for dynamic waveguide applications. $Sn_2P_2S_6$ is a semiconducting ferroelectric material with interesting optical and nonlinear optical properties: high photorefractive efficiency in the infrared up to the telecommunication wavelength 1.55 μm [33, 74, 75] and a large electro-optic coefficient ($r_{111} = 174$ pm/V at 633 nm [49]). Furthermore, the photorefractive response of $Sn_2P_2S_6$ in the near-infrared is very fast, more than two orders of magnitude faster than in any other photorefractive ferroelectric crystal as e.g. Rh-doped $BaTiO_3$ [32]. Recently, photorefractive self-focusing at 1.06 μm was demonstrated in bulk Te doped $Sn_2P_2S_6$ crystals with 15 ms response time at peak intensities of 160 W/cm^2 [76].

The photorefractive response time can be decreased, if light with photon energy larger than the band gap of the material is used [20]. In this so-called interband photorefractive effect, refractive index structures can be generated by charge redistribution between the bands, which in general provides 2-3 orders of magnitude faster response than the conventional effect.

So far, light induced waveguides were demonstrated in $KNbO_3$ [2] and Mg doped $LiTaO_3$ [69] by interband photorefraction with controlling light at ultraviolet (UV) wavelengths. However, there are some drawbacks of using UV light such as availability of laser sources, need of special optical elements and coatings to mention a few. $Sn_2P_2S_6$ has a band gap energy of $E = 2.3$ eV, which is lower than in conventional photorefractive crystals and enables interband photorefraction already in the visible at $\lambda = 514$ nm [55].

In this work we show that fast reconfigurable waveguides and waveguide arrays can be induced beneath the surface of $Sn_2P_2S_6$ crystals by using band-to-band excitations. The waveguiding structures are written beneath the surface in regions illuminated by 514 nm light by drift or diffusion of charge carriers, dominated by hole charge transport. They are probed nondestructively in transverse direction.

3.2 Light induced waveguides

The experiments were performed in a 6.8 mm long $Sn_2P_2S_6$ crystal oriented as shown in Fig. 3.1. The sample was nominally pure, to minimize the possibility of deep level trapping [20]. The use of interband light provides a faster effect, but on the other hand also a higher absorption for the controlling light. The absorption in $Sn_2P_2S_6$ is $\alpha = 490$ cm^{-1} at the controlling wavelength of $\lambda_{CL} = 514$ nm [55]. Therefore, the

waveguide reaches a depth of only a few ten micrometers below the surface and the crystal needs sharp edges for in- and out-coupling of the guided light. Since the structures are written between the bands, readout at sub band-gap wavelengths as e.g. red or telecommunication wavelengths, does not disturb the waveguide structures.

The illumination of the crystal is shown in Fig. 3.1a). The controlling light (Argon Ion Laser @ 514 nm) homogeneously illuminated a mask that was imaged onto the crystal z-surface by appropriate optics (not shown in the figure). The probe beam (HeNe @633 nm) traveled along the crystalline y-direction and was focused onto the input face of the crystal by a spherical lens ($f = 40$ mm) to a diameter of $2w_0 = 22$ μm. An out-coupling lens imaged the output face onto a CCD-camera. In order to excite an eigenmode, the readout beam was polarized along the dielectric 3-axis at an angle of $\psi = 43°$ with respect to the x-axis according to the orientation of the indicatrix in $Sn_2P_2S_6$ [49,75]. The controlling light was polarized in x-direction and an electric field was applied along x as well. For this configuration, we get an effective electro-optic coefficient of $r_{\mathrm{eff}} = r_{111} \sin^2 \psi + r_{331} \cos^2 \psi + r_{131} \sin 2\psi = 183\mathrm{pm/V}$ using the coordinate system as defined in [75]. Uniform background illumination at 514 nm produced a homogeneous conductivity that is needed for a better confinement of the waveguides [69].

The basic process for inducing a step index profile in photorefractive crystals is schematically shown in Fig. 3.1b). i) is the unperturbed state with a uniform refractive index n_0. In a first step (ii) an electric field E_0 is applied, which homogeneously decreases the refractive index via the electro-optic effect to a value of $n' = n_0 - \frac{1}{2}n_0^3 r_{\mathrm{eff}} E_0$. Finally, the controlling light is switched on (iii) and electrons are excited to the conduction band. Free charges, electrons in the conduction band and holes in the valence band, drift and screen the applied electric field in the illuminated region. This results in an electric field pattern that is correlated to the pattern of the controlling light. Thus, a refractive index structure is produced, which has its maximum in the illuminated regions. For the simple case of a slit mask, we get a 1D planar waveguide [2,69].
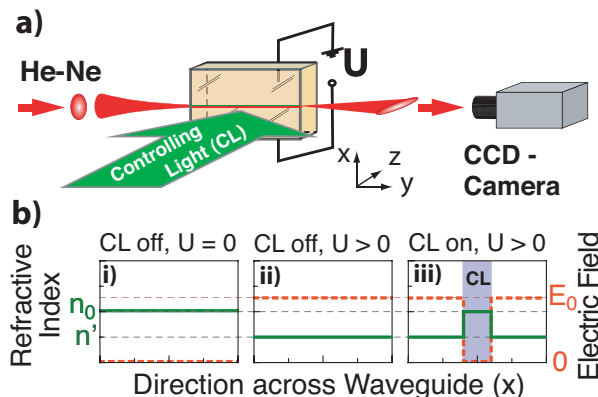

FIGURE 3.1: a) Arrangement for recording light induced waveguide structures. b) Simplified electric field (dashed red) and refractive index (solid green) distribution in a photorefractive crystal during the formation of the waveguides. Explanation is given in the text.
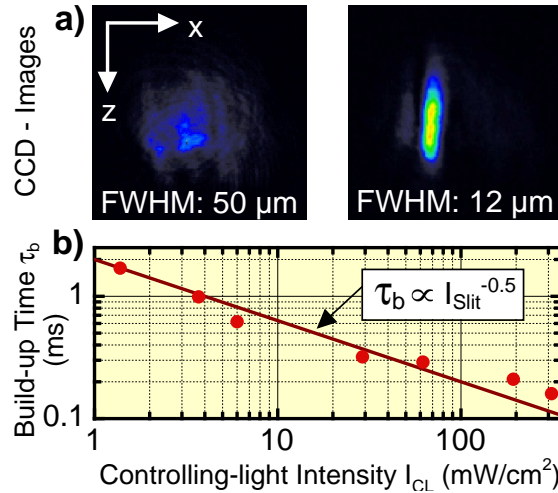
FIGURE 3.2: a) CCD-images of the output face of a 6.8 mm long SPS crystal without (left) and with (right) a photoinduced waveguide. b) Build-up times τ_b of the light induced waveguide as a function of the controlling light intensity.

Fig. 3.2a) shows the output of a 6.8 mm long pure $Sn_2P_2S_6$ crystal. A straight slit was imaged onto the crystal z-surface to a width of 17 μm in x-direction. Compared to previous experiments in $KNbO_3$ or $LiTaO_3$, much smaller fields are required due to the large electro-optic coefficient of $Sn_2P_2S_6$ (Table 3.1). In our experiments, the applied electric field was $E = 900$ V/cm, which resulted in a refractive index change of $\Delta n = 2.3 \times 10^{-4}$. The profile of the guided light perfectly matches a $\cos^2$-function, for the first waveguide-mode, with a FWHM of 12 μm, which is in good agreement with the expected FWHM of 11 μm for the given index profile.

The build-up times τ_b of light induced waveguides in $Sn_2P_2S_6$ as a function of the controlling light intensity are shown in Fig. 3.2b). The response is very fast, with $\tau_b <$ 200 μs for intensities above 0.1 W/cm^2. As listed in Table 3.1, this is two times faster than the build-up times observed in $KNbO_3$ [2] and more than one order of magnitude faster than the build-up times measured in $LiTaO_3$ [69] for recording with the same intensity but in the UV. The build-up times were determined by recording the temporal evolution of the peak intensity of the output light. This was measured using a photodiode and a 100 μm pinhole in the image plane of the out-coupling lens. The square-root intensity dependence of the build-up times confirms the interband nature of the structure formation [20].

3.3 Light induced waveguide arrays

We further demonstrated optically induced waveguide arrays in $Sn_2P_2S_6$ at the interband wavelength $\lambda_{CL} = 514$ nm. For this we used a crystal with a length of 15 mm along the propagation direction (y). The array was induced by interfering two light beams that generated an interband photorefractive grating beneath the z-surface of the crystal. Such a structure represents a waveguide array with a waveguide spacing equal to the grating spacing Λ and a waveguide with of $d \approx \Lambda/2$. In our set-up we had $\Lambda \approx 7$ μm which

Table 3.1: Parameters for the recording of interband light induced waveguides in LiTaO$_3$ [69], KNbO$_3$ [2] and Sn$_2$P$_2$S$_6$[this work]

Material	λ_{CL}	n_0	r_{eff}	α	E_0	Δn	τ_b
LiTaO$_3$	257 nm	2.18	31 pm/V	690 cm^{-1}	5.5 kV/cm	0.88×10^{-4}	16 ms
KNbO$_3$	364 nm	2.17	55 pm/V	550 cm^{-1}	4.8 kV/cm	1.34×10^{-4}	0.4 ms
Sn$_2$P$_2$S$_6$	514 nm	3.1	183 pm/V	490 cm^{-1}	0.9 kV/cm	2.5×10^{-4}	0.2 ms

λ_{CL}: Recording wavelength, n_0: Refractive index, r_{eff}: Electro-optic coefficient, α: Absorption @ λ_{CL}, E_0: Electric field, Δn: refractive index change, τ_b: Build-up Time at I$_{\mathrm{CL}}$=0.1W/cm^2. n_0, r_{eff}, Δn and τ_b are values for readout at 633 nm in the respective configuration.

yielded a modulation depth in the x-direction of $\Delta n = 1.0 \times 10^{-4}$ for the readout light at $\lambda \approx 633$ nm, as determined by Bragg diffraction measurements [55].

Different than in the single waveguide experiments described above, the array structures could be created only by diffusion of charge carriers without the background illumination. If an additional electric field was applied to the crystal, a combination of diffusion and drift was responsible for the formation of the waveguide arrays.

In optically induced photonic lattice experiments, where SBN was used, the controlling and probe light traveled in the same direction [71]. This was possible, because the lattices were written using photon energies below the band gap of the material, which implied a much lower absorption for the controlling light, but also a slower effect.

Here we probed the array in transverse direction since the structures are written in a layer a few ten micrometers beneath the surface, similar to the light induced waveguide experiments in the previous section. The light was coupled into the array with a 20x microscope objective. A cylindrical lens ($f = 200$ mm) was placed into the path of the probe beam, to minimize diffraction in the z-direction. The size of the read-out beam in the x direction was $2w_x = 12\mu$m, so that the input-beam covered about two waveguides. The output after 15 mm propagation was again monitored by the CCD - camera and is shown in Fig. 3.3a). Without the array, the beam diffracted to $2w_x = 330\mu$m. With the array, the input beam was distributed among several waveguides, as shown in Fig. 3.3a). The build-up time of these waveguides was $\tau_b = 225$ μs for controlling light intensity of 0.1 W/cm^2.

An additional electric field E_0 applied in the $+x$-direction of the crystal could shift the whole waveguide array by an amount of $\Delta x \approx -1.52\mu$m $= -0.21$ Λ (Fig. 3.3b), Λ being the waveguide spacing. This can be explained by the fact, that the refractive index grating is phase shifted with respect to the light illumination. This phase shift strongly depends on the applied electric field and on the type of dominant charge carriers (e$^-$ or h$^+$). This shift can be estimated by evaluating the complex space charge electric field E_{sc} which is responsible for the refractive index grating. The free carrier model from Ref. [20] can be simplified for large grating spacing $\Lambda \gtrsim 1\mu$m and an applied electric field smaller than the recombination field of the dominant charge carriers, i.e. the average

internal electric field in which the charges drift for an average distance $K^{-1} = \Lambda/2\pi$ before recombination. In our configuration this is true for $E_0 \ll 20$ kV/cm considering the results of the Bragg diffraction measurements [55]. We furthermore consider only one type of charge carriers. This is eligible if one of the mobilities is much larger than the other one, i.e. $\mu_e \gg \mu_h$ or $\mu_h \gg \mu_e$ for electron or hole dominated charge transport respectively. This simplification yields the following relation for the space charge field:

$$E_{sc} \approx im\frac{E_{qf}(\mp E_D + iE_0)}{2E_{qf} \mp iE_0} \tag{3.1}$$

where $E_D = Kk_BT/e$ is the diffusion field and $E_{qf} = \frac{e}{\epsilon\epsilon_0 K}n_0$ is the maximum electric field that can be created by free charge carriers; m grating modulation depth, k_B Boltzmann constant, T absolute temperature, e elementary charge, ϵ_0 vacuum permittivity and $\epsilon = 230$ [75] the dielectric constant of $Sn_2P_2S_6$. The charge density n_0 depends on the intensity of the writing light I_0 and can be determined by measuring the buildup times of the array for different writing intensities. We estimated the charge density to $n_0 \sim 2.3 \times 10^{16}$ cm^{-3} for $I_0 = 100$ mW/cm^2. The upper signs in Eq. 3.1 are for electron and the lower signs for hole dominated charge transport respectively.

From Eq. 3.1 we can calculate the phase shift of the space charge field with respect to the interference pattern ($\phi = \text{Arg}(E_1)$):

$$\tan\phi \approx \pm\frac{2E_{qf}E_D + E_0^2}{2E_{qf}E_0}, \tag{3.2}$$

The range of possible phase shifts ϕ is defined by the sign of the imaginary and of the real part of the space-charge field E_{sc}. Taking into account the negative sign of the electro-optic effect ($\Delta n = -1/2n^3rE$) the phase shift between the refractive index grating and light fringes lies within the range $0 < |\phi| \leq \frac{\pi}{2}$. Positive and negative values of ϕ correspond to dominant electron and hole charge transport respectively. Without
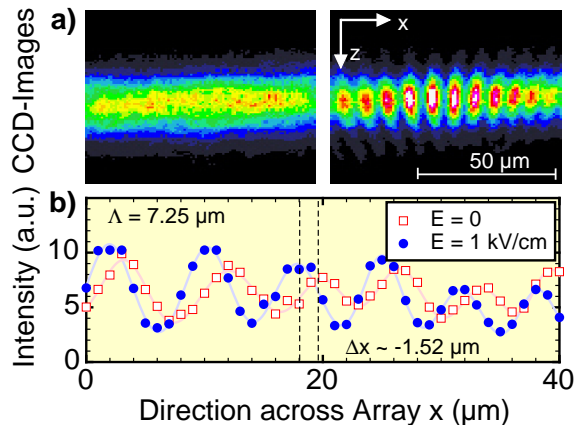

FIGURE 3.3: a) Output of a 15 mm long pure $Sn_2P_2S_6$ crystal without (left) and with (right) the induced photorefractive waveguides. b) Measured profiles along the x-direction without an external applied electric field (red open squares) and with an applied electric field of 1kV/cm (blue solid circles). The lines are drawn for the guidance to the eyes.

applied electric field, a maximum shift of $\phi_0 = \pm\frac{\pi}{2}$ is reached. It converges to zero when increasing the applied electric field.

After applying the electric field in our experiment, we get a spatial shift of the array in the negative x direction. This implies a reduced negative phase shift which approves that the hole mobility in our $Sn_2P_2S_6$ crystal is larger than the electron mobility, in agreement with two-wave mixing experiments at this wavelength [55]. For an applied electric field of $E_0 = 1$ kV/cm the phase shift calculated with (3.2) is $\phi_E = -0.25$ rad. This corresponds to a shift of the array by $\Delta x = -(\phi_E - \phi_0) \cdot \frac{\Lambda}{2\pi} = -0.21 \Lambda$, which is in perfect agreement with the measured value determined by comparing the two profiles shown in Fig. 3.3b).

By applying a modulating electric field, it may be possible to modulate such arrays in real-time. The arrays may also be shifted by a modulated phase-difference between the two writing beams, which can be realized with an additional electro-optic modulator or a piezo-controlled mirror in the path of one of the writing beams, as used for moving photorefractive gratings [33].

3.4   Conclusions

We have demonstrated for the first time to our knowledge waveguides and waveguide arrays induced by band-to-band excitation at visible wavelengths. In the electro-optic material $Sn_2P_2S_6$ we measured the fastest build-up of light induced waveguide structures ($\tau = 200$ μs at $I = 0.1$ W/cm^2) reported up to now. This is more than four orders of magnitude faster than for previously studied waveguides induced at visible wavelengths, which were produced by the conventional potorefractive effect [73]. The presented technique allows the generation of different straight and bent dynamic waveguide structures by using external masks or a spatial light modulator. Due to the fast response of $Sn_2P_2S_6$, these structures can be reconfigured in a sub-millisecond time-scale.

Chapter 4

High speed photorefraction at telecommunication wavelength 1.55 μm in Sn$_2$P$_2$S$_6$:Te [†]

We demonstrated for the first time photorefractive two-wave mixing in a bulk ferroelectric crystal using cw light at the telecommunication wavelength 1.55 μm. In the Te-doped ferroelectric semiconductor Sn$_2$P$_2$S$_6$ with absorption constant < 0.1 cm^{-1} at 1.55 μm, grating recording times of 10 ms and a two-beam coupling gain of 2.8 cm^{-1} have been measured at 350 mW power (intensity 440 W/cm^2) without a necessity to apply an external electric field. Using a moving grating technique a maximal gain of 6.0 cm^{-1} has been obtained.

4.1 Introduction

At the telecommunications wavelength 1.55 μm several photorefractive applications such as beam-cleanup, optical phase conjugation, signal processing or spatial soliton formation have been suggested [77]. So far photorefractive sensitivity at this wavelength has been observed in semiconductors [78, 79] and in photorefractive polymers [80]. In these material classes very high external fields are needed and in the operating range the material absorption is in the order of the observed photorefractive gain. In conventional photorefractive ferroelectrics the effect can be observed at 1.55 μm only under special conditions; e.g. in waveguides as in SBN (solitons) [81] and KNbO$_3$ (two-wave mixing) [82], where the absorption is increased by the defects induced by ion implantation, or with ultrashort lasers in the fs regime [83, 84], where a nonlinear two- or three-photon absorption process is used.

A very promising material for photorefraction in the IR is the ferroelectric semiconductor Sn$_2$P$_2$S$_6$ with high electro-optic coefficient, r_{111} is 160 pm/V at 1.5 μm [49]. It

---

is a relatively new photorefractive material with a smaller band-gap (2.3 eV) compared to conventional wide-band-gap oxide ferroelectrics [22]. It has a high gain factor of up to 40 cm^{-1} at visible wavelengths, is sensitive at $\lambda = 1.06~\mu$m [23, 25] and has a very fast response time in the near infrared at moderate light intensities of about 1 W/cm^2 (10 to 100 ms). Recent results showed that by doping with Te-atoms the photorefractive sensitivity can be increased considerably in the near infrared region [30] and phase conjugation could be demonstrated at $\lambda = 1.06~\mu$m [32]. In this letter we present the first results of two-beam coupling experiments at $\lambda = 1.55~\mu$m in Te-doped $\text{Sn}_2\text{P}_2\text{S}_6$ crystal using cw laser light. To the best of our knowledge this is the first time photorefraction has been observed in a ferroelectric bulk crystal at this wavelength.

4.2   Sample and measurement Setup

In our experiments a single mode, single frequency 1.55 μm fiber laser (NP Photonics) was used, which had a maximum power output of 400 mW. The beam was split into the pump and the signal beam with a glass plate, yielding an intensity ratio of 1:100 between the two beams. In front of the z-cut crystal a cylindric lens was used to focus the two beams onto the crystal in the vertical y direction in order to increase the intensity; the spot area was $\pi(w_{0y} \times w_{0x}) = \pi(50\,\mu\text{m} \times 450\,\mu\text{m})$. The light beams were p-polarized and incident on the crystal surface in the xz crystal plane symmetrically with respect to the z-axis. The power of the signal beam was measured with a Ge photodiode after the crystal.

The $\text{Sn}_2\text{P}_2\text{S}_6$ crystal studied in this work was grown using the conventional vapor transport technique using 1% Te in the initial compound [22,30]. The sample proportions were 4.5 mm $\times$ 6.0 mm $\times$ 2.1 mm along the x, y and z axis. We measured the absorption constant α at $\lambda = 1.55~\mu$m by transmission experiments with the laser, allowing to give an upper limit of $\alpha < 0.1$ cm^{-1}.

4.3   Experimental results

After switching on the pump beams, the two-wave mixing gain starts to increase exponentially, until it reaches the maximum value Γ. Fig. 4.1 shows the intensity dependence of this maximal two-wave mixing gain Γ. It has been shown that although several impurity levels contribute to the photorefractive effect in $\text{Sn}_2\text{P}_2\text{S}_6$, the assumption of only one dominant impurity level describes well the measured gain at a certain wavelength [22,30]. By doing so the intensity dependence can be explained by the competition between the photoconductivity σ_{photo} and the dark conductivity σ_{dark} as

$$\Gamma = \frac{\Gamma_0}{1 + I_{dark}/I}, \tag{4.1}$$

where I_{dark} (in our case 120 W/cm^2) is the light intensity at which the photoconductivity equals the dark conductivity and I is the total intensity, which is in our case defined as an average intensity of the focused beam. The maximum gain Γ_0 in the above equation depends on the grating spacing as [7]

$$\Gamma_0 = \frac{2\pi r_{eff} n^3}{\lambda} \frac{k_B T}{e} \frac{\cos(2\theta)}{\cos(\theta)} \frac{2\pi}{\Lambda \left(1 + \left(\frac{2\pi l_s}{\Lambda}\right)^2\right)}, \tag{4.2}$$

where n is the refractive index at the wavelength λ, θ is the angle between the signal beam and the sample normal, r_{eff} is the effective electro-optic coefficient, e is the fundamental electron charge, k_B is the Stefan-Boltzmann constant, T is the temperature and $l_s = [\epsilon\epsilon_0 k_B T/(e^2 N_{eff})]^{1/2}$ is the screening length, where ϵ is the dielectric constant, ϵ_0 is the vacuum permeability and N_{eff} is the effective trap density.
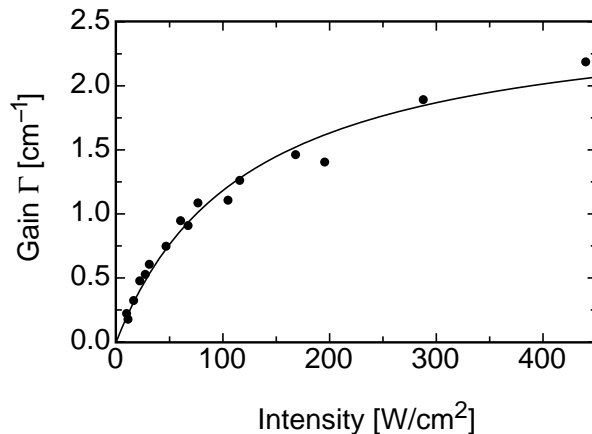

FIGURE 4.1: Intensity dependence of the maximal measured two-wave mixing gain Γ in Sn$_2$P$_2$S$_6$:Te at $\lambda = 1.55$ μm and grating spacing $\Lambda = 3.5$ μm. The solid curve is according to Eq. (4.1) for $\Gamma_0 = 2.6$ cm^{-1} and $I_{dark} = 120$ W/cm^2.

Note that our experiments were performed at a maximal average intensity of 440 W/cm^2 (350 mW power). This intensity was by a small margin still not high enough to reach the saturation gain factor Γ_0. We took this into account in the evaluation of the measured gain as a function of the grating spacing that is shown in Fig. 4.2. The maximum value is $\Gamma_{0,max} = 2.8$ cm^{-1} at $\Lambda = 2.0$ μm. This results in the density of effective traps $N_{eff} = 0.32 \cdot 10^{16}$ cm^{-3} and the effective electro-optic coefficient $r_{eff} = 78$ pm/V. Compared to the values obtained at shorter wavelengths, r_{eff} has a similar value, while N_{eff} is smaller (at 1.06 μm $N_{eff} = 0.53 \times 10^{16}$ cm^{-1}) and thus wavelength dependent in accordance with the trend observed previously in the 633 - 1064 nm wavelength range [30].

Fig. 4.3 shows the grating spacing dependence of the rise time τ at $\lambda = 1.55$ μm. This dependence is again modeled by assuming one dominant energy level [7]:
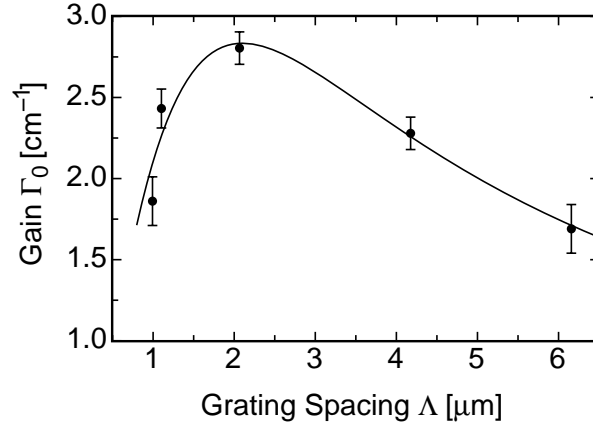
FIGURE 4.2: Grating spacing dependence of the maximal two-wave mixing gain Γ_0 at the wavelength $\lambda = 1.55$ μm. The solid line is according to Eq. (4.2) for $N_{eff} = 0.32 \cdot 10^{16}$ cm^{-3} and $r_{eff} = 78$ pm/V.

$$\tau = \frac{\epsilon\epsilon_0}{\sigma_{dark} + \sigma} \left(\frac{1 + \left(\frac{2\pi l_d}{\Lambda}\right)^2}{1 + \left(\frac{2\pi l_s}{\Lambda}\right)^2} \right), \tag{4.3}$$

where l_d is the diffusion length [22]. For large grating spacings the second term in this product converges towards one and can be neglected. This can be used to determine the dark conductivity σ_{dark} and photoconductivity σ_{photo}. At an intensity of $I_{max} = 440$ W/cm^2, σ_{dark} is $4.6 \cdot 10^{-8}$ 1/Ωm and σ_{photo} is $1.7 \cdot 10^{-7}$ 1/Ωm. Therefore at this intensity the photoconductivity is about 3.7 times the dark conductivity, which agrees very well with the measurement of the intensity dependence of the gain (Fig. 4.1, $I_{max}/I_{dark} = (440\,\text{W/cm}^2)/(120\,\text{W/cm}^2) \approx 3.7$).
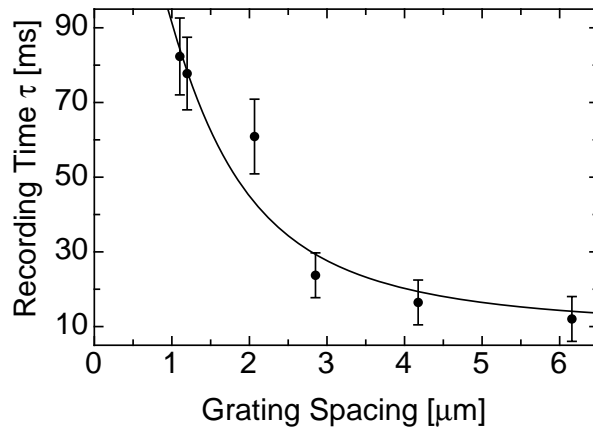

FIGURE 4.3: The recording-time τ as a function of the grating spacing Λ. The solid line is according to Eq. (4.3) resulting in $l_d = 0.8$ μm, $I_s = 0.2$ μm and $\sigma_{dark} + \sigma_{photo} = 2 \cdot 10^{-7}$ 1/Ωm. (I = 440 W/cm^2, $\lambda = 1.55$ μm)

For measurements performed on a larger time scale, i.e. several seconds, the two-wave mixing signal started to decrease due to charge compensation, which is a known phenomenon observed in some of the $Sn_2P_2S_6$ crystals [22, 24]. In our case the response time of the slow carriers was four orders of magnitude slower than the response time of the fast carriers at 440 W/cm^2. The origin of this compensation that was observed only in some of the crystals and depends on the crystal history like poling condition and preillumination is presently not clear [22]. The compesating carriers are thermally induced so this effect can be avoided by cooling the crystal [24]. We applied the moving grating technique similar as in Ref. [85]. One of the mirrors was fixed to a piezo motor. After the steady-state was reached, we shifted the grating produced by faster carriers by π and use both charge carriers for the grating formation process and thus reached a maximum transient gain $\Gamma_{0,max}$ of 6.0 cm^{-1} at $\Lambda = 1.6$ μm.

4.4 Discussion and comparison with semiconductors

Two-wave mixing has first been demonstrated at 1.5 μm in the semiconductor CdTe:V [78]. In this material a maximum gain of 7 cm^{-1} could be achieved by applying a large DC electric field of 14 kV/cm [86]. In a similar material CdZnTe:V a gain coefficient of 5.5 cm^{-1} has been reached by applying a large field and using additional stimulating illumination at $\lambda = 1.3$ μm [87]. Table 4.1 shows a comparison of photorefractive properties for different materials operating in a cw regime at 1.5 μm. With $Sn_2P_2S_6$:Te we can achieve the same or higher amplification factor $\Gamma_0 - \alpha$ without applying any external field. The advantage of semiconductors compared to $Sn_2P_2S_6$:Te is the low intensity, which is necessary to achieve two-wave mixing. We aim to realize low power operation by using waveguides that have been recently demonstrated in nominally pure $Sn_2P_2S_6$ crystals [88]. A disadvantage of semiconductors is the high electrical field, which has to be applied, and a need of a second laser source for the stimulating illumination. Another advantage of $Sn_2P_2S_6$:Te is the small absorption constant at 1.5 μm, which is below 0.1 cm^{-1} as compared to 0.5 to 2 cm^{-1} for CdTe with different dopants. Taking all this into account $Sn_2P_2S_6$:Te is a very attractive new material for applications at $\lambda = 1.5$ μm.

4.5 Conclusion

To summarize, we have demonstrated for the first time photorefractive two-beam coupling energy transfer with net gain at a telecommunication wavelength of 1.55 μm in a bulk ferroelectric crystal using cw laser light. The gain measured in the high electro-optic material $Sn_2P_2S_6$:Te without any enhancement methods was 2.8 cm^{-1} and by applying the moving grating technique a maximum gain of 6.0 cm^{-1} could be achieved with a fast rise time of 10 ms at 440 W/cm^2. These values could be improved further by controlling the temperature in order to suppress the slow charge carriers, by applying external electric

Table 4.1: Comparison of materials for photorefractive applications at 1.5 μm. I: total intensity, α: absorption constant, E_0: applied external field, r: electro-optic coefficient, Γ_0: maximum gain, τ: recording time.

	$Sn_2P_2S_6$:Te bulk	$KNbO_3$ waveguide	CdTe:V bulk	GaAs bulk
I [mW/cm^2]	$4 \cdot 10^5$	$2 \cdot 10^5$	10	$\sim$5
α [cm^{-1}]	< 0.1	0.5	2	0.1
E_0 [kV/cm]	0	0	14 (AC)	0
r [pm/V]	160	64	5.1	1.5
Γ_0 [cm^{-1}]	6.0	0.9	7	0.1
τ [ms]	10	100	-	-
$\Gamma_0 - \alpha$ [cm^{-1}]	6.0	0.4	5.0	0
Ref.	this work	[82]	[86]	[89]

fields and by using waveguides.

Chapter 5

Photorefractive waveguides in He$^+$-ion implanted pure and Te-doped Sn$_2$P$_2$S$_6$ †

We have demonstrated for the first time photorefractive two-wave mixing in He$^+$ implanted waveguides in one of the most promising materials for infrared photorefractive applications, the ferroelectric semiconductor Sn$_2$P$_2$S$_6$. The high optical nonlinearity is preserved after implantation and at the telecommunication wavelength $\lambda = 1.55$ μm, a maximal two-wave mixing gain of 2.5 cm^{-1} has been measured in Te-doped waveguides. In the nominally pure material an increase of the effective number of traps after implantation has been observed, resulting in an increase of the two-beam coupling gain by a factor of almost two in the 633-1064 nm spectral range. In 1% Te-doped Sn$_2$P$_2$S$_6$ the effect of ion implantation to the photorefractive response is completely different than in pure materials. While the dominant contribution by holes is not considerably affected, a strong, thermally induced charge compensation is observed in the He$^+$ implanted Te-doped waveguides.

5.1   Introduction

Photorefractive materials are interesting for a variety of applications, for example laser beam cleanup, optical phase conjugation, signal processing or spatial soliton formation [77]. Many of these applications require a response in the near infrared wavelength region, where very few materials fulfill most of the materials requirements. Semiconductors are for example sensitive in this range but they usually need high external fields or should operate close to resonance conditions to reach the desired nonlinearity [78, 79]. Many conventional photorefractive materials such as the ferroelectric oxides LiNbO$_3$ or KNbO$_3$ are very sensitive at shorter wavelengths, but do not show a high photosensitivity in the

---

†This chapter is accepted for publication in J. Opt. Soc. Am. B (2009)

infrared region. One way of solving this is doping the pure material, which led to some promising results mostly with BaTiO$_3$ and also KNbO$_3$ [90–92]. Another successful, but less investigated approach may be ion implantation of samples, thus creating a waveguide and additionally introducing new trap levels through deposition of energy in the process [93]. This method allowed for a photorefractive sensitivity at $\lambda = 1.55$ μm in Fe-doped KNbO$_3$ [82].

Tin thiohypodiphosphate (Sn$_2$P$_2$S$_6$) is a ferroelectric semiconductor with a high electro-optic coefficient ($r_{111} = 170$ pm/V at $\lambda = 633$ nm) and a narrower bandgap (2.3 eV) compared to conventional photorefractive oxides [49]. It has a wide transparency range from 530 nm up to 8 μm, making it very attractive for applications at infrared wavelengths. A very fast photorefractive response (10 - 100 ms) in the near IR at moderate light intensities of about 1 W/cm^2 can be achieved [22,30]. Recently, photorefractive sensitivity has been demonstrated at the telecommunications wavelength $\lambda = 1.55$ μm ($\Gamma = 2.8$ cm^{-1}) in the bulk material without an electric field applied, but high light intensities in the order of 100 W/cm^2 have been required. This is due to the relatively large dark conductivity in this material so that the low absorption makes high intensities necessary to induce a photoconductivity significantly higher than the dark conductivity [33]. Recently ion implanted waveguides have been demonstrated in pure Sn$_2$P$_2$S$_6$ material with losses of about 10 dB/cm [88]. These waveguides are very interesting for integrated optical application, such as Mach-Zehnder interferometers or for phase-matched frequency conversion [42], but may be also interesting for photorefractive applications, particularly at telecommunications wavelengths, to reduce power requirements for the wave-mixing applications [33].

In this work we investigate the photorefractive properties of the ion implanted planar waveguides in pure Sn$_2$P$_2$S$_6$ crystals and in Te-doped Sn$_2$P$_2$S$_6$ crystals implanted along different crystallographic directions. We show that ion implantation does not affect the high optical nonlinearity of this crystal but considerably influences the concentration of traps in Sn$_2$P$_2$S$_6$, however in a different way in pure and doped crystals.

5.2 Experimental

5.2.1 Samples and ion implantation

Pure Sn$_2$P$_2$S$_6$

Although the excellent performance of Sn$_2$P$_2$S$_6$ makes it interesting for many applications, only little is known about the origins of the photorefractive response, considering both, charge transport and energy (trap) levels involved [22, 27]. Nominally pure (yellow) Sn$_2$P$_2$S$_6$ crystals have been divided into two groups depending on their performance [22]. Type I crystals show a strong charge competition and can be influenced by pre-illumination [25]. This charge competition was used for example to demonstrate a

coherent optical oscillator with periodic zero-π phase modulation [28] or the photore-fractive slowing down of light [29]. Type II crystals do not show a pronounced charge compensation and are preferable for applications requiring high steady-state gain.

The pure Type II $Sn_2P_2S_6$ crystal studied in this work was grown using the conventional vapor transport method [22]. The sample proportions were 4.88 mm x 2.92 mm x 1.8 mm, along the x, y and z axis respectively, where the Cartesian axes x, y, z are defined as in [22]. The crystal was then irradiated in a TANDEM accelerator at ETH Zurich on the polished z-face by 2 MeV He$^+$ ions at a fluence of 0.25 x 10^{15} cm^{-2}. The implantation process was performed at room temperature with the ion current density being kept to extremely low values to prevent excessive heating of the crystals during the process. After implantation the sample was poled; during this process it was heated to 100 °C and kept at this temperature for several hours for annealing purpose. Annealing is usually used for ion implanted samples to restore the eventual decreased electro-optic coefficient in the guiding region due to ion-induced crystalline damage [93]. Using the barrier coupling method [94] and by approximating our refractive index profile by a step-index profile we determined a waveguide thickness of 6.0 ± 0.1 μm, which matches very well with SRIM simulations [www.srim.org]. This approach is much simpler than the model presented in [88] considering a more accurate index profile, but can describe our results with sufficient precision. Furthermore, from these measurement we obtained the change of the refractive index $\Delta n = 0.08 \pm 0.01$ in the barrier region, which is in good agreement with the parameters obtained from implantation experiments at higher fluences [88].

Te-doped $Sn_2P_2S_6$

The crystal was grown using conventional vapor transport technique with 1% Te in the initial compound. The sample proportions were 4.85 mm x 2.3 mm x 4.55 mm along the x, y and z axes respectively. The ion implantation was done the same way as for the pure $Sn_2P_2S_6$, except for the fluence that was higher, 0.6 x 10^{15} cm^{-2}, and the implantation direction, in this case the y-surface was irradiated. This implantation direction in $Sn_2P_2S_6$ has previously not been examined yet. Note that this configuration makes the end-face polishing process more challenging, because the cleavage plane is perpendicular to the y axis. Fig. 5.1 shows the results of the barrier coupling measurement. Whenever the reflectivity as a function of the angle drops, a mode was coupled into the crystal. The inset shows the corresponding measured and theoretical mode indices, used to determine the thickness of the waveguide and the barrier refractive index change. The line is just a guide to the eye, connecting the resulting mode points. The thickness of the waveguide calculated from this measurement was 5.52 ± 0.05 μm and the barrier had a refractive index change of $\Delta n = 0.09 \pm 0.01$. The Te-doped sample was investigated both before and after the annealing following the implantation.
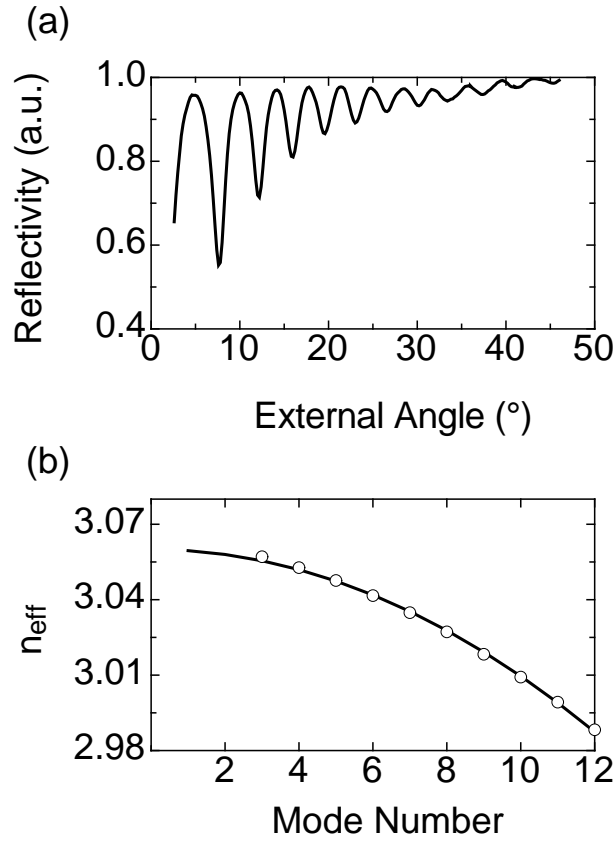
FIGURE 5.1: (a) The measured reflectivity using the barrier coupling method [94] as a function of the angle for the Te-Sn$_2$P$_2$S$_6$ waveguide implanted with He$^+$-ions with ion energy 2 MeV and fluence 0.6×10^{15} cm^{-2}. (b) The corresponding effective indices for the measured (dots) and calculated (solid line) profiles. The calculated modes of the best-fit profiles have been connected for clarity and are shown by the solid line. The resulting thickness is 5.52 ± 0.05 μm and the barrier strength $\Delta n = 0.09 \pm 0.01$.

5.2.2   Two-wave mixing measurement Set-up

For the two-wave mixing experiments a HeNe laser at 633 nm ($P_{\max} = 10$ mW), single-mode laser diodes at 780 nm ($P_{\max} = 100$ mW, Rainbow Photonics), a Nd:YAG laser at 1064 nm ($P_{\max} = 400$ mW, Lightwave Electronics) and a single-frequency fiber laser at 1550 nm ($P_{\max} = 400$ mW, NP Photonics) were used. The beam was split into the signal and the pump beam using a glass plate, resulting in a ratio of 1:100 between the two beams. The two beams were then coupled into the waveguide using a cylindrical lens with focal length of 19 mm to focus the beam in the vertical direction resulting in a spot area of $\pi(w_{0z} \times w_{0x}) = \pi(4\,\mu\text{m} \times 500\,\mu\text{m})$ at $\lambda = 633$ nm, with similar dimensions being used at the other wavelengths. The maximum power of the respective lasers was used to obtain the highest possible intensity and for the measurement in the bulk crystal the beams were focussed as well in order to be in a similar intensity regime. After the crystal the output plane of the crystal for the signal beam was visualized with a second spherical lens with focal length of 25 mm and imaged onto a CCD camera or a photodiode.

For the pure $Sn_2P_2S_6$ sample the beams were incident on the xz crystal surface, that is parallel to the mirror symmetry plane of the crystal with the point group symmetry m. Because of this the polarization of the beams was adjusted with respect to the rotation of the indicatrix at the respective wavelength in order to have an eigenmode propagating in the waveguide [88]. The beams were incident in the xy plane symmetrically with respect to the y axis so that the grating vector was parallel to the x axis. This means that the electro-optic coefficient used in the experiment was not the one usually employed in this material ($r_{111} = 170$ pm/V at $\lambda = 633$ nm) but a combination of r_{111}, r_{131} and r_{331} resulting in a coefficient $r = 180$ pm/V at $\lambda = 633$ nm for light polarized along the x_3 main axis of the Fresnel ellipsoid and the electric field along the x axis of the chosen Cartesian system [49].

Due to the different orientation of the Te-doped $Sn_2P_2S_6$ sample during implantation the usually employed electro-optic coefficient r_{111} could be used. Thus the beams entered the crystal through the xy surface and were polarized along the x-axis.

5.3   Results and Discussion

5.3.1   Pure $Sn_2P_2S_6$

For the evaluation of the amplification data we used the usual plane-wave approximation. If we use the model taking into account the Gaussian beam shape and strongly varying intensities in the focussed area [95] the photorefractive gain constant increases by about 10% with respect to the value reported, which is within the error range and therefore neglected. The whole length of the crystal was used as the interaction length for the calculation of the two-beam coupling gain.

We first measured the photorefractive gain Γ as a function of intensity to make sure,

that we are in the saturated region and the dark conductivity does not decrease the measured gain [33]. The input angle θ of the beams onto the crystal was varied to measure the gain as a function of the grating spacing $\Lambda = \lambda/(2\sin\theta)$, where λ is the vacuum light wavelength. The two-beam coupling gain coefficient can be described in the diffusion case and within the weak probe beam approximation as follows [7]:

$$\Gamma_0 = \frac{2\pi r_{\text{eff}} n^3}{\lambda} \frac{k_B T}{e} \frac{\cos(2\theta')}{\cos(\theta')} \frac{2\pi}{\Lambda \left(1 + \left(\frac{2\pi l_s}{\Lambda}\right)^2\right)}, \tag{5.1}$$

where n is the refractive index at the wavelength λ, θ' is the internal angle between the signal beam and the sample normal, r_{eff} is the effective electro-optic coefficient, e is the electron charge, k_B is the Boltzmann constant, T is the temperature and $l_s = [\epsilon\epsilon_0 k_B T/(e^2 N_{\text{eff}})]^{1/2}$ is the screening length, where ϵ is the dielectric constant, ϵ_0 is the vacuum permeability, N_{eff} is the effective trap density and r_{eff} the effective electro-optic coefficient.

Fig. 5.2(a) shows the grating spacing dependence of the two-wave mixing gain coefficient Γ in the nominally pure Sn$_2$P$_2$S$_6$ bulk crystal. The measurement was done by using the same set-up as for coupling into the waveguide. The direction of the amplification with respect to the polarization of the crystal allows to determine that holes are the dominant charge carriers, as is expected [22]. The resulting maximal gain coefficients were 3.5, 1.8 and 0.61 cm^{-1} at the wavelengths 633, 780 and 1064 nm, respectively. The solid curves were obtained using Eq. (5.1) with the following data: effective dielectric constant $\epsilon_{\text{eff}} = 230$ and the refractive indices $n_1 = 3.02$ at 633 nm, 2.91 at 780 nm and 2.82 at 1064 nm [22]. With these parameters we obtained values for the effective electro-optic coefficient r_{eff} and the effective concentration of traps N_{eff}; these are listed in Table 5.1.
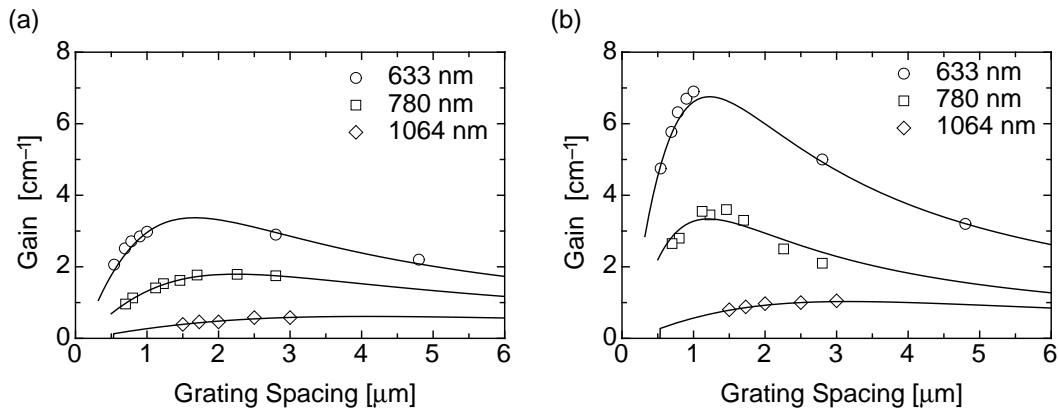

FIGURE 5.2: The two-wave mixing gain Γ as a function of the grating spacing Λ in nominally pure Sn$_2$P$_2$S$_6$: (a) in the bulk crystal, (b) in the waveguide. The solid curves are according to Eq. 5.1 and the resulting parameters are listed in Table 5.1.

Fig. 5.2(b) shows the grating spacing dependence of the two-wave mixing gain coefficient Γ in the waveguide in the same pure Sn$_2$P$_2$S$_6$ crystal. The resulting maximal

two-wave mixing gain coefficients are 6.8, 3.3 and 1.0 cm^{-1} at the wavelengths 633, 780 and 1064 nm respectively. The results of the analysis with Eq. (5.1) are shown in Table 5.1. The effective concentration of traps N_{eff} has increased in the waveguide region. This is attributed to the ions deposing a small amount of their implantation energy in the guiding region and thus introducing new defects.

In photorefractive measurements, one has to consider an effective electro-optic coefficient $r_{eff} = r'_{eff}\xi$, where r'_{eff} is a combination of the strain-free electro-optic contribution and the elasto-optic contribution. ξ is a reduction factor, which lowers the apparent effective electro-optic coefficient r'_{eff}, due to, e.g. electron-hole competition, different from the charge compensation observed at longer time scales. This reducing factor is responsible for the discrepancy of r_{eff} in Table 5.1 and the value obtained through direct interferometric measurements. The effective electro-optic coefficient does not change in the waveguiding region compared to the bulk within the error margins, which is an important result considering the reduction of the nonlinear-optic properties in several materials after waveguide formation [93].

The temporal evolution of the build-up can be described by a single exponential function with the time constant τ:

$$\Gamma = \Gamma_0(1 - \exp(-t/\tau)) \tag{5.2}$$

The time constants τ are shown in Table 5.1. The direct comparison of the time constants obtained in the bulk crystal and in the waveguide region is difficult since the exact coupling efficiency and thus the resulting intensity are cannot be determined with high precision. Due to the strong confinement and thus high intensity of the beam one would expect faster time constants in the waveguide region, which is confirmed by the measurements. At time scales of several minutes no decrease of the gain could be observed, neither in the waveguide region nor in the bulk region of the crystal. The amplification was in direction of the $+x$ crystalline axis, implying that holes are the dominant charge carriers in both regions of the crystal, as usually in $Sn_2P_2S_6$ crystals [22].

5.3.2 Te doped $Sn_2P_2S_6$

As for pure $Sn_2P_2S_6$ the grating spacing dependence of the peak gain coefficient was measured and the effective number of traps N_{eff} and the effective electro-optic coefficient r_{eff} determined according to Eq. 5.1. The respective values are listed in Table 5.1. N_{eff} is almost the same for the bulk and the waveguiding region, which is different than in the case of undoped $Sn_2P_2S_6$, where the implantation increases its value. In Te-doped $Sn_2P_2S_6$ the trap levels created through implantation do not interfere with the main trapping channel. This might indicate that the concentration of these traps has already reached the saturation in our sample (1% Te in the initial compound). Something similar is observed if the Te concentration in the initial compound is increased to 2-3%. In this case the photorefractive gain remains about the same as well [30].

TABLE 5.1: Photorefractive parameters of ion implanted Sn$_2$P$_2$S$_6$. (Error: 15%)

	λ (nm)		Γ_{max} cm^{-1}	τ (ms)	r_{eff} (pm/V)	N_{eff} (10^{16} cm^{-3})
Nominally pure	633	wg	6.8	2	36	0.89
(yellow)		bulk	3.5	7	25	0.45
	780	wg	3.3	8	25	0.94
		bulk	1.8	14	24	0.26
	1064	wg	1.0	38	30	0.13
		bulk	0.6	64	23	0.078
SPS:Te 1%	633	wg	7.5	3	36	1.1
		bulk	6.4	4	33	0.9
	780	wg	5.8	8	46	0.81
		bulk	5.2	11	45	0.61
	1064	wg	5	20	76	0.49
		bulk	4.1	23	61	0.51
	1550	wg	2.5	85	74	0.31
		bulk	2.6	75	72	0.34

The direction of the amplification again implies holes as being the dominant charge carriers. In the bulk crystal no charge compensation was observed, which can be seen in Fig. 5.3. We measured the amplified signal beam on longer time scales, in the order of several minutes, and could not observe any compensating effect except at $\lambda = 1.55$ μm. At this wavelength a weak and very slow compensation effect with τ_s in the order of 400 s was observed, in good agreement with [33]. On the other hand in the waveguiding region a strong charge compensation could be observed at all the wavelengths, similar as observed in bulk Type I samples. Therefore we refer to the charge carriers responsible for the first increase of the signal beam as "fast charge carriers" and the ones responsible for the decrease as "slow charge carriers". Fig. 5.3 shows an example at $\lambda = 780$ nm. These slow charge carriers are one order of magnitude slower than those responsible for the formation of the first grating at room temperature, and thus essentially faster than for example the compensating effect observed in the bulk at $\lambda = 1.55$ μm, which showed compensation effects at a timescale of minutes. If the nature of the compensating charges is the same and only the concentration is increased by the implantation or if different levels are created is not clear. It is also interesting that the effect does not occur in nominally pure Type II Sn$_2$P$_2$S$_6$ samples. The creation of new types of charge carriers through ion implantation is known from KNbO$_3$. Here an even more pronounced effect was observed, since the direction of the amplification in the waveguiding region was opposite to the one in the bulk crystal the charge separation process was changed from p-type to n-type, which was attributed to the reduction of Fe impurities by proton irradiation [82]. The

ion implantation in $Sn_2P_2S_6$:Te gives us a method to create the compensating effect if wanted for applications such as the coherent optical oscillator with periodic zero-π phase modulation [28] or the photorefractive slowing down of light [29].
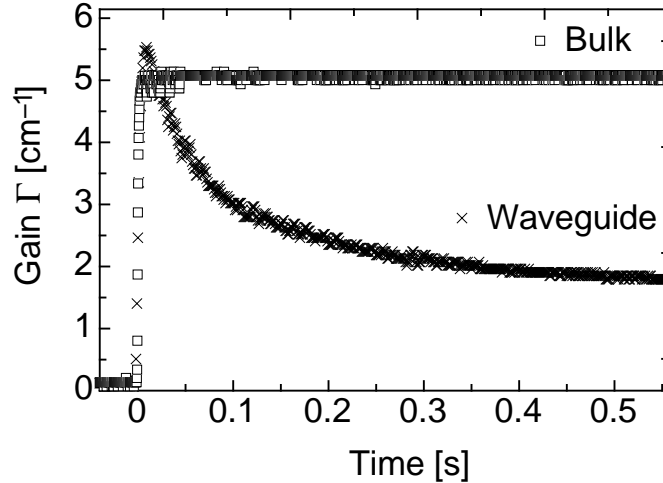

FIGURE 5.3: The two-beam coupling signal measured after opening the pump at $t = 0$ s in Te-doped $Sn_2P_2S_6$, with crosses representing the signal in the waveguiding region and squares the bulk region. It can be clearly seen, that only in the waveguiding region charge compensation occurs, with a time constant $\tau_{\text{wgs}} = 140$ ms. ($\lambda = 780$ nm, $\Lambda = 2.0$ μm)

To investigate the nature of this compensating effect we measured the temperature dependence of the build-up times of the fast and slow charge carriers, as it was previously observed, that the slow carriers in Type I $Sn_2P_2S_6$ crystals are rather temperature induced than by light excitation [22, 25]. Peltier elements were used to cool or heat the crystal and the two-beam coupling signal was measured.

The compensating charge carriers build-up time decreases exponentially with increasing temperature, while the fast charge carriers build-up time remains more or less constant. This is shown in Fig. 5.4. The exponential behavior of the slow charge carriers can be described by the following Arrhenius equation:

$$\tau_{\text{wgs}} = \tau_0 \exp\left(\frac{\Delta E}{k_b}\frac{1}{T}\right), \qquad (5.3)$$

where τ_{wgs} is the slow time constant, τ_0 is the normalization constant, T is the temperature in Kelvin and ΔE the characteristic activation energy for the thermal motion of the slow charge carriers. The activation energy ΔE corresponding best to the measurement performed at $\lambda = 780$ nm in the waveguide is 0.95 ± 0.02 eV for the slow charge carriers. This matches very well with the activation energy measured for the compensating charge carriers in bulk $Sn_2P_2S_6$:Te at $\lambda = 1.55$ μm, where ΔE is 0.96 ± 0.2 eV, indicating their common origin, although the response times differ by 3 orders of magnitude. Compared to normal bulk Type I $Sn_2P_2S_6$ crystals this energy is almost three times larger in the

Sn$_2$P$_2$S$_6$:Te He$^+$-ion implanted waveguide [25]. The origin could still be similar, since in doped samples we have additional levels in the gap and so complementary channels for excitation of charge carriers. At 40 °C the two gratings form at the same speed and by evaluating the magnitude of the gain contribution of the slow charge carriers even exceeds the one from the fast charge carriers.
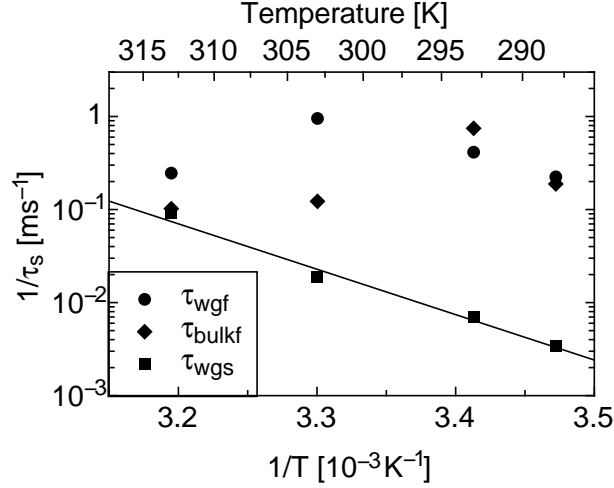

FIGURE 5.4: The temperature dependence of the inverse build-up time is shown on a logarithmic scale for Sn$_2$P$_2$S$_6$:Te at $\lambda = 780$ nm and $\Lambda = 2.0$ μm. τ_{bulkf} and τ_{wgf} are the build up times for the fast charge carriers in the bulk material respectively the waveguide and τ_{wgs} the one for the slow charge carriers in the waveguide. Only the slow charge carriers show a strong dependence on the temperature. The solid line is according to Eq. 5.3 and results in an activation energy $\Delta E = 0.95$ eV.

From the intensity dependence of the charge excitation rate it is possible to determine the dark conductivity σ_{dark} by using the following relation:

$$\frac{1}{\tau} = \frac{\sigma_{\text{photo}}(I) + \sigma_{\text{dark}}}{\epsilon_0 \epsilon}, \tag{5.4}$$

where $\sigma_{\text{photo}}(I)$ is the photoconductivity depending linearly on the intensity. In the bulk region σ_{dark} is 2.7×10^{-8} 1/Ωm and in the waveguide region σ_{dark} is 7.4×10^{-8} 1/Ωm at room temperature. This increased dark conductivity due to ion implantation increases the speed of the process but may reduce the two-wave mixing efficiency at low intensities, specifically strong at 1.55 μm, where it has been shown that extremely high intensities are necessary (400 W/cm^2) to induce a large enough photoconductivity to reach the saturated photorefractive gain region [33].

Of special interest are the photorefractive properties of Te-doped Sn$_2$P$_2$S$_6$ at $\lambda = 1.55$ μm. As mentioned to reach the saturated gain region a very high intensity of about 400 W/cm^2 is necessary [33], which is more easily achievable in a waveguide, especially for a longer interaction length if compared to a focussed beam. As can be seen in Table 5.1

the photorefractive properties in the waveguide region are about the same as in the bulk material, making it well suited for applications.

To investigate the effect of annealing, the sample was heated to a temperature of 100 °C for several hours and additionally repoled along the x-axis. Measurements of the two-beam coupling gain did not show any significant difference compared to before the annealing was done. The compensating effect of the slow charge carriers was still present and not influenced by the annealing.

5.4 Conclusion

We have measured for the first time the photorefractive properties of ion implanted waveguides in $Sn_2P_2S_6$. In the undoped crystal implanted along the z direction an increase of the effective number of traps N_{eff} was observed, resulting in a higher two-beam coupling gain Γ. At $\lambda = 633$ nm Γ increased from 3.5 cm^{-1} to 6.8 cm^{-1}. Neither in the bulk material nor in the waveguide region charge compensation could be observed. The high effective electro-optic coefficient r_{eff} is preserved by He$^+$ implantation.

In Te-doped $Sn_2P_2S_6$ for the first time the y face of the crystal was implanted allowing the use of r_{111} and TE waveguiding modes. No increase of N_{eff} could be observed in the waveguiding region compared to the bulk crystal, which may be attributed to the high trap concentration in doped samples as compared to the ones created by implantation. In the waveguiding region a strong charge compensation was observed, created by the ion implantation, since in the bulk crystal no such effect was observed. The nature of these ion-induced defects is presumably similar to those previously observed in Type I $Sn_2P_2S_6$ crystals. The temperature dependence of the build-up time of this compensation resulted in an activation energy of $\Delta E = 0.95 \pm 0.02$ eV, which is larger than previously observed in Type I $Sn_2P_2S_6$ crystals but may have a similar origin.

At $\lambda = 1.55$ μm in Te-doped $Sn_2P_2S_6$ a similar photorefractive response was observed as in the bulk material. This is especially interesting since at this wavelength a high intensity is needed to reach the saturated two-beam coupling region, making waveguides the ideal choice, even though a slightly higher dark conductivity in the waveguide was measured.

Acknowledgements

Appendix A

Determination of the absorption constant in the interband region by photocurrent measurements †

We determined high absorption constants of crystals from photocurrent measurements within the interband absorption region $(10 - 10^4\,\mathrm{cm}^{-1})$. The method has been demonstrated in the interband absorption regime near 530 nm in $\mathrm{Sn_2P_2S_6}$, a novel infrared sensitive photorefractive material, and in the interband absorption regime near 257 nm of near stoichiometric $\mathrm{LiTaO_3}$. Besides the verification of older measurements with our new technique, also precise absorption data for $\mathrm{Sn_2P_2S_6}$ in the wavelength range $488 - 514$ nm are presented.

A.1   Introduction

Light emitting diodes, photodetectors, electro-absorption modulators [96], solar cells and many other photonics devices involve transitions of charges between bands, and thus work in a region of high light absorption. Also holographic applications based on the interband photorefractive effect such as multiple quantum well devices [97,98], incoherent-to-coherent optical converters [57], light-induced waveguides [2], high-frame-rate joint Fourier-transform correlators [58] and dynamically reconfigurable wavelength filters [59], operate beyond the absorption edge with absorption constants up to 10^3 cm^{-1}. In this region the absorption constant is not easily measured, but is nevertheless of crucial importance for the underlying basic physical mechanisms and the applications.

The most common technique for measuring absorption constants in the order of $10 - 10^4\,\mathrm{cm}^{-1}$ is a direct measurement of the transmission of a thin sample. This method is quite precise but often requires a thin plate of only a few μm thickness.

---

†This chapter has been published in Appl. Phys. B **83**, 115-119 (2006) [63]

If the light at the wavelength of interest induces a secondary physical effect, it is possible to determine the absorption constant indirectly by a scanning method. For example, if the secondary effect is a light-induced absorption at another wavelength, we can determine the absorption constant by depth scanning of the transmitted intensity of the light at the second wavelength from the side of the crystal, while illuminating the crystal from the top with the wavelength of interest [56, 99]. A similar method is based on scanning the diffraction efficiency of holographic gratings at different depths instead of using the induced absorption [20]. The basic principle of the scanning method is applicable for the absorption measurement if the strength of the secondary physical effect is a monotonic function of the light intensity. These techniques can reach a precision of about 25 percent, but very sharp polished edges of the crystal are needed, since the measurement involves probing light traveling only a few micrometers below the crystal surface. If the secondary effect is light-induced absorption, we refer to this technique here as the induced absorption method.

In ferroelectrics, the absorption constant can also be determined by measuring the transient pyroelectric current due to changes in the ferroelectric polarization produced by heating the sample through the absorption of light [100]. This method, however, usually requires very precise electrometers, the prior knowledge of several material constants, and is very sensitive to external influences, so that it has to be done in a vacuum chamber.

A different approach for determining the absorption constant is based on the reflectivity measurements. Either one measures the wavelength dependence of the reflectivity at normal incidence and then evaluates the absorption using the Kramers-Kronig relation, or one measures the angular dependence of the reflectivity at a certain wavelength and evaluates the absorption constant using the Fresnel formulas [101, 102]. Both of these methods are only well suited for very high absorption constants in the order of $10^4 - 10^5 \, \mathrm{cm}^{-1}$ and they usually show limited accuracy.

In semiconductors photoconductivity measurement is a standard method to determine the absorption edge and the absorption constants in the transparent region [103]. Here we determine the absorption constant beyond the absorption edge by measuring the photocurrent in bulk crystals. Compared to the existing methods it does not require any special crystal preparation or the knowledge of other material constants.

We first present in section 2 a theoretical background of the proposed method. In section 3 we report the measurements of the photocurrent for $\mathrm{Sn_2P_2S_6}$ and the determination of the absorption constant at the wavelengths of $\lambda = 514 \, \mathrm{nm}$, $\lambda = 501 \, \mathrm{nm}$, $\lambda = 496 \, \mathrm{nm}$ and $\lambda = 488 \, \mathrm{nm}$ and compare the obtained values to the results of a direct transmission measurement using a thin plate of $45 \, \mu\mathrm{m}$ thickness. The absorption coefficients were also determined by this photocurrent method for near-stoichiometric $\mathrm{LiTaO_3}$ at $\lambda = 257 \, \mathrm{nm}$ and the results were compared to published data.

A.2 Theoretical

We consider a photoconducting dielectric crystal illuminated by light with photon energy larger than the band gap of the material. We are interested in the photocurrent generated by bandgap light with an applied electric field E, and on how this photocurrent depends on the absorption constant α if one of the sample surfaces is homogeneously illuminated. Fig. A.1a shows the orientation of the crystal and the coordinate system we use for our calculations and experiments with $Sn_2P_2S_6$ and Fig. A.1b shows the same for the experiments with $LiTaO_3$. In the case of $Sn_2P_2S_6$ the light is incident on the surface normal to the z-axis and the field is applied parallel to the x-axis of the crystal. For $LiTaO_3$ the light is incident on the surface normal to the x-axis and the field is applied parallel to the z-axis of the crystal.
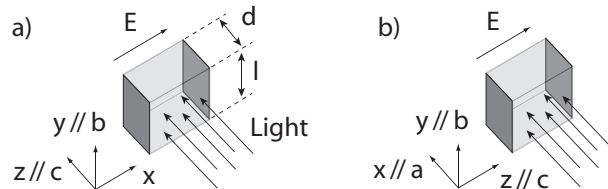

FIGURE A.1: Coordinate system used and orientation of the crystallographic axes a, b, c. Figure a) shows the coordinate system and orientation of the crystal axes for $Sn_2P_2S_6$, where the x-axis is shifted by $1.5°$ with respect to the crystallographic a-axis. Figure b) shows the coordinate system and the orientation of the crystallographic axes for $LiTaO_3$.

According to the theoretical analysis of charge transport induced by interband illumination in photoconductive crystals [20] we can distinguish two different regimes, which are identified by a specific characteristic exponent κ for the increase of the photoconductivity σ with light intensity I ($\sigma \propto I^\kappa$). For low light intensities I and considering only one deep impurity level (due to intrinsic defects or dopants) inside the band gap of the material, carriers recombine predominantly into the impurity level. The recombination rate does not depend on light intensity, which leads to a linear increase of the photoconductivity with light intensity, similarly to conventional off-resonant charge excitation [11]. For large light intensities I the interband regime becomes dominant, as was also confirmed experimentally in $KNbO_3$ [20] and $LiTaO_3$ [56]. In this regime charge carriers recombine from the valence to the conduction band and the recombination rate increases with intensity. As a result the steady-state free-hole concentration p_0 and the free-electron concentration n_0 follow the same square root intensity dependence $n_0 \cong p_0 \cong \sqrt{gI/\gamma_{dir}}$ [20], where γ_{dir} is the band-to-band recombination rate and g the photoexcitation constant. The photoexcitation is proportional to the absorption constant α as $g = \alpha/h\nu$, where h is the Planck constant, ν the frequency and α the absorption constant. The photoconductivity $\sigma(z)$ is then given by:

$$\sigma(z) = e(p_0\mu_h + n_0\mu_e) \propto e(\mu_h + \mu_e)\sqrt{\frac{\alpha I(z)}{\nu}} \propto \sqrt{\frac{\alpha}{\nu}}\, e^{-\frac{\alpha z}{2}}, \tag{A.1}$$

where e is the electron charge, μ_e the mobility of the electrons and μ_h the mobility of the holes and where we assumed an exponential decrease of intensity in the beam propagation direction z as $I(z) = I_0 e^{-\alpha z}$. The spatially integrated electric current J measured by an amperemeter in series with the crystal can now be calculated as:

$$J = \int_0^d j(z)l\,\mathrm{d}z = const\, E\sqrt{\frac{\alpha}{\nu}}\, l \int_0^d e^{-\frac{\alpha z}{2}}\,\mathrm{d}z, \tag{A.2}$$

where l is the length of the crystal in the y direction and d the thickness in the z direction, $j(z) = \sigma(z)E$ is the depth-dependent electric current density for a field applied parallel to the x direction and $const$ is a proportionality factor including intrinsic material constants. By solving the last integral and considering $d \gg 1/\alpha$ we get

$$J \propto \frac{1}{\sqrt{\alpha\nu}}, \tag{A.3}$$

which shows that the measured current is inversely proportional to the square root of the absorption constant α. This relationship is valid if the wavelength and intensity are such that the interband processes dominate, which means that the photoconductivity increases according to the square root of the intensity. In this case equation (A.3) can be used to determine the absorption constant by a comparative process provided that one absorption constant (at another wavelength or for a different polarization) has been determined directly by another method. The basic principle is schematically shown in Fig. A.2 for the case, where the absorption constant α_y is smaller than α_x, and where $\alpha_y^{\lambda_1}$ can be measured directly. Its wavelength (λ_1) is typically chosen close to the transparency range, where the absorption can be determined by standard methods with high precision. Then the photocurrents $J_x^{\lambda_1}$, $J_x^{\lambda_2}$, $J_y^{\lambda_1}$ and $J_y^{\lambda_2}$ for the same intensity $(J \propto \sqrt{I_0})$, for both wavelengths λ_1 and λ_2 and both polarizations (x and y) are measured. By using the following relationships, derived from (A.3),

$$\sqrt{\frac{\alpha_y^{\lambda_1}}{\alpha_x^{\lambda_1}}} = \frac{J_x^{\lambda_1}}{J_y^{\lambda_1}}, \tag{A.4}$$

$$\sqrt{\frac{\alpha_y^{\lambda_1}}{\alpha_x^{\lambda_2}}}\sqrt{\frac{\nu_1}{\nu_2}} = \frac{J_x^{\lambda_2}}{J_y^{\lambda_1}}, \tag{A.5}$$

$$\sqrt{\frac{\alpha_y^{\lambda_1}}{\alpha_y^{\lambda_2}}}\sqrt{\frac{\nu_1}{\nu_2}} = \frac{J_y^{\lambda_2}}{J_y^{\lambda_1}} \tag{A.6}$$

one can determine the absorption constants $\alpha_x^{\lambda_1}$, $\alpha_y^{\lambda_2}$ and $\alpha_x^{\lambda_2}$. In many cases these absorption constants are much too large to be determined directly by the classical methods

as $\alpha_y^{\lambda_1}$ in our example. Note that the factor $\sqrt{\nu_1/\nu_2}$ in (A.5) and (A.6) takes into account that light of the same intensity I_0 does not contain the same number of photons at different wavelengths. If the reflection losses differ considerably at different wavelengths or polarizations because of different refractive indices, one should consider it when normalizing the current to the input intensity ($J \propto \sqrt{I_0}$) considering $I_0 = (1-R)I_{ext}$, where $R = (n-1)^2/(n+1)^2$ is the reflectivity, n the refractive index and I_{ext} the external light intensity.
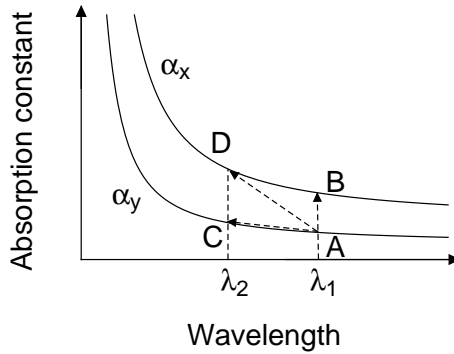

FIGURE A.2: A schematic absorption spectra showing the principle of our method. For point A the lower absorption constant $\alpha_y^{\lambda_1}$ can be determined by direct transmission measurements. By using equations (A.4)–(A.6) one can calculate the large absorption constants $\alpha_x^{\lambda_1}$, $\alpha_y^{\lambda_2}$, $\alpha_x^{\lambda_2}$ etc. (points B–D) by measuring the photocurrents at the corresponding wavelengths and polarizations.

A.3   Experimental verification

We verified the proposed method for two different materials, where band-to-band photorefraction [20] is a very efficient recording process. The first material we used was the narrow-bandgap ferroelectric crystal $Sn_2P_2S_6$. It has been demonstrated as a promising material for fast hologram recording in the infrared [25,61] and also interband photorefraction in the visible near 530 nm [62]. It has a transparency range extending from 0.53 μm to 8 μm and has been proposed as an interesting nonlinear optical material in this wide frequency range [47]. In $Sn_2P_2S_6$ crystal optical correlation at high repetition rates has been demonstrated [58] using interband recording at a wavelength of 532 nm using frequency doubled Nd:YAG laser. In the interband region the absorption constant has been previously calculated using the Urbach rule [104,105].

The second material is near-stoichiometric $LiTaO_3$ (SLT), which is attractive for several electro-optical, photorefractive or nonlinear optical applications like nonvolatile holographic data storage [106] or frequency doubling into the UV [107] and is transparent down to $\lambda \approx 280$ nm. In SLT deep UV fast interband photorefraction has recently been demonstrated [56]. The absorption constant in this regime has been measured with the

method of the induced absorption [56] and by direct measurements in samples of different compositions [108].

A.3.1 Determination of the absorption constant in $Sn_2P_2S_6$

We first determined the absorption constants in $Sn_2P_2S_6$ using the direct transmission method. We used a thin plate of $Sn_2P_2S_6$ with dimensions $7.3 \times 8.3 \times 0.045$ mm^3 along the x, y and z axes. In this work we use the standard coordinate system with the z-axis parallel to the crystallographic c-axis, $y \parallel b$ normal to the mirror plane, and x normal to y and z. The thin plate was attached to a substrate of quartz with a thickness of 3 mm. The crystal was poled along the x-axis. The absorption constant in the interband regime was measured by the direct transmission method at four Ar-ion laser lines ($\lambda_1 = 514$ nm, $\lambda_2 = 501$ nm, $\lambda_3 = 496$ nm, $\lambda_4 = 488$ nm). In all the experiments the contribution of the reflections between the substrate and the $Sn_2P_2S_6$ plate were taken into account as well as multiple Fresnel reflections in the crystal itself. We used the recently determined two-oscillator Sellmeier parameters for the refractive indices of $Sn_2P_2S_6$ [42]. The results of the transmission measurement with the laser lines are given in Table A.1 and Fig. A.3. The solid lines in Fig. A.3 are obtained with the Urbach extrapolation. This extrapolation uses the exponential behavior of the absorption constant at the absorption edge:

$$\alpha(\nu) = \alpha_0 \exp\left(\frac{h\nu - E_0}{w}\right), \tag{A.7}$$

where w is the energy width of the exponential absorption edge, and α_0 and E_0 empirical parameters. In the measurements reported in Ref. 105 it seems that the axes were defined differently, because the Urbach parameters given there would qualitatively match with our results if the polarizations x and y were exchanged. The difference in the absorption values obtained there might be related to a possible different crystal composition.

TABLE A.1: Absorption constants α_x and α_y of pure $Sn_2P_2S_6$ as obtained with a direct transmission measurement using an argon laser and a thin sample ($z = 45\,\mu$m) and as obtained from photocurrent measurements with a bulk crystal.

Wavelength	direct α_x [cm^{-1}]	photoc. α_x [cm^{-1}]	direct α_y [cm^{-1}]	photoc. α_y [cm^{-1}]
$\lambda_1 = 514$ nm	490 ± 20	380 ± 120	110 ± 10	starting point
$\lambda_2 = 501$ nm	1450 ± 50	1100 ± 450	500 ± 20	420 ± 130
$\lambda_3 = 496$ nm	1730 ± 65	1350 ± 530	860 ± 35	800 ± 280
$\lambda_4 = 488$ nm	–	2600 ± 800	1730 ± 70	2050 ± 850

The $Sn_2P_2S_6$ crystal used for the photocurrent measurements had the dimensions $5.07 \times 5.38 \times 4.85$ mm^3 along the x, y and z axes. It was poled along the x-axis and
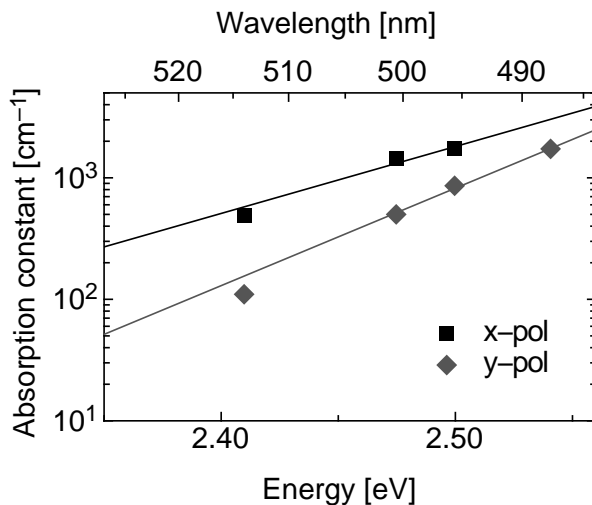
FIGURE A.3: Absorption constant of $Sn_2P_2S_6$ in the interband regime measured with a thin sample of 45 μm thickness. The solid lines are according to equation (A.7).

had silver electrodes painted onto the x-surfaces. We applied an electric field between 200 and 600 V/cm parallel to the x-axis, which is about 15 degrees off the spontaneous polarization [43]. The crystal surface normal to z of the sample was homogeneously illuminated with green ($\lambda_1 = 514$ nm, $\lambda_2 = 501$ nm) or blue ($\lambda_3 = 496$ nm, $\lambda_4 = 488$ nm) light polarized either parallel to the x- or y-axis of the crystal. We determined the photocurrent by measuring the voltage drop over a reference resistor of 125 kΩ put in series with the crystal. A multimeter with a large input impedance (1 GΩ) was used for the current measurement.

For increasing light intensity we expect the different ratios of J to approach a constant value corresponding to equations (A.4)–(A.6), because we approach the purely interband absorption regime. Fig. A.4 shows the intensity dependence of the ratio between the photocurrents $J_x^{\lambda_4}/J_y^{\lambda_4}$ of the x-polarization and the y-polarization at $\lambda_4 = 488$ nm. After reaching the intensity 10 mW/cm^2, the number of charge carriers in the band is sufficient for band to band recombination and the photocurrent follows the expected square root intensity dependence. In this regime the ratio $J_x^{\lambda_4}/J_y^{\lambda_4}$ is a constant and the ratio of the absorption constants $\alpha_y^{\lambda_4}/\alpha_x^{\lambda_4}$ can be determined. The results for λ_1, λ_2, λ_3 and λ_4 obtained from this and from the direct measurements with thin plates agree very well, as can be seen in Table A.1.

The absorption coefficient $\alpha_x^{\lambda_4}$ could not be measured directly by the classical method since the absorption constant was too high even for the thin plate of 45 μm thickness. However with the photocurrent method we determined $\alpha_x^{\lambda_4} = 2600 \pm 800 \, \text{cm}^{-1}$ which corresponds well with the Urbach extrapolation (see Fig. A.3) of the directly measured absorption constants, which gave $\alpha_x^{\lambda_4} = 3200 \, \text{cm}^{-1}$.
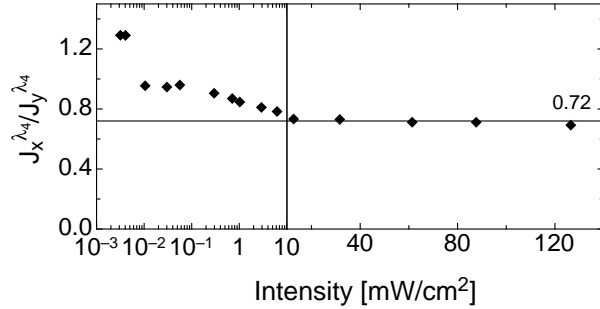
FIGURE A.4: Ratio of the photocurrents $J_x^{\lambda_4}/J_y^{\lambda_4}$ of the x-polarization and the y-polarization as a function of the intensity for $\lambda_4 = 488\,\text{nm}$ and $E = 600\,\text{V/cm}$. For intensities above $10\,\text{W/cm}^2$ a constant ratio $J_x^{\lambda_4}/J_y^{\lambda_4} = 0.72$ is reached.

A.3.2   Determination of the absorption constant in LiTaO$_3$

For the determination of the photocurrent in near-stoichiometric LiTaO$_3$ (SLT) in the interband regime we used UV light, provided by external cavity frequency doubling (WaveTrain, Spectra Physics) of the output of an Ar-ion laser, producing continuous-wave laser radiation at $\lambda = 257\,\text{nm}$. The near stoichiometric crystal with a composition Li/(Li+Ta) = 49.9 % (Curie temperature $T_C = 684\,°\text{C}$), was poled along the z-axis and had the dimensions $1.96 \times 7.94 \times 8.16\,\text{mm}^3$ along the x, y and z axes which where chosen parallel to a, b and c crystal axes respectively. The absorption coefficients at $\lambda = 257\,\text{nm}$ were calculated using the Urbach extrapolation for the stoichiometry of our sample, using the data reported in Ref. 108, which gives $\alpha_z = 270\,\text{cm}^{-1}$ and $\alpha_y = 265\,\text{cm}^{-1}$. This results in a ratio of $\alpha_y/\alpha_z = 0.98$, which agrees well with the value $\alpha_y/\alpha_z = 0.92 \pm 0.10$ that we get from the photocurrent measurements. These results are also expected from direct measurements using a spectrophotometer, which show a similar absorption constant for both polarizations close to the absorption edge.

With a thin plate of magnesium doped near-stoichiometric LiTaO$_3$ (Mg:SLT, $T_C = 694\,°\text{C}$) with dimensions $0.107 \times 9.8 \times 10.0\,\text{mm}^3$ along the x, y and z axes we measured the absorption directly at $\lambda = 257\,\text{nm}$. Both polarizations showed almost the same absorption constants: $\alpha_y = 700 \pm 40\,\text{cm}^{-1}$ and $\alpha_z = 690 \pm 40\,\text{cm}^{-1}$. This confirms the data obtained with the new method, since the ratio of the two polarizations is supposed to be similar for this composition, although the absolute values differ [56, 108].

We previously used another method, the method of the induced absorption change to determine the absorption constant in our SLT crystal at $\lambda = 257\,\text{nm}$ [56]. These results however ($\alpha_z = 450 \pm 70\,\text{cm}^{-1}$ and $\alpha_y = 170 \pm 30\,\text{cm}^{-1}$) do not correspond with the results presented here and determined by the photocurrent method and the results presented in Ref. 108. In BaTiO$_3$, however, the method of induced absorption allowed for an accurate determination of absorption constants up to 1400 cm^{-1} as has been shown in [99]. The failure of the induced absorption method in LiTaO$_3$ samples may suggest that the photo-induced absorption is not, as required, a monotonic function of the light intensity over the

whole intensity range. Our new simple photoconductivity-based method can therefore be used to independently check the results obtained by other more complex techniques.

A.4 Conclusions

We determined the absorption constants beyond the lower edge of the transmission region (absorption constant 10–10^4 cm^{-1}) with a good accuracy. This method does not require the knowledge of any other material constants and it does not require the preparation of thin samples or plates with polished sharp edges.

For $Sn_2P_2S_6$ the absorption constant has been determined from 488–514 nm. The photocurrent measurements have been compared with the data obtained with the direct transmission measurement of the absorption in a very thin plate. These values match quite well and confirm the reliability of the new technique. Also for near-stoichiometric $LiTaO_3$ the obtained data matches the existing values and shows the advantage compared for instance to the indirect method based on the photo-induced absorption.

The technique presented here can be used for determining the absorption constants of any photoconductive crystal, in which interband transitions are induced within a regime where the photoconductivity depends on the square root of the light intensity. Furthermore, provided that all the absorbed light gives rise to photoconduction, the same method can be adapted also to materials where the intensity dependence of the photoconductivity exhibits a regime with a characteristic exponent other than 1/2 or 1 over a sufficiently broad range of light intensities.

Appendix B

Reduction experiments with $Sn_2P_2S_6$

B.1 Introduction

In so called "reduced" crystals, a large fraction of impurities or dopants is in a valence state that is reduced by one unit charge relative to the untreated samples. A lot of knowledge on reduction possibilities was gathered from $BaTiO_3$ for optimizing capacitors build from material [109]. The capacitors degraded after a certain time due to the formation of conductive channels. So the goal of these first studies was to eliminate the reduction process. For photorefractive materials the reduction may be a desired effect, since it often changes the material from p-type to n-type conductivity and increases the effective number of traps in the material [110]. This makes reduction one possibility of increasing the photorefractive response after the growth of a material.

B.2 Samples

Two pure $Sn_2P_2S_6$ samples were used for the experiments. Both were from the same growth and had the same dimensions 4.88 mm $\times$ 3.61 mm $\times$ 1.88 mm along the x, y and z axis. The z surfaces were polished to optical quality and the samples poled according to the standard method for $Sn_2P_2S_6$. After reduction treatment the samples were repoled for measuring the photorefractive properties, since the phase transition temperature of 66 °C was surpassed and multiple domains were created. In the following we refer to the samples as sample 1 and sample 2.

B.3 Experiments

The first attempt was to reduce sample 1 through electro chemical reduction which has been done successfully in $KNbO_3$ crystals [111]. The sample is heated in vacuum or silicon oil to isolate it from the atmospheric gases and an electric field is applied. The physical processes involved in this method are not fully understood, in case of $KNbO_3$
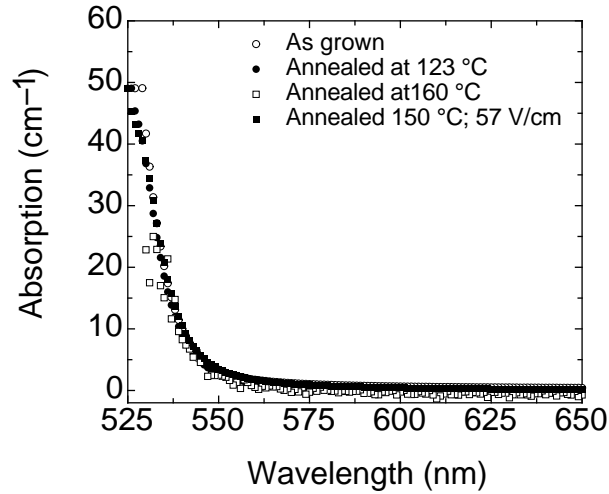
FIGURE B.1: The absorption spectra for x polarized light of sample 1 as grown and after treatment at different temperatures in silicon oil. For the last last treatment at 150°C, an additional electric field was applied in x direction. There is no difference between the as grown crystal and the treated crystal.

one explanation is the removal of O_2 which would leave two electrons in the crystal structure to fill trap levels and thus be available for n-type excitation. In $Sn_2P_2S_6$ the idea was to remove S^{2-} from the crystal structure to create vacancies by heating the sample. Before the treatment the photorefractive properties were determined and the absorption constant measured. The sample was immersed in silicon oil and heated to 120 °C with the heating process taking about one hour. Afterwards the sample was left in this state for about 22 hours and then carefully cooled back down to room temperature. The absorption curves, for the as grown and reduced sample are shown in Fig. B.1. No considerable changes were observed. Also the photorefractive properties did not change. In the next steps first the temperature was increased to 160 °C and then additionally an external field of about 60 V/cm applied along the x axis. The results of the absorption spectrum measurements are shown in Fig. B.1. Still no changes were observable.

The last attempt was to further increase the electric field to 200 V/cm which is about 1/4th of the coercive field of $Sn_2P_2S_6$. After successfully heating the crystal to 150°C during the reduction phase a breakthrough occurred destroying the sample.

The second approach using sample 2 was to encase the crystal in a small tube containing a pure O_2 atmosphere. This should enhance the chances of S^{2-} being removed from the crystal lattice and reduced to S^{4+} in the form of SO_2, leaving free electrons in the crystal structure. We heated this sample with a ramp duration of about three hours up to 150°C, 200°C, 250°C and 280°C, leaving the sample at the respective temperature for about 10 hours and cooling back to room temperature and then measuring the absorption curves. Fig. B.2 shows the absorption curve measurement as grown and after the last treatment at 280 °. No changes were visible compared to the as grown state.
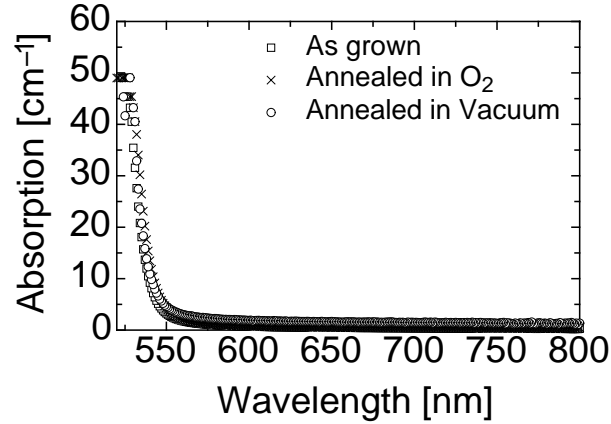
FIGURE B.2: The absorption spectra for x polarized light of sample 2 as grown and after treatment at different temperatures in a oxygen atmosphere and in vacuum. No changes in the absorption behavior were observable.

In Ref. [112] reducing a pure $Sn_2P_2S_6$ crystal at 300°C in vacuum lead to a change in the transmission spectra. Therefore we used a vacuum oven with sample 2 which was taken out of the encasing and heated it for about 10 hours to a temperature of 320°C in vacuum. The absorption spectra after the treatment is shown in Fig. B.2. The resulting absorption spectra once again showed no difference compared to the spectra of the as grown crystal.

B.4   Conclusions and Outlook

None of the reduction techniques applied to the two samples resulted in the change of the absorption or photorefractive properties of the $Sn_2P_2S_6$ crystals. Since reduction of $Sn_2P_2S_6$ crystals has been observed in other cases it can be concluded, that the effect of reducing the sample can differ strongly from different samples which were grown under different conditions. This makes the reproducibly of reduction as a means of increasing the photorefractive properties problematic.

As a future prospect it might be interesting to try and reduce $Sn_2P_2S_6$ crystals from a different growth or try to reduce Te-doped $Sn_2P_2S_6$ samples, since this could lead to a further increase of the photorefractive properties in the very important infrared region.

Appendix C

Bi-doped $Sn_2P_2S_6$

C.1 Introduction

Different approaches were made with $Sn_2P_2S_6$ to increase the photorefractive response of the material. The first was to change the growth parameters, more specifically using SnI_2 instead of SnI_4 as the transport agent and increasing the temperature gradient. This lead to the modified $Sn_2P_2S_6$ crystal of brown color which was referred to as "brown" $Sn_2P_2S_6$. These crystals show an extremely large two-wave mixing gain (as high as 38 cm^{-1} at $\lambda = 633$ nm) which is probably due to an increase of the non-stochiometric defects [26]. A disadvantage is that they have a relatively high absorption constant (5.7 cm^{-1} at $\lambda = 633$ nm) and most importantly the reproducibility is very bad. The next step was to introduce doping elements into the initial growth compound. The most successful one was Te-doping, which increased the coupling constant ($\Gamma = 12$ cm^{-1} at $\lambda = 633$ nm) and also the speed of the grating build-up [30]. Most importantly it increased the photorefractive response in the infrared region and, as is presented in chapter 4, has good photorefractive properties at the telecommunication wavelength 1.55 μm. If the opposite effect is desired and the infrared response of the material should be suppressed while increasing the response at lower wavelength, Sb-doping can be used [30]. Te and Sb were chosen as dopants because they are in the same group as S and P respectively, and can therefore replace these atoms in the crystal lattice. In the same group as P is Bi and was therefore considered as a good candidate for doping $Sn_2P_2S_6$ during the growth process. In the following section the absorption and photorefractive properties of such Bi-doped crystals will be described.

C.2 Samples

The samples used for the characterization were grown from an initial compound of stoichiometric polycrystalline $Sn_2P_2S_6$ samples with different amounts of Bi in the quartz tubes. Three different doping percentages were used 0.01%, 0.1% and 0.5%, which will
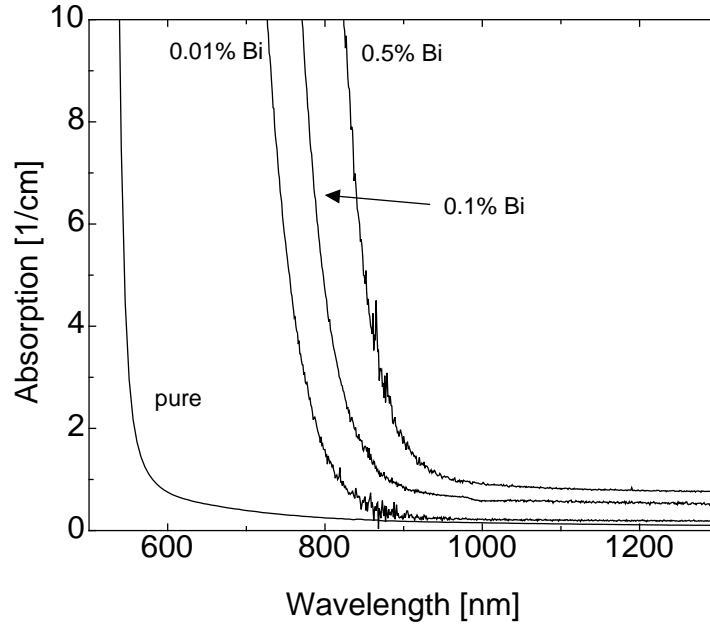
FIGURE C.1: The absorption constant for the three different Bi doped samples and pure $Sn_2P_2S_6$. A slight change of the doping percentage shifts the absorption edge by several tens of nm and allows for a good control of the desired absorption behavior.

from now on be used to describe the different samples. The crystals were cut into z plates for the absorption and photorefractive measurement. The dimensions were 4.5 mm $\times$ 8.6 mm $\times$ 1.5 mm for the 0.01% Bi sample, 4.6 mm $\times$ 6.8 mm $\times$ 0.84 mm for the 0.1% Bi sample and 3.6 mm $\times$ 6.9 mm $\times$ 1.2 mm for the 0.5% Bi sample along the x, y and z axis respectively. The samples were poled in the standard way for $Sn_2P_2S_6$ crystals using a dc field of 1.2 kV/cm in the x direction.

C.3   Results and discussion

The absorption constant was calculated from transmission measurements with a photo-spectrometer and taking into account the Fresnel losses at the surface as well as multiple reflections in the crystal. Fig. C.1 shows the results of the measurement compared to the absorption curve of pure $Sn_2P_2S_6$. The Bi doping shifts the absorption curve towards the infrared region and does not show the "shoulder" in the infrared region which is typical for Te-doped crystals [30]. Thus the absorption remains low in the infrared region in all investigated samples. Interesting is the strong dependence on the exact amount of Bi in the initial compound with higher Bi doping ratios shifting the curve towards longer wavelength. This allows for a good control of the exact location of the lower absorption edge, which could be for example interesting for interband applications tuned to match a certain laser wavelength.

The photorefractive gain constant Γ was determined at several wavelengths for all

three samples. The results of these measurements are shown in Table C.1. Close to the absorption edge the Bi-doping results in a very high gain constant with fast build-up times, making it a good material for near infrared applications. Towards longer wavelength the same behavior as for Sb-doping can be observed and the photorefractive sensitivity drops strongly. Additional information on the grating spacing dependence and thus on the effective number of traps N_{eff} and the effective electro-optic coefficient r_{eff} as well as dielectric properties can be found in Ref. [113]. We modeled the dynamics of the grating build-up with a simple exponential model, whereas in Ref. [113] three different time constants are used. The single exponential approach allows for a better comparability at different wavelengths and doping percentages. In Ref. [113] it is also found, that mainly one of the three time constants contributes to the gain build-up, validating our single exponential approach.

TABLE C.1: Photorefractive two-wave mixing gain and time constants for Bi-doped $Sn_2P_2S_6$ with different doping ratios. The intensity for the build-up times is 1 W/cm^2. The grating spacing was $\Lambda = 1.5$ μm. at $\lambda = 780$ nm the 0.5% Bi-doped sample was too absorbing for measurements.

λ [nm]		0.01% Bi	0.1% Bi	0.5% Bi
780	Γ [cm^{-1}]	23	3.4	-
	α [cm^{-1}]	2.5	7.9	35
	τ [ms]	10	3	-
860	Γ [cm^{-1}]	8	2	15
	α [cm^{-1}]	0.5	1.3	4.3
	τ [ms]	40	12	6
1300	Γ [cm^{-1}]	0.3	0.2	0.5
	α [cm^{-1}]	0.2	0.5	0.8
	τ [ms]	120	70	65

C.4 Conclusions

Bi-doping of $Sn_2P_2S_6$ crystals shifts the absorption edge into the near infrared region and by adjusting the doping percentage the exact location of the absorption edge can be adjusted over several tens of nm. Close to the absorption edge high two-wave mixing gain constants of up to 23 cm^{-1} were demonstrated with build-up times in the order of 10 ms. The deeper infrared response of the material is surpressed. This makes Bi-doped $Sn_2P_2S_6$ a good candidate for applications specifically working at a certain wavelength in the near infrared region.

Conclusions

The interband photorefractive properties of $Sn_2P_2S_6$ have been determined at visible wavelengths and the application of this effect for dynamic light-induced waveguides has been demonstrated. The first step for these experiments was to develop a new method of determining the absorption constant beyond the lower absorption edge of the optical wavelength range (absorption constants of 10–10^4 cm^{-1}) through photocurrent measurements. This method does not require the knowledge of any other material constants and does not require the preparation of thin samples or plates with polished sharp edges. The technique presented here can be used for determining the absorption constants of any photoconductive crystal, in which interband transitions are induced within a regime where the photoconductivity depends on the square root of the light intensity. Furthermore, provided that all the absorbed light gives rise to photoconductivity, the same method can be adapted also to materials where the intensity dependence of the photoconductivity exhibits a regime with a characteristic exponent other than $1/2$ or 1 over a sufficiently broad range of light intensities.

The investigation of the photorefractive effect in $Sn_2P_2S_6$ at $\lambda = 514$ nm resulted in an average refractive index change of $\Delta n = (3 \pm 0.3) \times 10^{-4}$ and a build-up time for the grating in the order of 100 μs at an intensity of 0.6 W/cm^2. This is more than two orders of magnitude faster than the conventional photorefractive effect in the same material. Furthermore, we observed a strong shift of the Bragg angle for the diffraction measurements. This shift is due to the rotation of the indicatrix and by calculating the theoretical shift we could determine the refractive indices in the interband regime. These matched very well with extrapolations from measured data at longer wavelength by using the Sellmeier equation. By using a thin plate of $Sn_2P_2S_6$ (45 μm thick) a very high two-wave mixing gain of $\Gamma = 60 \pm 8$ cm^{-1} could be demonstrated at $\lambda = 514$ nm and the most mobile charge carriers were determined to be holes and therefore $\mu_h > \mu_e$.

Interband holography in $Sn_2P_2S_6$ proves therefore to be an important tool, not only for applications in fast parallel coherent optics, but also as an experimental technique allowing to access and determine material parameters in the high absorption region. As an application we have demonstrated for the first time to our knowledge waveguides and waveguide arrays induced by band-to-band excitation at visible wavelengths. In the electro-optic material $Sn_2P_2S_6$ the fastest build-up of light induced waveguide structures ($\tau = 200$ μs at $I = 0.1$ W/cm^2) reported up to now were measured. This is more than

four orders of magnitude faster than in SBN crystals at the same wavelength. This effect allows to generate different straight and bent dynamic waveguide structures by using external masks or a spatial light modulator. Due to the fast response of $Sn_2P_2S_6$, these structures can be reconfigured in a sub-millisecond time-scale.

In the second part of the thesis the characteristics of Te-doped $Sn_2P_2S_6$ at the important telecommunication wavelength $\lambda = 1.55 \ \mu m$ were investigated. For the first time photorefractive two-beam coupling energy transfer with net gain in a bulk ferroelectric crystal using cw laser light was demonstrated. A gain constant of $2.8 \ cm^{-1}$ was measured without using any enhancement methods such as an external field or stimulating the material at a different wavelength, which are techniques commonly used to perform two-wave mixing in semiconductors at this wavelength. Two different charge carrier contributions were observed, the first having a grating build-up time of about 10 ms and the second in the order of several minutes. This results in a compensation effect on longer timescales, which can be used to further increase the gain by applying the moving grating technique. With this technique a gain constant of $6 \ cm^{-1}$ was demonstrated. An intensity of about $400 \ W/cm^2$ is necessary to achieve this coupling constant at $\lambda = 1.55 \ \mu m$, which is due to the relatively high dark conductivity in $Sn_2P_2S_6$:Te (dark conductivity is the same at all λ).

To decrease the power requirements at telecommunication wavelength, ion-implanted waveguides in $Sn_2P_2S_6$ and $Sn_2P_2S_6$:Te were studied. In the undoped crystal an increase of the effective number of traps N_{eff} was observed, resulting in a higher two-beam coupling gain Γ. At $\lambda = 633 \ nm \ \Gamma$ increased from $3.5 \ cm^{-1}$ to $6.8 \ cm^{-1}$. Neither in the bulk material nor in the waveguide region charge compensation could be observed. In Te-doped $Sn_2P_2S_6$ no increase of N_{eff} could be observed in the waveguiding region compared to the bulk crystal, indicating that the induced trap levels are similar to the ones introduced by Te-doping, since increasing the doping percentage of Te does not affect the photorefractive properties. At $\lambda = 1.55 \ \mu m$ in Te-doped $Sn_2P_2S_6$ a similar photorefractive response in the waveguiding region was observed as in the bulk material. This is especially interesting since as mentioned before at this wavelength a high intensity is needed to reach the saturated two-beam coupling region, making waveguides the ideal choice, even though a slightly higher dark conductivity in the waveguide was measured.

An interesting application for two-beam coupling is beam clean-up of high-power fiber lasers or fiber amplifiers. A seeder-laser is coupled into a specially doped glass fiber, normally erbium or ytterbium is used as a dopant, which is pumped by a high power laser diode. The seeder-laser is amplified in the fiber but has a very bad spatial beam profile at the output of the fiber, since the fiber should be multimode to sustain high laser power. By using a beam-splitter to divert a small (in terms of power) part of the beam, it is possible to clean this weak beam and minimize the powerloss in this process. The energy of the strong beam is then transfered by two-wave mixing to the weak cleaned beam. Since $Sn_2P_2S_6$ is the only ferroelectric material working at $\lambda = 1.55 \ \mu m$ it is a very promising candidate for such an application.

Another prospect is to combine the ion-implantation of $Sn_2P_2S_6$ with the light induced waveguide technique. The ion-implantation would confine the beam depthwise, while the light induced waveguide confines it in the lateral direction, perpendicular to the beam propagation. This would result in a two-dimensional confinement of the beam, which reduces the losses and makes it easier to connect such a switching device to fibers or other integrated optical devices.

Bibliography

[1] A. Ashkin, G. D. Boyd, J. M. Dziedzic, R. G. Smith, A. A. Ballman, J. J. Levinstein, and K. Nassau, "Optically-induced refractive index inhomogeneities in $LiNbO_3$ and $LiTaO_3$," Appl. Phys. Lett. **9**(1), 72–74 (1966).

[2] P. Dittrich, G. Montemezzani, P. Bernasconi, and P. Günter, "Fast, reconfigurable light-induced waveguides," Optics Lett. **24**(21), 1508–1510 (1999).

[3] A. Yariv, "Phase conjugate optics and real-time holography," IEEE Journal of Quantum Electronics **QE-14**(9), 650–660 (1978).

[4] P. Günter, "Holography, coherent light amplification and optical phase conjugation with photorefractive materials," Phys. Reports **93**(4), 199–299 (1982).

[5] A. Marrakchi, J. P. Huignard, and P. Günter, "Diffraction efficiency and energy transfer in two-wave mixing experiments with $Bi_{12}SiO_{20}$ crystals," Appl. Phys. **24**(2), 131–138 (1981).

[6] M. Cronin-Golomb, J. O. White, B. Fischer, and A. Yariv, "Exact solution of a nonlinear model of four-wave mixing and phase conjugation," Optics Letters **7**(7), 313–315 (1982).

[7] N. V. Kukhtarev, V. B. Markov, S. G. Odulov, M. S. Soskin, and V. L. Venetskii, "Holographic storage in electrooptic crystals. II. Beam coupling-light amplification," Ferroelectrics **22**(3-4), 961–964 (1979). UK Journal-Paper English 0015-0193.

[8] N. V. Kukhtarev, V. B. Markov, S. G. Odulov, M. S. Soskin, and V. L. Vinetskii, "Holographic storage in electrooptic crystals. I. Steady state," Ferroelectrics **22**(3-4), 949–960 (1979). UK Journal-Paper English 0015-0193.

[9] V. L. Vinetskii, N. V. Kukhtarev, S. G. Odulov, and M. S. Soskin, "Dynamic self-diffraction of coherent light beams," Soviet Physics Uspekhi **22**(9), 742–56 (1979). USA; Original: USSR Journal-Paper English 0038-5670; Original: 0042-1294.

[10] E. Krätzig and K. Buse, "Two-step processes and IR recording in photorefractive crystals," in *Infrared holography for optical communications. Techniques, materials, and devices.*, pp. 23–39 (Springer-Verlag, Berlin, Germany, 2003).

[11] K. Buse, "Light-induced charge transport processes in photorefractive crystals. I. Models and experimental methods," Applied Physics B **B64**(3), 273–91 (1997).

[12] K. Buse, "Light-induced charge transport processes in photorefractive crystals .2. Materials," Appl. Phys. B **64**, 391–407 (1997).

[13] P. Günter and M. Zgonik, "Clamped-unclamped electro-optic coefficient dilemma in photorefractive phenomena," Opt. Lett. **16**(23), 1826–1828 (1991).

[14] M. Zgonik, P. Bernasconi, M. Duelli, R. Schlesser, P. Günter, M. H. Garrett, D. Rytz, Y. Zhu, and X. Wu, "Dielectric, elastic, piezoelectric, electro-optic, and elasto-optic tensors of $BaTiO_3$ crystals," Phys. Rev. B Condensed Matter **50**(9), 5941–5949 (1994).

[15] P. Günter, "Holography, coherent-light amplification and optical-phase conjugation with photorefrative materials," Physics-Reports Review Section of Physics Letters **93**, 199–299 (1982).

[16] T. K. Gaylord and M. G. Moharam, "Thin and thick gratings: terminology clarification," Appl. Opt. **20**(19), 3271–3273 (1981).

[17] H. Kogelnik, "Coupled wave theory for thick hologram gratings," Bell System Tech. J. **48**(9), 2909–2947 (1969).

[18] G. Montemezzani and M. Zgonik, "Light diffraction at mixed phase and absorption gratings in anisotropic media for arbitrary geometries," Physical Review E Statistical Physics, Plasmas, Fluids, and Related Interdisciplinary Topics **55(1) pt. B**, 1035–1047 (1997).

[19] P. Yeh, "Fundamental limit of the speed of photorefractive effect and is impact on device applications and material research," Appl. Opt. **26**, 602–605 (1987).

[20] G. Montemezzani, P. Rogin, M. Zgonik, and P. Günter, "Interband photorefractive effects: Theory and experiments in $KNbO_3$," Phys. Rev. B Condensed Matter **49**(4), 2484–2502 (1994).

[21] P. A. G. Bernasconi, "Physics and applications of ultraviolet light induced photorefractive gratings," Ph.D. thesis, Swiss Federal Institute of Technology (1988).

[22] A. A. Grabar, M. Jazbinsek, A. N. Shumelyuk, Y. M. Vysochanskii, G. Montemezzani, and P. Günter, "Photorefractive effects in $Sn_2P_2S_6$," in *Photorefractive materials and their applications II*, P. Günter and J. P. Huignard, eds. (Springer-Verlag, Berlin, 2007).

[23] A. A. Grabar, R. I. Muzhikash, A. D. Kostyuk, and Y. M. Vysochanskii, "Investigation of the switching processes in the domain structure of ferroelectric $Sn_2P_2S_6$ by the dynamic holography method," Soviet Physics Solid State **33**(8), 1314–16 Translated from Fizika–Tverdogo–Tela. vol.33, no.8; Aug. 1991; 2335–9 (1991).

[24] S. G. Odoulov, A. N. Shumelyuk, U. Hellwig, R. A. Rupp, A. A. Grabar, and I. M. Stoyka, "Photorefraction in tin hypothiodiphosphate in the near infrared," Journal of the Optical Society of America B (Optical Physics) **13**(10), 2352–2360 (1996).

[25] S. G. Odoulov, A. N. Shumelyuk, U. Hellwig, R. A. Rupp, and A. A. Grabar, "Photorefractive beam coupling in tin hypothiodiphosphate in the near infrared," Optics Letters **21**(10), 752–754 (1996).

[26] A. A. Grabar, I. V. Kedyk, M. I. Gurzan, I. M. Stoika, A. A. Molnar, and Y. M. Vysochanskii, "Enhanced photorefractive properties of modified $Sn_2P_2S_6$," Optics Communications **188**(1-4), 187–194 (2001).

[27] B. Sturman, P. Mathey, H. R. Jauslin, S. G. Odoulov, and A. N. Shumelyuk, "Modeling of the photorefractive nonlinear response in $Sn_2P_2S_6$ crystals," J. Opt. Soc. Am. B **24**, 1303–1309 (2007).

[28] A. N. Shumelyuk, A. Hryhorashchuk, and S. G. Odoulov, "Coherent optical oscillator with periodic zero-π phase modulation," Phys. Rev. A **72**, 023,819 (2005).

[29] A. N. Shumelyuk, K. Shcherbin, S. G. Odoulov, B. Sturman, E. Podivilov, and K. Buse, "Slowing down of light in photorefractive crystals with beam intensity coupling reduced to zero," Phys. Rev. Lett. **93** (2004).

[30] T. Bach, M. Jazbinsek, G. Montemezzani, P. Günter, A. A. Grabar, and Y. M. Vysochanskii, "Tailoring of infrared photorefractive properties of $Sn_2P_2S_6$ crystals by Te and Sb dopint," J. Opt. Soc. Am. B **24**, 1535–1541 (2007).

[31] M. Jazbinsek, D. Haertle, G. Montemezzani, and P. Günter, "Wavelength dependence of visible and near-infrared photorefraction and phase conjugation in $Sn_2P_2S_6$," Opt. Commun. **215**, 333 (2005).

[32] T. Bach, M. Jazbinsek, P. Günter, A. A. Grabar, I. M. Stoika, and Y. M. Vysochanskii, "Self pumped optical phase conjugation at 1.06 μm in Te-doped $Sn_2P_2S_6$," Opt. Express **13**, 9890–9896 (2005).

[33] R. Mosimann, P. Marty, T. Bach, F. Juvalta, M. Jazbinsek, P. Günter, and A. A. Grabar, "High-speed photorefraction at telecommunication wavelength 1.55 μm in $Sn_2P_2S_6$" Opt. Lett. **32**, 3230–3232 (2007).

[34] R. Nitsche and P. Wild, "Crystal growth of metal-phosphorus-sulfur compounds by vapor transport," Materials Research Bulletin **5**(6), 419–423 (1970).

[35] C. D. Carpentier and R. Nitsche, "Vapour growth and crystal data of the thio(seleno)-hypodiphosphates $Sn_2P_2S_6$, $Sn_2P_2Se_6$, $Pb_2P_2S_6$, $Pb_2P_2Se_6$ and their mixed crystals," Materials Research Bulletin **9**(4), 401–410 (1974).

[36] G. Dittmar and H. Schäfer, "Die Struktur des Di-Zinn-Hexathiohypo-diphosphats $Sn_2P_2S_6$," Zeitschrift fuer Naturforschung **29B**(5-6), 312–327 (1974).

[37] B. Scott, M. Pressprich, R. D. Willet, and D. A. Cleary, "High temperature crystal structure and DSC of $Sn_2P_2S_6$," Journal of Solid State Chemistry **96**(2), 294–300 (1992).

[38] A. P. Buturlakin, M. I. Gurzan, and V. Y. Slivka, "Ferroelectric properties of $Sn_2P_2S_6$ crystals," Soviet Physics Solid State **19**(7), 1165–7 Translated from Fizika–Tverdogo–Tela. vol.19, no.7; July 1977; 1990–3 (1977).

[39] Y. M. Vysochanskii, V. Y. Slivka, V. Voroshilov Yu, M. I. Gurzan, and D. V. Chepur, "Model of the phase transition in the ferroelectric semiconductor $Sn_2P_2S_6$, and its lattice dynamics," Soviet Physics Solid State **21**(8), 1382–5 Translated from Fizika–Tverdogo–Tela. vol.21, no.8; Aug. 1979; 2402–8 (1979).

[40] "ANSI/IEEE Std 176 - IEEE Standard on Piezoelectricity," in *ANSI/IEEE Std 176-1987*, p. 242 (IEEE, Inc; 345 East 47th Street, New York, NY 10017, USA, 1987). FE 0.42 in our old articles in HPF E18.

[41] C. D. Carpentier and R. Nitsche, "Ferroelectricity in $Sn_2P_2S_6$," Materials Research Bulletin **9**(8), 1097–1100 (1974).

[42] D. Haertle, A. Guarino, J. Hajfler, G. Montemezzani, and P. Günter, "Refractive indices of $Sn_2P_2S_6$ at visible and infrared wavelengths," Optics Express **13**(6), 2047–2057 (2005).

[43] M. M. Maior, Y. M. Vysochanskii, I. P. Prits, B. Molnar Sh, L. A. Seikovskaya, and V. Y. Slivka, "Pyroelectric properties of oblique cuts of an $Sn_2P_2S_6$ crystal," Soviet Physics Crystallography **35**(5), 767–9 Translated from Kristallografiya. vol.35, no.5; Sept.–Oct. 1990; 1300–2 (1990).

[44] M. M. Maior, V. P. Bovtun, M. Poplavko Yu, B. M. Koperles, and M. I. Gurzan, "Dielectric properties of $Sn_2P_2S_6$ crystals," Soviet Physics Solid State **26**(3), 397–400 Translated from Fizika–Tverdogo–Tela. vol.26, no.3; March 1984; 659–64 (1984).

[45] V. N. Zhikharev, V. Popik Yu, and I. D. Seikovskii, "Specific features of ferroelectric switching in $Sn_2P_2S_6$ single crystals," Crystallography Reports **41**(5), 855–858 Translated from Kristallografiya. vol.41, no.5; Sept.–Oct. 1996; 898–901 (1996).

[46] M. I. Gurzan, A. P. Buturlakin, V. S. Gerasimenko, N. F. Korde, and V. Y. Slivka, "Optical properties of $Sn_2P_2S_6$ crystals," Soviet Physics Solid State **19**(10), 1794–1795 (1977).

[47] D. Haertle, M. Jazbinsek, G. Montemezzani, and P. Günter, "Nonlinear optical coefficients and phase-matching conditions in $Sn_2P_2S_6$," Optics Express **13**(10), 3765–3776 (2005).

[48] A. A. Grabar, I. V. Kedyk, I. M. Stoika, Y. M. Vysochanskii, M. Jazbinsek, G. Montemezzani, and P. Gunter, "Enhanced photorefractive properties of Te-doped $Sn_2P_2S_6$," in *Ninth International Conference on Photorefractive Effects, Materials and Devices. 17 21 June 2003 La Colle sur Loup, France*, P. Delaye, C. Denz, L. Mager, and G. Montemezzani, eds., pp. xv+740 (Opt. Soc. Am., Washington, DC, USA, 2003).

[49] D. Haertle, G. Caimi, A. Haldi, G. Montemezzani, P. Günter, A. A. Grabar, I. M. Stoika, and Y. M. Vysochanskii, "Electro-optical properties of $Sn_2P_2S_6$," Opt. Comm. **215**(4-6), 333–343 (2003).

[50] Y. M. Vysochanskii, M. I. Gurzan, M. M. Maior, E. D. Rogach, F. I. Savenko, and V. Y. Slivka, "Piezoelectric properties of single crystals of $Sn_2P_2S_6$," Soviet Physics Crystallography **35**(3), 459–61 Translated from Kristallografiya. vol.35, no.3; May–June 1990; 784–6 (1990).

[51] R. M. Yevych, S. I. Perechinskii, A. A. Grabar, Y. M. Vysochanskii, and V. Y. Slivka, "Temperature dependence of the brillouin spectra in $Sn_2P_2S(Se)_6$ ferroelectric crystals," Condensed Mat. Phys. **6**(2), 315–323 (2003).

[52] Y. M. Vysochanskii, M. M. Maior, V. A. Medvedev, V. M. Rizak, V. Y. Slivka, and E. A. Sorkin, "Low-temperature specific heat and pyroactivity of ferroelectric crystals of the system Sn(Pb)/sub 2/P/sub 2/S(Se)/sub 6," Soviet Physics Crystallography **35**(4), 541–4 Translated from Kristallografiya. vol.35, no.4; July–Aug. 1990; 918–22 (1990).

[53] A. A. Vasilkevich, Y. M. Vysochanskii, P. G. Ivanitskii, V. M. Rizak, I. M. Rizak, V. Y. Slivka, and V. I. Slisenko, "Density of states and thermodynamic properties of the ferroelectrics $Sn_2P_2S_6$ and Sn/sub 2/P/sub 2/Se/sub 6," Physics of the Solid State **36**(5), 660–3 Translated from Fizika–Tverdogo–Tela. vol.36, no.5; May 1994; 1205–12 (1994).

[54] K. Al' Shufi, V. M. Rizak, I. M. Rizak, I. P. Prits, Y. M. Vysochanskii, and V. Y. Slivka, "Thermal conductivity of ferroelectric $Sn_2P_2S_6$ in the temperature range 4.2-370 K," Physics of the Solid State **35**(8), 1055–1057 Translated from Fizika–Tverdogo–Tela. vol.35, no.8; Aug. 1993; 2122–7 (1993).

[55] R. Mosimann, D. Haertle, M. Jazbinsek, G. Montemezzani, and P. Günter, "Interband photorefraction in $Sn_2P_2S_6$ at visible wavelengths," J. Opt. Soc. Am. B **23**, 1620–1625 (2006).

[56] P. Dittrich, B. Koziarska-Glinka, G. Montemezzani, P. Günter, S. Takekawa, K. Kitamura, and Y. Furukawa, "Deep-ultraviolet interband photorefraction in lithium tantalate," Journal of the Optical Society of America B Optical Physics **21**(3), 632–9 (2004).

[57] P. Bernasconi, G. Montemezzani, M. Wintermantel, L. Biaggio, and P. Günter, "High-resolution, high-speed photorefractive incoherent-to-coherent optical converter," Optics Letters **24**(4), 199–201 (1999).

[58] R. Ryf, G. Montemezzani, P. Günter, A. A. Grabar, I. M. Stoika, and Y. M. Vysochanskii, "High-frame-rate joint Fourier-transform correlator based on $Sn_2P_2S_6$ crystal," Optics Letters **26**(21), 1666–8 (2001).

[59] P. Dittrich, G. Montemezzani, and P. Günter, "Tunable optical filter for wavelength division multiplexing using dynamic interband photorefractive gratings," Optics Communications **214**(1-6), 363–70 (2002).

[60] A. Shumelyuk, S. Odoulov, D. Kip, and E. Kratizig, "Electric-field enhancement of beam coupling in $Sn_2P_2S_6$," Appl. Phys. B **72**(6), 707–10 (2001).

[61] M. Jazbinsek, G. Montemezzani, P. Günter, A. A. Grabar, I. M. Stoika, and Y. M. Vysochanskii, "Fast near-infrared self-pumped phase conjugation with photorefractive $Sn_2P_2S_6$," Journal of the Optical Society of America B Optical Physics. June **20**(6), 1241–6 (2003).

[62] G. Montemezzani, R. Ryf, D. Haertle, P. Günter, A. A. Grabar, I. M. Stoika, and Y. M. Vysochanskii, "Continuous-wave interband photorefraction in $Sn_2P_2S_6$," Ukrainian Journal of Physics **49**(4), 333–8 (2004).

[63] R. Mosimann, D. Haertle, M. Jazbinsek, G. Montemezzani, and P. Günter, "Determination of the absorption through photocurrent measurement in the interband regime," Appl. Phys. B **83**, 115–119 (2005).

[64] A. A. Grabar, "Directional light scattering by domain walls in $Sn_2P_2S_6$ uniaxial ferroelectrics," Journal of Physics: Condensed Matter **10**(10), 2339–46 (1998).

[65] G. Montemezzani, P. Rogin, M. Zgonik, and P. Günter, "Interband photorefractive effects in KNbO$_3$ induced by ultraviolet illumination," Optics Letters **18**(14), 1144–6 (1993). USA Journal-Paper English 0146-9592.

[66] M. Carrascosa, F. Agullo-Lopez, G. Montemezzani, and P. Günter, "Photorefractive gratings generated by band-gap excitation: application to KNbO$_3$," Applied Physics B Lasers and Optics **B72**(6), 697–700 (2001).

[67] P. Günter, *Nonlinear optical effects and materials*, vol. 72 of *Springer Series in Optical Science* (Springer, Berlin, Heidelberg, New York, 2000).

[68] O. Matoba, T. Inujima, T. Shimura, and K. Kuroda, "Segmented photorefractive waveguides in LiNbO$_3$:Fe," J. Opt. Soc. Am. B **15**(7), 2006–2012 (1998).

[69] F. Juvalta, P. Dittrich, G. Montemezzani, M. Jazbinšek, P. Gunter, S. Takekawa, and K. Kitamura, "Holographic gratings in pure and Mg-doped near-stoichiometric LiTaO$_3$ induced by deep-ultraviolet light," Holography 2005: International Conference on Holography, Optical Recording, and Processing of Information **6252**, A2520–A2520 (2006).

[70] D. N. Christodoulides, F. Lederer, and Y. Silberberg, "Discretizing light behaviour in linear and nonlinear waveguide lattices," Nature **424**(6950), 817–823 (2003).

[71] J. W. Fleischer, M. Segev, N. K. Efremidis, and D. N. Christodoulides, "Observation of two-dimensional discrete solitons in optically induced nonlinear photonic lattices," Nature **422**(6928), 147–150 (2003).

[72] H. S. Eisenberg, Y. Silberberg, R. Morandotti, and J. S. Aitchison, "Diffraction management," Phys. Rev. Lett. **85**(9), 1863–1866 (2000).

[73] J. W. Fleischer, G. Bartal, O. Cohen, T. Schwartz, O. Manela, B. Freedman, M. Segev, H. Buljan, and N. K. Efremidis, "Spatial photonics in nonlinear waveguide arrays," Opt. Express **13**(6), 1780–1796 (2005).

[74] A. Shumelyuk, S. Odoulov, O. Oleynik, G. Brost, and A. A. Grabar, "Spectral sensitivity of nominally undoped photorefractive Sn$_2$P$_2$S$_6$" Appl. Phys. B **88**(1), 79–82 (2007).

[75] P. Günter and J. P. Huignard, *Photorefractive Materials and Applications II* (Springer-Verlag, Berlin, 2005).

[76] C. Dan, D. Wolfersberger, N. Fressengeas, G. Montemezzani, and A. A. Grabar, "Near infrared photorefrative self focusing in Sn$_2$P$_2$S$_6$ Te crystals," Opt. Express **16**, 12,777 (2007).

[77] P. Günter and J. P. Huignard, *Photorefractive Materials and Their Applications 3* (Springer-Verlag, Berlin, 2007).

[78] A. Partovi, J. Millert, E. M. Garmire, M. Ziari, W. Steier, S. B. Trivedi, and M. B. Klein, "Photorefractivity at 1.5 μm in CdTe-V," Appl. Phys. Lett. **57**, 846 (1990).

[79] K. Shcherbin, "Recent Progress in Semiconductor Photorefractive Crystals," in *Photorefractive Materials and Their Applications 2*, P. Günter and J. P. Huignard, eds., pp. 391–418 (Springer-Verlag, Berlin, 2007).

[80] P. Acebal, S. Blaya, and L. Carretero, "Bidimensional chromophores for photorefractive polymers with working wavelengths in the near IR," Opt. Express **13**, 8296 (2005).

[81] M. Wesner, C. Herden, E. Krätzig, D. Kip, and P. Moretti, "Photorefractive steady state solitons up to telecommunication wavelengths in planar SBN waveguides," Opt. Commun. **188**, 69 (2001).

[82] S. Brülisauer, D. Fluck, P. Günter, L. Beckers, and C. Buchal, "Photorefractive effect in proton-implanted Fe-doped $KNbO_3$ waveguides at telecommunication wavelengths," J. Opt. Soc. Am. B **13**, 2544 (1996).

[83] M. Horowitz, B. Fischer, Y. Barad, and Y. Silberberg, "Photorefractive effect in a $BaTiO_3$ crystal at the 1.5 μm wavelength regime by two-photon absorption," Opt. Lett. **21**, 1120 (1996).

[84] O. Beyer, I. Breunig, F. Kalkum, and K. Buse, "Photorefractive effect in iron-doped lithium niobate crystals induced by femtosecond pulses of 1.5 μm wavelength," Appl. Phys. Lett. **88**, 051,120 (2006).

[85] A. N. Shumelyuk, A. Hryhorashchuk, S. G. Odoulov, and D. R. Evans, "Transient gain enhancement in photorefractive crystals with two types of movable charge carrier," Opt. Lett. **32**, 1959 (2007).

[86] J.-Y. Moisan, N. Wolffer, O. Moine, P. Gravey, G. Martel, A. Aoudia, E. Repka, Y. Marfaing, and R. Triboulet, "Characterization of photorefractive CdTe-V - High 2-wave mixing gain with an optimum low-frequency periodic external electric-field," J. Opt. Soc. Am. B **11**, 1655 (1994).

[87] P. Pogany, H. J. Eichler, and M. H. Ali, "Two-wave mixing gain enhancement in photorefractive CdZnTe: V by optically stimulted electron-hole resonance," J. Opt. Soc. Am. B **15**, 2716 (1998).

[88] A. Guarino, M. Jazbinsek, C. Herzog, R. Degl'Innocenti, G. Poberaj, and P. Günter, "Optical waveguides in $Sn_2P_2S_6$ by low fluence MeV He^+-ion implantation," Opt. Express **14**, 2344 (2006).

[89] L. A. Montmorillon, P. Delaye, J. C. Launey, and G. Roosen, "Comparative study of CdTe and GaAs photorefractive performances from 1 μm to 1.55 μm," Opt. Mater. **4**, 233 (1995).

[90] G. W. Ross, P. Hribek, R. W. Eason, M. H. Garrett, and D. Rytz, "Impurity enhanced self-pumped phase conjugation in the near infrared in 'blue' BaTiO$_3$," Optics Communications **101**(1-2), 60–4 (1993). Netherlands Journal-Paper English 0030-4018.

[91] C. Medrano, M. Zgonik, N. Sonderer, C. Beyeler, S. Krucker, J. Seglins, H. Wüest, and P. Günter, "Photorefractive effect in Cu- and Ni-doped KNbO$_3$ in the visible and near infrared," J. Appl. Phys. B **76**, 5640–5645 (1994).

[92] M. Kaczmarek, R. W. Eason, and I. Mnushkina, "The effect of doping and processing conditions on the optical performance of Rh:BaTiO$_3$," Applied Physics B Lasers and Optics **B68**(5), 813–17 (1999). Springer-Verlag Germany Journal-Paper English 0946-2171.

[93] D. Kip, "Photorefractive waveguides in oxide crystals: fabrication, properties, and applications," J. Appl. Phys. B **67**, 191–150 (1998).

[94] A. Guarino and P. Günter, "Nondestructive method for the determination of planar waveguide profiles by means of a non-stationary mode index calculation," Opt. Lett. **30**, 2412–2414 (2005).

[95] D. Fluck, J. A. Weiss, S. Brülisauer, and P. Günter, "Two-wave mixing of focused Gaussian beams in photorefractive waveguides," Optics Lett. **19**, 2080–2082 (1994).

[96] N. M. Jokerst and E. Garmire, "Nonlinear optical absorption in semiconductor epitaxial depletion regions," Applied Physics Letters **53**(10), 897–9 (1988).

[97] D. D. Nolte, Q. Wang, and M. R. Melloch, "Robust infrared gratings in photorefractive quantum wells generated by an above-band-gap laser," Applied Physics Letters **58**(19), 2067–9 (1991). USA Journal-Paper English 0003-6951.

[98] A. Partovi, A. M. Glass, D. H. Olson, G. J. Zydzik, and K. T. Short, "High-speed photodiffractive effect in semi-insulating CdZnTe/ZnTe multiple quantum wells," Optics Letters **17**(9), 655–7 (1992).

[99] G. Ross, G. Montemezzani, P. Bernasconi, M. Zgonik, and P. Günter, "Strong ultraviolet induced absorption and absorption gratings in BaTiO$_3$," Journal of Applied Physics **79**(7), 3665–8 (1996).

[100] M. Jazbinˇsek, M. Zgonik, S. Takekawa, M. Nakamura, K. Kitamura, and H. Hatano, "Reduced space-charge fields in near-stoichiometric LiTaO$_3$ for

blue, violet, and near-ultraviolet light beams," Applied Physics B Lasers and Optics **B75**(8), 891–4 (2002). Springer-Verlag Germany Journal-Paper doi:10.1007/s00340-002-1069-3 English 0946-2171.

[101] J. A. Bardwell and M. J. Dignam, "Extensions of the Kramers-Kronig transformation that cover a wide range of practical spectroscopic applications," Journal of Chemical Physics **83**(11), 5468–78 (1985).

[102] L. Mutter, M. Jazbinˇsek, M. Zgonik, U. Meier, C. Bosshard, and P. Günter, "Photobleaching and optical properties of organic crystal 4-N, N-dimethylamino-4'-N'-methyl stilbazolium tosylate," Journal of Applied Physics **94**(3), 1356–61 (2003). AIP USA Journal-Paper doi:10.1063/1.1588359 English 0021-8979.

[103] T. S. Moss, "Photoconductivity," Reports on Progress in Physics **28** (1965).

[104] R. Ryf, G. Montemezzani, P. Günter, A. A. Graber, and I. M. Stoyka, "Interband photorefraction at visible wavelength in $Sn_2P_2S_6$ crystals," Advances in Photorefractive Materials **27**, 80–85 (1999).

[105] I. P. Studenyak, V. V. Mitrovcij, G. Kovacs, O. A. Mykajlo, M. I. Gurzan, and Y. M. Vysochanskii, "Temperature variation of optical absorption edge in $Sn_2P_2S_6$ and SnP_2S_6 crystals," Ferroelectrics **254**(1-4), 295–310 (2001).

[106] Y. W. Liu, K. Kitamura, S. Takekawa, M. Nakamura, Y. Furukawa, and H. Hatano, "Two-color photorefractive properties in near-stoichiometric lithium tantalate crystals," Journal of Applied Physics **95**(12), 7637–44 (2004).

[107] J. P. Meyn and M. M. Fejer, "Tunable ultraviolet radiation by second-harmonic generation in periodically poled lithium tantalate," Optics Letters **22**(16), 1214–16 (1997).

[108] C. Baumer, C. David, A. Tunyagi, K. Betzler, H. Hesse, E. Kratzig, and M. Wohlecke, "Composition dependence of the ultraviolet absorption edge in lithium tantalate," Journal of Applied Physics **93**(5), 3102–4 (2003).

[109] N. H. Chan, R. K. Sharma, and D. M. Smyth, "Non-stoichiometry in undoped $BaTiO_3$," J. Am. Cer. Soc. **64**, 556–562 (1981).

[110] A. Krumins and P. Günter, "Diffraction efficiency and energy-transfer during hologram formation if reduced $KNbO_3$," Appl. Phys. **19**, 153–163 (1979).

[111] C. Medrano, C. Voit, P. Amrhein, and P. Günter, "Optimization of the photorefractive properties of $KNbO_3$ crystals," J. Appl. Phys. **64**, 4668–4673 (1988).

[112] Z. Potucek and Z. Bryknar, "Photoluminescence of defects in $Sn_2P_2S_6$ crystals," Ferroelectrics **334**, 447–455 (2006).

[113] I. V. Kedyk, P. Mathey, G. Gadret, O. Bidault, A. A. Grabar, I. M. Stoika, and Y. M. Vysochanskii, "Enhanced photorefractive properties of Bi-doped $Sn_2P_2S_6$," J. Opt. Soc. Am. B **25**, 180–186 (2008).

List of publications

Articles

- R. Mosimann, D. Haertle, M. Jazbinsek, G. Montemezzani, P. Günter,"Determination of the absorption constant in the interband region by photocurrent measurements", Applied Physics B **83**, 115-119 (2006)

- R. Mosimann, D. Haertle, M. Jazbinsek, G. Montemezzani, P. Günter, "Interband photorefraction in $Sn_2P_2S_6$ at visible wavelengths", Journal of the Optical Society of America B **23**, 1620-1625, (2006)

- R. Mosimann, P. Marty, T. Bach, F. Juvalta, M. Jazbinsek, P. Günter, A. A. Grabar, "High-speed photorefraction at telecommunication wavelength 1.55 μm in $Sn_2P_2S_6$:Te", Optics Letters **32**, 3230-3232 (2007)

- F. Juvalta, R. Mosimann, M. Jazbinsek, P. Günter, "Fast dynamic waveguides and waveguide arrays in photorefractive $Sn_2P_2S_6$ induced by visible light', Accepted in Optics Express **13**, 3765–76 (2008)

- R. Mosimann, F. Juvalta, M. Jazbinsek, P. Günter, A. A. Grabar, "Photorefractive waveguides in He^+-ion implanted pure and Te-doped $Sn_2P_2S_6$", Submitted to Journal of the Optical Society of America B (2008)

Conference proceedings

- R. Mosimann, M. Jazbinsek, P. Günter, G. Montemezzani, "Interband dynamic holography at visible wavelengths in $Sn_2P_2S_6$", 2007 Conference on Lasers and Electro Optics Europe CLEO/Europe (2007)

- R. Mosimann, P. Marty, M. Jazbinsek, P. Günter, A. A. Grabar, "Photorefractive two-wave mixing in $Sn_2P_2S_6$:Te at 1.55 μm", Conference on Lasers and Electro-Optics (CLEO 2008), San Jose, Ca, USA (2008).

- G. Montemezzani, C. Dan, M. Gorram, N. Fressengeas, D. Wolfersberger, **F. Juvalta**, R. Mosimann, M. Jazbinsek, P. Günter, and A. A. Grabar, "Real-time

Photoinduced Waveguides in $Sn_2P_2S_6$ Bulk Crystals with Visible or Near Infrared Light," in *Controlling Light with Light: Photorefractive Effects, Photosensitivity, Fiber Gratings, Photonic Materials and More*, OSA Technical Digest (CD), paper TuB3 (2007).

Acknowledgments

I would like to thank everyone who contributed to this thesis and supported me during the last four years. May this have been through their great scientific knowledge, help in the laboratory, fruitful discussions or by cheerful laughter. In particular I would like to thank the following people:

Prof. Dr. P. Günter, for the opportunity to do a PhD at the Nonlinear Optics Laboratory and the knowledge he shared with me,

Prof. Dr. G. Montemezzani for being the co-examiner of this thesis and the support given at the beginning of my thesis,

Dr. M. Jazbinsek for directing me through my thesis and helping to overcome any obstacles presenting themselves,

my roommate *F. Juvalta* for the fruitful discussions on a variety of topics and introducing me to floorball,

J. Hajfler for his expert crystal preparation,

T. Bach for his help on many topics and introducing me to the world of real estate,

the remaining members of the photorefractive team namely *Dr. D. Haertle* and *Dr. Ph. Dittrich* for sharing their knowledge

all the other member of the Günter group for creating the nice working atmosphere and the good time we spent together.

And finally my parents *Monika* and *Peter* for without them I would not be were I am now.

Curriculum vitae

Roger Mosimann, born on September 24, 1979 in Rheinfelden (Switzerland)

2008	Ph. D. thesis on "*Photorefractive effects in $Sn_2P_2S_6$ at near bandgap and telecommunication wavelengths* ", in the Nonlinear Optics Laboratory of Prof. Dr. P. Günter at the Institute of Quantum Electronics of ETH Zürich
2004–2008	Research and teaching assistant in the group of Prof. Dr. P. Günter, ETH Zürich
2004	Graduation with a diploma in experimental physics on "*Interband photorefractive effects in $Sn_2P_2S_6$*"
1999–2004	Study of Physics at the Swiss Federal Institute of Technology Zürich (ETH Zürich)
1995–1999	Matura am Gymnasium Muttenz (BL)
1995–1986	Primary and secondary school, Canton Aargau
1984–1985	First grade in Summit, New Jersey, USA